Molecular Dynamics of Crystal Growth and Transport in Zeolites

Harald Tepper

2001

Ph.D. thesis
University of Twente

Twente University **Press**

Also available in print:
http://www.tup.utwente.nl/uk/catalogue/technical/mdzeolites/

Molecular Dynamics of Crystal Growth and Transport in Zeolites

Promotion committee:

Prof.dr. P.J. Gellings	*University of Twente (chairman)*
Prof.dr. W.J. Briels	*University of Twente (thesis supervisor)*
Prof.dr.ir. A.B. de Haan	*University of Twente*
Prof.dr.ir. B. Poelsema	*University of Twente*
Prof.dr. D.N. Theodorou	*University of Patras, Greece*
Prof.dr. J.P.J.M. van der Eerden	*Utrecht University*
Prof.dr.ir. B. Smit	*University of Amsterdam*

Twente University **Press**

Twente University Press,
P.O. Box 217, 7500 AE Enschede, The Netherlands, www.tup.utwente.nl

Cover design Jo Molenaar [deel 4] ontwerpers
Print Grafisch Centrum Twente

Motto (page V) taken from the title of a collection of poems by Rutger Kopland.

Typeset in LaTeX, by the author

ISBN 9036516528

MOLECULAR DYNAMICS OF CRYSTAL GROWTH AND TRANSPORT IN ZEOLITES

IN SEARCH OF THE MACROSCOPIC LIMIT

PROEFSCHRIFT

ter verkrijging van
de graad van doctor aan de Universiteit Twente,
op gezag van de rector magnificus,
prof.dr. F.A. van Vught,
volgens besluit van het College voor Promoties
in het openbaar te verdedigen
op vrijdag 26 oktober te 16.45 uur

door

Harke Lucas Tepper
geboren op 28 oktober 1972
te Hattem

Dit proefschrift is goedgekeurd door de promotor

prof.dr. W.J. Briels

Wie wat vindt heeft slecht gezocht

Rutger Kopland

Contents

Part I

Preludium

About the author

On October 28, 1972, Harald Tepper was born in Hattem (the Netherlands) where he spent the first 20 days of his life. Thereafter he moved to Vaassen, where he grew up and attended primary school. In september 1984, he entered the Gymnasium in Apeldoorn, from which he graduated in 1990.

In that same year, the author started his studies in Chemical Technology at the University of Twente. As part of his practical training, he spent four months in the group of Dr. K. Hermansson at the University of Uppsala (Sweden), for which he was awarded a scholarship from 'Svenska Institutet' in Stockholm. He carried out ab initio calculations on diatomic molecules in electrical fields and molecular dynamics simulations on water exchange around solvated lithium ions. The work resulted in a publication in 'Molecular Physics'.

The graduation project was performed in the Chemical Physics group of (then) Prof. D. Feil under the supervision of Dr. W.J. Briels. It was entitled 'Towards a crystal growth morphology of the Lennard-Jones system' and formed the start of the work that was later to appear in 'Physical Review Letters' (see also *Chapter 2* of this thesis). In September 1996 he graduated (cum laude) as chemical engineer.

In September 1991, Harald also started studying clarinet with P.M. Dijcks at the Conservatory in Enschede. He graduated as 'teaching musician' in January 1997. As an extended (one-year) practical training period, he was involved in the project 'Music and school' in Hengelo, providing weekly musical teaching to children in an underprivileged neighbourhood.

The author was employed as a Ph.D. student (AIO) at the University of Twente from February 1997 till August 2001. Under the supervision of Prof. W.J. Briels in the (then) Computational Chemistry group, he carried out molecular dynamics simulations on crystal growth and diffusion in zeolites, the results of which have been laid down in this thesis. Parts of the work have been presented at conferences in Lunteren (the Netherlands), Uppsala (Sweden), Lyon (France), Hillerød (Denmark), Baltimore (USA), and Granada (Spain). A full list of publications in refereed journals is given on the next page. Apart from being engaged in research, Harald was involved as a teacher in courses on classical mechanics, quantum theory, and statistical thermodynamics.

From September 1996 till July 2001, he was also employed as a musical teacher with the wind orchestra 'Excelsior' in Eibergen, where he provided weekly clarinet lessons for adults.

The author will continue his scientific studies in the group of Prof. G.A. Voth at the University of Utah in Salt Lake City (USA), starting February 2002.

List of publications

- H.L. Tepper and W.J. Briels,
  Comments on the use of the Einstein equation for transport diffusion. Application to argon in $AlPO_4$-5,
  Submitted to J. Chem. Phys.

- H.L. Tepper and W.J. Briels,
  Crystal growth and interface relaxation rates from fluctuations in an equilibrium simulations of the Lennard-Jones (100) crystal-melt system,
  Submitted to J. Chem. Phys.

- H.L. Tepper and W.J. Briels,
  Crystallization and melting in the Lennard-Jones system. Equilibration, relaxation and long-time dynamics of the moving interface,
  Accepted for publication in J. Chem. Phys. (scheduled issue: November 22, 2001).

- H.L. Tepper and W.J. Briels,
  Simulations of crystallization and melting of the FCC (100) interface: The crucial role of lattice imperfections,
  J. Cryst. Growth **230**(1-2), 270 (August 2001).

- J.P. Hoogenboom, H.L. Tepper, N.F.A. van der Vegt and W.J. Briels,
  Transport diffusion of argon in $AlPO_4$-5 from equilibrium molecular dynamics simulations,
  J. Chem. Phys. **113**(16), 6875 (October 22, 2000).

- H.L. Tepper, J.P. Hoogenboom, N.F.A. van der Vegt and W.J. Briels,
  Unidirectional diffusion of methane in $AlPO_4$-5,
  J. Chem. Phys. **110**(23), 11511 (June 15, 1999).

- W.J. Briels and H.L. Tepper,
  Crystal growth of the Lennard-Jones (100) surface by means of equilibrium and nonequilibrium molecular dynamics,
  Phys. Rev. Lett. **79**(25), 5074 (December 22, 1997).

- Kersti Hermansson and Harald Tepper,
  Electric-field effects on vibrating polar molecules: from weak to strong fields,
  Mol. Phys. **89**(5), 1291 (December 10, 1996).

Introduction

Walking around in nature, looking at the sea, feeling the wind, or climbing on solid rocks, there is hardly any reason to believe that all matter is constituted of small atoms, moving around in an everlasting motion. In fact, despite the early speculation by the ancient Greek Demokritos, it was not before the beginning of the 20th century that the atomic nature of matter was accepted beyond reasonable doubt. Our direct knowledge of the behaviour of matter is almost exclusively derived from the observation of samples that are very large compared to atomic dimensions. Most scientific experiments therefore relate to the average properties of an immense number of atoms or molecules. To give an example, 18 grams of water contain one mole of molecules ($\approx 6 \times 10^{23}$ molecules). Suppose one would want to count such a number of particles. If one were be able to do so at a rate of 100 per minute then, even with the help of the entire wold's population, it would still last 2000 millennia (!) until all the molecules in those 18 grams would have been counted.

Fortunately, one does not need to consider all individual molecules in order to describe the nature of matter. Although the individual trajectories of the molecules in, say, two separate glasses of water do not resemble each other at all, the macroscopic behaviour of the two samples will be the same. It is a well-established fact in *thermodynamics* that only three variables, such as for instance pressure, temperature, and number of particles, have to be specified to unambiguously define the state of a system (or, to be precise, a one-component system in equilibrium). If the corresponding thermodynamic potential (in this case the Gibbs free energy) is known as a function of those variables, all other properties, such as the heat capacity, compressibility, etc., can be derived from it. The power and internal consistency of the theory of thermodynamics once led Albert Einstein to remark [52]:

> A theory is the more impressive the greater the simplicity of its premises, the more different kinds of things it relates, and the more extended its area of applicability. Therefore the deep impression that classical thermodynamics made upon me. It is the only physical theory of universal content which I am convinced will never be overthrown, within the framework of applicability of its basic concepts.

Despite the immense power in describing the relations between thermodynamic properties, thermodynamics does not provide the means to predict absolute quantities. They need to be supplied by an external source, such as experimental measurements. One could, for instance, measure the temperature with a thermometer, or the pressure with a manometer. Another approach would be to try and predict the macroscopic properties from microscopic principles. This is the realm of *statistical thermodynamics*; starting from a model of the microscopic constitution of a material (and the interactions between its microscopic constituents), theories are developed that predict thermodynamic properties from the average statistical behaviour of a vast number of constituents. At this point the question could be

raised 'how vast is vast?' or in other words 'what should be the size of the model system under consideration?' The size of the system at which it starts to display macroscopic behaviour is generally referred to as the *macroscopic limit*. In most analytical theories, extrapolation to the macroscopic limit is not a problem. Usually equations are derived for a fixed number of particles N and the result is subsequently taken to the limit $N \to \infty$ (infinite is vast enough!). In case dynamical problems are considered, the limit to macroscopic timescales ($t \to \infty$) has to be taken as well. That is, the timeframe of observation has to be extended to the scale at which the dynamics of the system starts to reflect macroscopic dynamics. In some cases, the order in which both limits should be taken ($N \to \infty$ and $t \to \infty$) is not trivial. We will encounter an example of this in *Chapters 8 and 9*.

With the advent of computer simulations such as Molecular Dynamics [2,3] it became for the first time possible to actually test analytical theories and the assumptions that had been made in solving their equations. Any proposed model system was put into the computer and its static and dynamic properties were measured via a 'computer experiment'. The outcomes were then compared to the theoretical predictions. In such simulations, however, reaching the thermodynamic limit is not trivial. By nature, one is restricted to finite sizes and several tricks have been invented to mimic a bulk system. Even then, every reliable computer simulation should in principle be complemented by some account of finite size effects. A large part of the present thesis will be devoted to questions of this kind.

Crystal growth and diffusion in zeolites

Although many of the (bulk) properties of materials are indeed controlled by the overall statistical average of the underlying microscopic dynamics, some of their properties depend upon the exceptions. In this thesis we encounter two such examples: solidification processes and the transport of molecules through confined geometries that are themselves of molecular size. In both cases, it is the local microscopic dynamics that governs the properties of interest, even in the macroscopic limit.

Part II of this thesis deals with the calculation of the growth rate of the (100) face of an FCC crystal of spherical particles in contact with its melt. In the growth of crystals, it is the microscopic processes taking place at the interface that determine the macroscopic morphology of the crystal as a whole. No matter how large the two bulk phases (i.e., crystal and melt) are, the interface extends over at most several interatomic distances, so any theory aiming at the prediction of crystal morphology should be of microscopic nature. Although many (thermodynamic) theories have been developed in the past to calculate a crystal's *equilibrium morphology* — theories which were solely based on bulk properties like lattice energies and bond energies — a growing crystal is never in thermodynamic equilibrium with its environment. As a consequence, most crystals have a kinetic growth form which will be bounded by the slowest growing faces. For a prediction of this *growth morphology*, one needs to be able to calculate the growth rates of individual planes of the crystal. In this thesis we will do so for one particular example and we will focus on different ways to set up the simulations and to extract the desired quantities.

Part III of this thesis deals with the transport of small molecules (methane and argon)

through the channels of a nanoporous zeolite ($AlPO_4$-5). Zeolites are crystals with well-defined pores of molecular dimensions, which makes them perfectly suited for use as molecular sieves or shape-selective catalysts. Their crystalline nature makes the pores essentially monodisperse, in contrast to disordered alternatives like porous carbon or polymer membranes. For a good understanding of their overall behaviour, it is of the utmost importance to understand the transport processes taking place when guest molecules move through zeolitic pores. Because of the molecular confinement, the phase of the guest molecules is completely different from a normal bulk phase (like gas, liquid, or solid), which leads to a wealth of new transport phenomena. Moreover, due to the confinement, some thermodynamic concepts that apply to bulk phases, like for instance the pressure, completely lose their meaning.

In our example $AlPO_4$-5, all pores are aligned and they do not intersect each other. Their diameters range from ca. 7 nanometers at the narrowest passages (the 'windows') to ca. 10 nanometers at the widest passages. We will study the self motion and collective motion of guest molecules in this system. In the case of self motion, we look at the implications for (anomalous) diffusion when the adsorbents are of such size that two molecules can just pass each other in the pores. In the case of collective motion we look at the influence of correlations between the pathways of the adsorbents. Like in Part II, the focus will be on the proper setup of the computer experiments and on various ways to extract the desired properties.

Simulations

The methodology used throughout this thesis is Molecular Dynamics (MD) simulations [5, 60]. In that scheme, Newton's equations of motion are numerically solved for a large number of interacting particles (nowadays typically between 1000 and 100,000 particles). Statistical averages can be measured from the obtained distributions of configurations and momenta to extract thermodynamic properties. They could also be calculated by other sampling methods, such as Monte Carlo, but the MD method, since it describes the real motion of the particles, has the advantage that information on the *dynamics* of the system can be obtained. It is the dynamical properties that we are mainly interested in: crystal growth rates in Part II and diffusion coefficients in Part III.

Molecular dynamics simulations as just described can strictly speaking only yield trajectories in the NVE ensemble (i.e., constant number of particles N, constant volume V, and constant energy E), since Newton's laws obey conservation of energy. Today several routines are available to modify the dynamics of the particles such that systems can also be studied in other ensembles [18, 87, 139]. This makes it easier to connect to experimental practices. Simulations at constant temperature T, constant pressure P, or constant chemical potential μ can now routinely be performed. We will use canonical (NVT) ensemble simulations in *Chapters 2, 5, 7, 8, and 9* and NPT simulations in *Chapters 2, 3, and 4*. In the limit of very large system sizes (the thermodynamic limit), all ensembles will give the same average results. With the restriction of finite sizes inherent in simulations, however, a choice for the most appropriate method has to be made in each particular case under study.

In search of the macroscopic limit

In order to obtain macroscopic properties from simulations at microscopic time and length scales, one has to take care to ensure that extrapolation of the results to the macroscopic level is justified. Small discrepancies in the sampled distributions or in the averaging procedure may develop into quantitative errors on large scales, and are therefore to be avoided. This is particularly important when large collective motions play a role in the simulations, which is the case in both our systems. In crystal growth simulations, entire planes of molecules are restructuring and correlation lengths extend over several atomic diameters. The presence of a crystal-melt interface, for example, induces structure far into the liquid. In the simulation of transport in zeolites, collective motions are associated with the calculation of the transport diffusivity.

As an example of changing behaviour with changing timescales, in *Chapter 7* we study the tracer diffusion of methane in the pores of $AlPO_4$-5. These molecules are of such size that they have great difficulty passing each other. For the mean square displacement of the particles we find a time dependence close to the theoretical value for particles that cannot pass at all. On a very long timescale, however, the infrequent passings start to dominate the dynamics and a normal diffusion regime is recovered. In other to reach this regime, we switch from MD simulations to a coarse-grained hop-and-cross model, using input parameters derived from the atomistic MD simulations.

Transport diffusion describes the collective motion of particles under the influence of a concentration gradient. One intuitive way to try to calculate the transport diffusivity is to impose a gradient and measure the resulting steady-state flux. One major problem, however, is that gradients that are small on the microscopic level of the simulation are often extremely large on a macroscopic level. For that reason, the system is likely to reach the regime where it does not respond linearly anymore and does not obey the linear transport equation (in this case Fick's law). Therefore we look in *Chapters 8 and 9* at equilibrium methods; we study the decay of spontaneous fluctuations in the system and investigate how the measured diffusivity depends on the wavelengths of the fluctuations. The regime where the diffusivity is independent of the wavelength is then associated with linear response.

A similar situation arises in the calculation of a crystal growth or melting rate; this is also a nonequilibrium property, which can be measured by applying a nonequilibrium condition (e.g., a temperature below or above the melting temperature) and measuring the steady-state rate with which the system grows in either direction. In our system with soft interactions, however, the rates are so high that it is difficult to reach the proper steady state. Therefore, we introduce in *Chapter 2* an equilibrium method to extract the kinetic coefficient from the fluctuations of the interface at equilibrium. The method is discussed in more detail in *Chapter 5*. In the interjacent chapters, we develop ways of setting up nonequilibrium simulations such that they give the most accurate results (which can then be compared to the results from the equilibrium method). Since the growth and melting rates are so high, the whole system soon becomes occupied by one phase. Therefore the nonequilibrium simulations are restricted to short run times and it is extremely important to set up a well-equilibrated interface right from the start. In fact, we find two time-regimes: one in which the system relaxes to its nonequilibrium steady-state, and one in which the macroscopic growth mechanism prevails.

To summarize: the main scope of this thesis is to develop methods that can give reliable results on macroscopic nonequilibrium properties. In order to do so, we look at equilibration procedures, system size effects, transformation of behaviour over timescales, and limits imposed by assumptions of linear response. Both Part II and Part III start with a historical overview of the relevant field, outlining the most relevant theories, and ending with an outline of subsequent chapters.

Part II

Growth and melting at the Lennard-Jones (100) surface

1 Crystal growth investigations: a historical perspective

In this chapter, a historical account will be given of investigations that led to the present-day understanding of crystallization and melting processes. The focus will be on one-component crystals in contact with their pure melts. We will describe the experiments that were carried out and the theories that were developed from the end of the nineteenth century up till the present day, occasionally pointing at questions that remained open and anticipating the issues that will be addressed in subsequent chapters. In the final section, an outline will be given of the chapters to follow.

1.1 The early years

In the final decade of the nineteenth century, the theory of evaporation of liquids and condensation of gases had come to a close. The experiments of Th. Andrews on the volume change upon evaporation of carbon dioxide up to the critical point of the coexistence line had laid the foundation for the theoretical work of J.D. van der Waals. His masterpiece *"Over de continuïteit van den gas- en vloeistoftoestand"*[1] in turn formed the inspiration for many experimentalists thereafter. It was shown that both the volume change ΔV and the latent heat of evaporation ΔH^{vap}, following the liquid-vapour coexistence line, decrease with increasing temperature and pressure. This goes on up to the critical point, where both ΔV and ΔH^{vap} vanish. Below the critical point, a substance separates into two isotropic phases; above, the phases become indistinguishable and no separation occurs. Given the success of the van der Waals theory, several scientists tried to translate it to the theory of crystallization, but it soon turned out that every attempt to do so failed.

One of the first to anticipate that the transformation of a gas into a liquid might be fundamentally different from the transformation of a liquid into a crystal was Gustav Tammann. At the beginning of the previous century, he covered a whole range of experimental data and theoretical considerations in two subsequent books [164, 165]. He posed the hypothesis that a critical point, where the crystal becomes identical to its melt, could not exist on the melt-

1 "On the continuity of the gas and the liquid phase"

ing curve. The hypothesis was deduced from knowledge of the behaviour of substances in isotropic and anisotropic phases, and was supported by experiments. He reported on findings that, on the melting curve of sodium sulphate, ΔV goes through zero, while at the same time ΔH remains positive. Conversely, by the transformation of two crystal polymorphs of water, silver iodide, or phenol, despite substantial volume differences of the polymorphs, ΔH goes through zero at a certain point on the transformation curve. Note that at that time, a direct search for critical points on the crystal-liquid coexistence curve was out of reach: the strongest known material by then was steel, which made it possible (in very small set-ups) to reach pressures of 12000 $\mathrm{kg/m^2}$ maximum, still well below the pressures at which possible critical points were expected.

Tammann clearly distinguished isotropic states of matter from anisotropic ones, thereby strongly opposing to the use of the word 'solid'. This was still used by many authors to refer to both the crystalline and the glassy state, while those could already be clearly distinguished experimentally. Glasses show anisotropic, scalar properties, while crystals display direction dependent, vectorial properties. It was known that, in such anisotropic phases, molecules vibrate around points that are ordered according to space groups. Tammann argued that since there exists only a distinct, limited, number of space groups, it would not be possible to have a continuous change between different states. A transformation of an isotropic to an anisotropic state, or a transformation between two anisotropic states, must therefore proceed discontinuously, thus ruling out the possible existence of a critical point.

Tammann reported on experiments where the growth of crystals in time was followed. It was found that, for neatly conducted experiments, crystals grew at a constant rate, the value of which was temperature dependent. In those days it had already been established as common knowledge that the macroscopic shape of crystals depends very much on their building history; if temperature distributions around the sample were different in separate experiments, totally different macroscopic forms could evolve. Tamman concluded from this that the temperature dependence of growth rates must differ for different directions of growth. This was indeed shown experimentally to be the case. The first measurements of growth rates at different temperatures were conducted by Gernez on rhombic and yellow phospor [65] and by Moore on phenol and acidic acid [131]. Their finding that the growth rate R increased with decreasing temperature T was first considered a mystery (!) since up till then all transformation processes in nature had been found to slow down upon lowering the temperature. Friedländer and Tammann did similar experiments on benzophenon, which grows much slower, allowing them to study growth at as much as 100 degrees undercooling. For low enough temperatures, the rates were shown to level off to a plateau value. This was explained by the fact that growth in this case should be heat transport limited. Therefore the bath temperature might be far off the actual temperature at the interface. Indeed, when the test tube was taken smaller (allowing better heat transport away from the interface) higher rates could be found.

The temperature dependence of the macroscopic crystal shape was neatly shown in experiments by R. Nacken. He put a copper wire in an undercooled salol melt. (Salol is the commercial name for phenyl-*o*-hydroxybenzoate, $C_6H_4(OH)CO_2C_6H_5$, a crystalline ester that is used as a stabilizer in plastics and medicines). At 0.5 degree undercooling, the crystalline surface was rounded off, showing that at very small undercooling, all growth rates

become equal. When the undercooling was increased the crystal started to facet. At 1.5 degrees undercooling a nice polyhedron was found. If the undercooling was higher than 2 degrees the crystal became increasingly thread-shaped. The variance in rates had become so large that the fastest growing planes disappeared from the outer shape.

Finally, in Chapter 9 of Tammann's second book [165], he introduced some theoretical considerations on the temperature dependence of growth and melting rates very close to equilibrium. Based on considerations of heat transport, he predicted that *the dependence should be linear, with the same slope for crystallization and melting*. This will be a major issue in *Chapters 3 and 4* of this thesis.

It is amazing how many of the issues and questions that are still around today (both in simulations and in the interpretation of experiments) were already anticipated in some way or another at the time Tammann wrote his volumes. To summarize, we mention the most relevant ones for the present thesis:

- The temperature dependence of growth rates is different for different crystal planes. (Since around the 1950's, the distinction is made between *equilibrium morphology*, which is the crystal shape that can be predicted from a consideration of binding energies of all surfaces, *growth morphology*, which is the actual shape that arises from experimental growth conditions, and *dissolution morphology* which develops when existing crystals are (partly) dissoluted. See also Frank [59].)

- It is important to consider the possible influence of heat transport on growth and melting rates. A clear distinction should be made between the bath temperature and the temperature at the interface.

- It was anticipated that the temperature dependence of growth and melting rates should not change discontinuously upon crossing the equilibrium temperature. (Note that this contains the implicit assumption that crystallization and melting are fundamentally the same process.)

1.2 The Wilson-Frenkel theory

As soon as the influence of temperature conditions on the growth morphology was recognized, people started to think about theories that could explain, or even predict, the trends that were seen in experiments. The earliest theories concentrated on growth from the vapour, since the rates are generally much lower and the crystal-vapour interface is far more accessible for experiments. Hertz [83] and Knudsen [112] proposed that the net rate of growth was just the difference between the rate of arrival of atoms and the rate of evaporation. The analogue for melt growth was first given by Wilson [190], who assumed that particles had to overcome a diffusional barrier in order to make the transition from the liquid to the solid phase. The rate of incorporation of atoms in the crystal lattice is then given by

$$R_c(T) = a\nu \exp\left(-\frac{Q}{k_B T}\right), \tag{1.1}$$

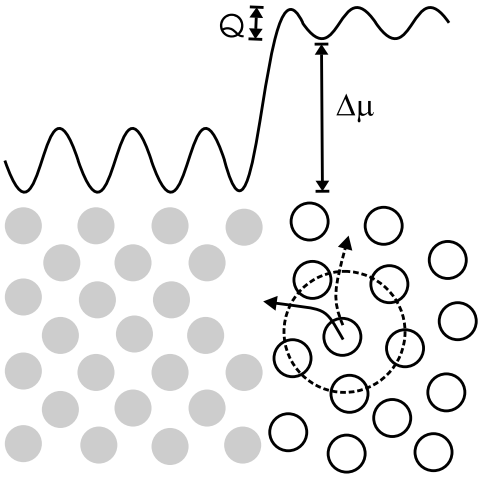

Figure 1.1: Pictorial representation of the incorporation of an atom from the liquid (white circles) into a vacant site in the crystal (grey circles). In a cartoon of the free energy profile, the chemical potential difference between liquid and crystal is depicted, as well as the barrier to incorporation. The arrows represent the idea behind the Wilson-Frenkel theory that the barrier to incorporation is equal to the barrier to self-diffusion in the liquid.

with a some characteristic length, ν the attempt frequency and Q the diffusional barrier.

This process is counteracted by particles that move from the crystal to the liquid. Since the Gibbs free energy per molecule, the chemical potential $\mu = G/N$, is higher in the liquid than in the crystal, the rate of melting will be smaller than the rate of crystallization by a factor $\exp(-\Delta\mu/k_{\mathrm{B}}T)$:

$$R_m(T) = a\nu \exp\left(-\frac{Q}{k_{\mathrm{B}}T}\right) \exp\left(-\frac{\Delta\mu}{k_{\mathrm{B}}T}\right). \tag{1.2}$$

Note that it is implicitly assumed that the attempt frequency for both processes is the same. Wilson took ν to be equal to the frequency of atomic lattice vibrations. The net rate of growth is thus given by:

$$R(T) = R_c(T) - R_m(T) = a\nu \exp\left(-\frac{Q}{k_{\mathrm{B}}T}\right)\left[1 - \exp\left(-\frac{\Delta\mu}{k_{\mathrm{B}}T}\right)\right]. \tag{1.3}$$

Independently, Frenkel [61] derived a similar expression where the activation barrier was based on the viscosity of the melt. The Wilson and Frenkel formulae can be shown to be equivalent using the Stokes-Einstein formula derived by Einstein in his famous 1905 article [50], where the self-diffusion coefficient is related to the viscosity:

$$\nu a^2 \exp\left(-\frac{Q}{k_{\mathrm{B}}T}\right) = D = \frac{k_{\mathrm{B}}T}{6\pi\eta a}. \tag{1.4}$$

The idea behind equating the activation energy for diffusion with that for incorporating an atom in the crystal is illustrated in Fig. 1.1. For both processes the atom needs to break out of the cage of neighbours in the liquid. Note that D in this case stands for the *self*-diffusion coefficient, associated with the motion of a 'tracer' particle surrounded by a bulk of like particles. Self diffusion does not represent net transport, hence the diffusional barrier in the Wilson-Frenkel theory should not be confused with so-called 'diffusion limited growth'. The

latter can be encountered in growth from solution when the *collective* diffusion coefficient is so small that material transport to the interface becomes rate limiting. This distinction is often not made clear when the Wilson-Frenkel formula is discussed in the literature. (For a more general account of self- and transport diffusion, see *Chapters 8 and 9*).

In most present-day representations of Eq. 1.3, one finds not the chemical potential μ, but the latent heat of fusion per atom l (which can be measured experimentally). The latent heat of fusion is the amount of energy released during crystallization at the melting point at constant pressure, and consists of an internal energy part and work done on the crystal:

$$l = \Delta u + P\Delta v = \Delta(u+Pv)_P = h_l^{\mathrm{eq}} - h_s^{\mathrm{eq}}. \tag{1.5}$$

At equilibrium, the chemical potential $\mu = G/N = h - Ts$ of both phases is equal, so that

$$l = T^{\mathrm{eq}}\left(s_l^{\mathrm{eq}} - s_s^{\mathrm{eq}}\right) = -T^{\mathrm{eq}}\left\{\left(\frac{\partial \mu_l}{\partial T}\right)_P^{\mathrm{eq}} - \left(\frac{\partial \mu_s}{\partial T}\right)_P^{\mathrm{eq}}\right\}, \tag{1.6}$$

showing that the crystal-liquid transformation is a first-order phase transition (because there is a discontinuity in the first derivative of the thermodynamic potential). Now, expanding $\Delta\mu$ up to first order in the temperature around equilibrium leads to:

$$\begin{aligned}\Delta\mu = \mu_l - \mu_s &\approx \mu_l^{\mathrm{eq}} + \left(\frac{\partial \mu_l}{\partial T}\right)_P^{\mathrm{eq}}(T - T^{\mathrm{eq}}) - \mu_s^{\mathrm{eq}} - \left(\frac{\partial \mu_s}{\partial T}\right)_P^{\mathrm{eq}}(T - T^{\mathrm{eq}}) \\ &= -\frac{l}{T^{\mathrm{eq}}}(T - T^{\mathrm{eq}}).\end{aligned} \tag{1.7}$$

Finally, the Wilson-Frenkel formula can be transformed to give

$$R^{\mathrm{WF}}(T) = fd\frac{D_{\mathrm{self}}(T)}{\lambda^2}\left[1 - \exp\left(\frac{l}{T^{\mathrm{eq}}}\frac{(T - T^{\mathrm{eq}})}{k_{\mathrm{B}}T}\right)\right], \tag{1.8}$$

where d stands for the interlayer spacing, λ the diffusional mean free path, and f the effectiveness facter, which is included to account for the effect that not all atoms that cross the boundary will stick there and/or not all sites on the surface might be active growth sites. It should be remembered that the above formula is an approximation and therefore principally more limited to temperatures close to equilibrium than Eq. 1.3.

Jackson in 1975 [94] followed a slightly different route to derive an analogous expression, which in the end contains an extra entropy factor. He suggested that $\Delta\mu$ in Eq. 1.3 should be replaced with the enthalpy of fusion per atom, l. For the transformation rate from crystal to liquid, he wrote

$$R_m = R_m^0 \exp\left(-\frac{Q}{k_{\mathrm{B}}T}\right)\exp\left(-\frac{l}{k_{\mathrm{B}}T}\right), \tag{1.9}$$

and for the reverse process

$$R_c = R_c^0 \exp\left(-\frac{Q}{k_{\mathrm{B}}T}\right). \tag{1.10}$$

From the equilibrium condition $[R_m(T^{\rm eq}) = R_c(T^{\rm eq})]$ one can derive

$$R_c^0 = R_m^0 \exp\left(-\frac{l}{k_{\rm B}T^{\rm eq}}\right). \tag{1.11}$$

Taking the prefactor R_m^0 equal to $a\nu$ and taking the net rate as the difference between the two competing rates leads to

$$\begin{aligned} R^{\rm J}(T) &= a\nu \exp\left(-\frac{Q}{k_{\rm B}T}\right) \exp\left(-\frac{l}{k_{\rm B}T}\right) \left[1 - \exp\left(-\frac{l(T-T^{\rm eq})}{k_{\rm B}TT^{\rm eq}}\right)\right] \\ &\approx a\nu \exp\left(-\frac{Q}{k_{\rm B}T}\right) \exp\left(-\frac{\Delta s}{k_{\rm B}}\right) \left[1 - \exp\left(-\frac{l(T-T^{\rm eq})}{k_{\rm B}TT^{\rm eq}}\right)\right] \\ &\Rightarrow f d \frac{D_{\rm self}(T)}{\lambda^2} \exp\left(-\frac{\Delta s}{k_{\rm B}}\right) \left[1 - \exp\left(-\frac{l(T-T^{\rm eq})}{k_{\rm B}TT^{\rm eq}}\right)\right], \end{aligned} \tag{1.12}$$

where in the last line the effectiveness factor f has again been included. In a study of silicon solidification and melting with the Stillinger-Weber potential, Grabow *et al.* [68] showed that the Jackson modification (Eq. 1.12) behaved better than the original Wilson-Frenkel form (Eq. 1.8). In fact, it is this Jackson form that most people refer to when discussing the Wilson-Frenkel theory.

1.3 Microscopic models

Though the Wilson-Frenkel theory was motivated by microscopic considerations (like the barrier to diffusion and the description as two competing processes at the interface), it is basically thermodynamic by nature. For instance, it is not easily seen how one could extend it to account for different growth rates of different interfaces (except, perhaps, via the lattice spacing d and the effectiveness factor f). It was soon recognized that more microscopic theories would be necessary. People started thinking about the details of the interface and realized that if a crystal had smooth faces (even at the atomistic level), growth would proceed by the formation of islands on the surface and subsequent growth of the islands. In that case, the nucleation of islands would be rate limiting and not the incorporation of atoms at random lattice sites. In fact, it was Gibbs who already suggested that "there could be a difficulty in the formation of a new layer", but that remark ended up in a footnote of his work [66] and was overlooked for decades.

The process of two-dimensional nucleation depends on the chance that two atoms on a surface meet. The growth rate would then be proportional to $(\Delta T)^2 = (T - T^{\rm eq})^2$ instead of linear in ΔT (as Tammann suggested for all growth close to equilibrium). These ideas were first tested for growth from the vapour, where conditions are normally such that surface diffusion is fast compared with the deposition of atoms. Indeed, experimental observations clearly showed the quadratic dependence. Quantitative rates, however, were always much higher than predicted, a problem which long remained unexplained. A breakthrough came when Frank [58] pointed out that lattice misfits might play a major role in growth. He suggested the mechanism of spiral growth in the following words: "The presence of a dislocation

with a component of its Burgers vector normal to the crystal surface provides, around its point of emergence, a perpetual step that can move but which cannot be eliminated by growth". Indeed, with his theory, rates were predicted that were in close agreement with experimental observations. But, even in vapour growth, which mostly proceeds by the above mechanism at smooth surfaces, it is possible to find a regime where the smoothness of the interface is lost. At very large undercoolings, the deposition of atoms on the surface can become so fast that it exceeds the rate of diffusion along the surface. In that case, atoms are incorporated at any point on the surface and the growth rates are linear in ΔT. This transition is called kinetic roughening. A comprehensive account of all early theories on vapour growth processes was published in the famous paper by Burton, Cabrera, and Frank [33].

Jackson pointed out that for a crystal growing from its melt, the equilibrium interface structure is that which is in equilibrium with both the crystal and the melt [93]. Applying a simple mean-field approach to a single-layer model of the interface, he developed a qualitative understanding of the roughening transition (i.e., the temperature below which the interface is smooth and above which the interface is atomically rough). We will briefly sketch the derivation here, largely following the representation of Saito [152] (with somewhat different notation).

In the Jackson model, the interface is described as a collection of N sites on which N_s atoms are adsorbed. Each site has a coordination number z_s. On average, for each atom, $(1-N_s/N)z_s$ neighbouring sites are empty, which corresponds to an energy cost (with respect to a totally filled, smooth lattice) of

$$\Delta U = U_{\mathrm{bond}}(1-N_s/N)z_s N_s, \tag{1.13}$$

where $2U_{\mathrm{bond}}$ is the energy associated with one 'crystal bond' between neighbouring atoms. (In this crude model, only nearest-neighbour interactions are taken into account). Apart from the energy cost, there is an entropy gain associated with the number of configurations that N_s atoms can take on N sites:

$$\begin{aligned}\Delta S = k_{\mathrm{B}}\ln\Omega &= k_{\mathrm{B}}\ln\frac{N!}{N_s!(N-N_s)!}\\ &\approx k_{\mathrm{B}}\left[N\ln N - N_s\ln N_s - (N-N_s)\ln(N-N_s)\right],\end{aligned} \tag{1.14}$$

where we have used Stirling's approximation to lose the factorials.

The bonding energy U_{bond} is related to the latent heat per atom l by $l = zU_{\mathrm{bond}}$, where z is the coordination number in the bulk crystal. Now Jackson introduced the roughening temperature as

$$T_R = \frac{z_s l}{2zk_{\mathrm{B}}}. \tag{1.15}$$

The free energy difference $\Delta F = \Delta U - T\Delta S$ between the smooth interface and the interface with N_s atoms adsorbed can now be expressed as a function of the fraction of occupied sites $\phi = N_s/N$:

$$\frac{\Delta F}{Nk_{\mathrm{B}}T_R} = 2\phi(1-\phi) + \frac{T}{T_R}\ln(1-\phi) - \frac{T}{T_R}\phi\ln\left(\frac{1-\phi}{\phi}\right) \tag{1.16}$$

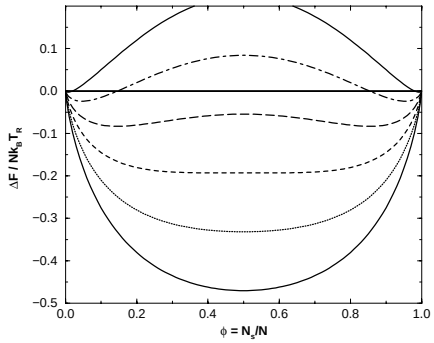

Figure 1.2: Free energy between the smooth and the non-smooth interface as a function of the fraction of occupied sites. Shown are various temperatures; from top to bottom: $T/T_R = 0.4$, 0.6, 0.8, 1.0, 1.2, and 1.4, respectively.

The relationship is shown graphically in Fig. 1.2. It can be seen that for $T < T_R$ there are two free energy minima, corresponding to an almost empty and an almost full interface (both can be regarded smooth). For $T > T_R$, there is one minimum at $\phi = 0.5$, corresponding to a rough interface.

Jackson also introduced a parameter α (the 'Jackson α-parameter') which is a material property, but also depends on the specific crystal plane (via the surface coordination number z_s):

$$\alpha \equiv \frac{z_s l}{z k_B T^{eq}} = \frac{2T_R}{T^{eq}} \tag{1.17}$$

For surfaces with $\alpha > 2$ the melting point is below the roughening temperature and the interface should be flat at all temperatures. If $\alpha < 2$, the interface should be rough when the experiment is carried out at temperatures sufficiently close to equilibrium. For all metallic crystal-melt interfaces $\alpha < 2$, and rough growth is indeed found experimentally. For some organic crystals, like salol and glycerol, smooth interfaces are found. The Lennard-Jones (100) interface which is the main topic of this thesis has values $z_s = 4$, $z = 12$, and $l = 1.115\,\varepsilon/k_B$, which leads to a roughening temperature of $T_R = 0.186\,\varepsilon/k_B$, well below the melting temperature of $T^{eq} = 0.6972\,\varepsilon/k_B$ (at a pressure of $P = 2.512 \times 10^{-3}\,\varepsilon/\sigma^3$). For the calculation of these Lennard-Jones bulk properties see *Chapter 5*.

It is obvious that the Jackson model is an oversimplification. It accounts for only one layer and treats every site equivalently. Many improvements have been made upon the model, such as including the possibility of multiple layers. This was done first by Burton, Cabrera, and Frank [33] and later by Temkin [167]. Although all kinds of critical phenomena change when more detail is included in the model, the roughening temperature does hardly change quantitatively. Thus the Jackson parameter remains a convenient criterion for surface roughening.

Around the 1960's, many of the existing ideas and theories on growth from the melt were collected in the papers by Jackson and Chalmers [35, 92]. To summarize, the possible types of crystal growth had been grouped into three classes:

rough growth When the temperature of the experiment is below the melting temperature but

above the roughening temperature, the interface is rough and the growth rate depends linearly on the temperature: $R(T) \propto \Delta T$.

smooth growth When the temperature of the experiment is below the roughening temperature, the surface is smooth and the process of crystallization is governed by two-dimensional island nucleation and surface diffusion. Incorporation of atoms is most likely at steps and kinks on the surface. The spiral growth mechanism, in which steps cannot grow out of the surface, accounts for the moderate rates that can still be observed. The growth rates are proportional to the square of the undercooling: $R(T) \propto (\Delta T)^2$.

kinetic roughening Even for initially smooth surfaces, at very large undercoolings the interface can become rough because the rate of arrival of atoms at the surface exceeds the transport by surface diffusion. The growth rates again become linear in the undercooling: $R(T) \propto \Delta T$.

The above state of theories in the 1960's would seem to present a clear starting point for experimental observations (and possible falsifications). This was a serious problem, however, since the solid-liquid interface is hardly accessible to experiments, both in terms of the location of the interface and of measuring the actual interface temperature. At this point in time, in order to be able to test existing theories, new methods had to be found that could provide information with atomic detail.

1.4 Computer experiments

With the advent of molecular dynamics simulations by Alder and Wainwright [2,3] in the late 1950's, a whole new route was opened to investigate the dynamics of atomistic systems. By solving the many-body problem numerically for a few hundred hard spheres, they were able to test and reproduce the results of several existing analytic theories. For equilibrium properties an alternative route was already available in the Monte Carlo method, but the advantage of being able to follow the dynamic evolution of the system was obvious. Already in a preliminary letter (before the method was described in detail), they reported on the discovery of a phase transition in the hard sphere system [2]. This was clearly a remarkable result and a great promise for future applications of the method.

In their 1959 paper [3] they report, besides on the advantages, also on the limitations of the method, some of which play a major role in the present thesis. They argue: "In phase transition regions the artificial inhibition of density fluctuations caused by maintaining a constant number of molecules in the box can be serious", and "... in order to examine the properties of a heterogeneous system it is necessary to use many more particles than in the case of a single phase system".

Mainly due to the above limitations and the state of computer technology, it took a long time before the properties of the interface between two thermodynamic phases could be examined by molecular dynamics simulations. Among the first to do so were Ladd and Woodcock [116] in 1977, who managed to create a 3-phase Lennard-Jones system at the triple

point. They employed a hard wall on one side of the box and a free boundary on the other side, while employing periodic boundary conditions in the remaining two directions. The results were shown to be in reasonable agreement with Monte Carlo results of Hansen and Verlet from 1969 [77]. This can be seen as the first demonstration of the possibility to simultaneously simulate both bulk and surface with the limited system sizes manageable in molecular dynamics. Reservations were made, however, to the exact quantitative data. Indeed, in a subsequent paper [117] they showed that more extensive equilibration resulted in significant changes in the coexistence properties. However, the basic conclusions about the nature of the crystal-liquid interface remained unchanged. From a detailed examination of the density profiles, it was found that the solid-liquid interface of the Lennard-Jones system was significantly more diffuse (extending over 7 to 8 atomic diameters) than was usually assumed. The authors justly stated that their profiles represented a thermal average and could therefore not unequivocally decide upon the validity of existing theories, but the power of the molecular dynamics method in the study of interfaces was established. (Note that we will address the issue of the difference between time-averaged and instantaneous interface profiles in *Chapter 5*, Sec. 5.5).

The study of the Lennard-Jones solid-liquid interface was taken over by a former student from the group of Woodcock, Jeremy Q. Broughton [26]. First together with Bonissent and Abraham and later with Gilmer and Jackson, a series of papers were published which are still heavily cited today [27–32]. They performed an extensive study of the bulk properties of the Lennard-Jones FCC crystal and liquid. Subsequently they studied steady-state growth rates for the (100) and (111) face at several temperatures (albeit all below the melting temperature), and finally calculated the excess surface free energy. In their study of the temperature dependence of growth rates for the (100) surface, they tried to fit their data to the Wilson-Frenkel formula. They concluded however, that no energy barrier could be found that prevents the liquid atoms from reaching the lattice sites. Instead they proposed a new form, where the diffusion factor in the Wilson-Frenkel formula is replaced by a factor proportional to the average thermal velocity of the atoms, which could be fitted to give excellent agreement with their data:

$$R(T) = \frac{d}{\lambda}\left(\frac{3k_{\mathrm{B}}T}{m}\right)^{1/2} f_0 \left\{1 - \exp\left(-\frac{\Delta\mu}{k_{\mathrm{B}}T}\right)\right\}, \tag{1.18}$$

where λ is the actual mean distance the particles have to travel (taken to be 0.4 times the interlayer spacing d) and f_0 is an effectiveness parameter which was fitted at 0.27.

After the evident success of the above investigations, many more simulations followed on various crystal/liquid systems. At this point we will name only a few: Crystal growth rates were measured in the Lennard-Jones system (growth from pure melts and/or solutions) by Báez and Clancy [7] and Huitema *et al.* [88–90], in metallic crystal-melt systems (Na and Si) by Kluge, Tymczak, and Ray [111, 177, 178], and in the hard-sphere system by Mori [132]. Detailed measurements of the interface structure were performed in the Lennard-Jones system by Huitema *et al.* [90], in the hard-sphere system by Davidchack and Laird [45, 46], in aluminium by Jesson and Madden [96, 97], and in the water/ice system by Hayward and Haymet [82]. Besides molecular dynamics, several other methods have been applied to understand the atomic processes at the interface, such as lattice gas models [133], and (dynamic)

Density Functional Theory [141, 157–159]. At this point, we will not go into further detail of those recent investigations. The relevant papers will be discussed at appropriate points in subsequent chapters. For further reading we refer to a number of reviews [81, 95, 118, 121] and books [124, 152] and references quoted therein.

1.5 Outline of subsequent chapters

In this part of the thesis our main concern will be how to calculate the correct rates of growth and melting in the macroscopic limit from molecular dynamics simulations. As a model system we will use the Lennard-Jones FCC (100) surface in contact with its pure melt.

The obvious choice for the setup of a simulation would be one that resembles a real experiment as closely as possible. A system could be constructed with two phases in contact with each other. This system could be initiated at a desired off-equilibrium state point and the growth (or melting) rate could then be measured while running at constant temperature and pressure. There are, however, several problems associated with such a nonequilibrium simulation. For instance, it is not trivial to construct and maintain a nonequilibrium steady state or to impose a gradient in the box that is both large enough to obtain good measurements and small enough to represent macroscopic gradients. Second, unless countermeasures are taken, the length of a growth simulation is basically limited to the time over which the whole simulation box becomes crystalline, which imposes severe limitations to the accuracy that can be reached even at moderate amounts of undercooling or superheating.

For the above reasons we will develop an alternative route in *Chapter 2*. We will present a method to extract the nonequilibrium kinetic coefficient for growth from the fluctuations of the interface in an equilibrium simulation. We will show that good agreement can be reached between the predictions of this method and the results from seperate nonequilibrium simulations. The equilibrium method has as its main advantage that the simulations can essentially be run *ad infinitum*, providing as accurate statistics as one wishes.

The proposed method will only be feasible in cases where the temperature dependence of the growth rates is linear and does not show a slope-discontinuity upon crossing the equilibrium temperature. The linear dependence of T is fulfilled for any face growing above the roughening temperature, which is the case for our model system (see Sec. 1.3). Although it was early anticipated (see Sec. 1.1) that a slope discontinuity of growth and melting rates could not exist, this has been the source of much debate in the literature. A singularity at the melting temperature was for instance claimed by Tymczak and Ray [177, 178] in their study of crystallization and melting kinetics of sodium. We will investigate this in *Chapter 3*, where we study growth and melting rates close to equilibrium by means of nonequilibrium simulations. We will look closely at the influence of the equilibration procedure, connecting with the observation of Ladd and Woodcock (Sec. 1.3) that different equilibration times can result in significant changes in the coexistence properties (though they did not look at dynamics). We will show in our simulations that improper equilibration of the two-phase system can lead to an apparent slope discontinuity, which can entirely be explained by the difference in the amount of lattice imperfections between the bulk crystal and the crystal as used in the two-phase simulations.

In *Chapter 4*, we will elaborate on this finding and present very accurate simulations of the growth and melting rates close to equilibrium. We will rule out the existence of a slope discontinuity for the Lennard-Jones (100) surface. We will also do a study of the effect of system size on the growth kinetics, relating to the remark by Alder and Wainwright (Sec. 1.3) that "in order to examine the properties of a heterogeneous system it is necessary to use many more particles than in the case of a single phase system". We will report on the discovery of two regimes of linear growth: a short-time regime which is associated with interface relaxation and a long-time regime associated with the macroscopic limit of growth and melting. For sufficiently large simulation systems both regimes can in principle be measured. In a system of $8.044\sigma \times 8.044\sigma \times 69.595\sigma$ (4048 atoms) — which is already larger than used in most simulations — the initial regime lasts much longer than in a system of twice the size in the growth direction. This makes an accurate calculation of the long-time dynamics in the smaller system rather difficult.

Given the accurate measurements of both regimes from the nonequilibrium simulations, we return to the equilibrium method in *Chapter 5*. Although very long simulations are required to obtain accurate autocorrelation functions over a sufficiently large time interval, the equilibrium method also shows two regimes. The kinetic coefficients for both the interface relaxation and the long-time dynamics agree well with the nonequilibrium results. The derivation of the method as proposed in *Chapter 2* is reconsidered and slightly modified. A factor that could previously only be calculated by reference to separate bulk simulations is now replaced by a correlation function relating number fluctuations to pressure fluctuations, which can directly be measured from the equilibrium two-phase simulation.

2 Equilibrium and nonequilibrium simulations

On the basis of Onsager's hypothesis a new method is presented to calculate growth rate constants of various crystal faces from the fluctuations of interfaces during NVT simulations. The method is applied to the (100) face of a Lennard-Jones crystal grown from the melt. The results are in good agreement with those obtained by means of NPT nonequilibrium simulations. The new method allows for much better statistics at the cost of much less computation time. The use of Onsager's hypothesis to derive the microscopic expression for the growth rate constant may serve as an example for applications in other fields.[*]

2.1 Introduction

The study of growth rates of crystals from their melt, or from supersaturated solutions, besides being an interesting theoretical problem, is of importance for the prediction of macroscopic growth morphologies of crystals. The rheological properties of particulate systems, be it liquids in which small crystallites are suspended or just granular materials consisting of small crystallites, very much depend on the morphologies of the crystallites.

Since the crystal-melt interface, being a combination of two dense phases, is not easily accessible to experimental measurements, molecular dynamics simulations can be of great help in the study of these systems. Several studies of the crystal-melt interface of Lennard-Jones systems, consisting of atoms which interact by pairwise potentials of the form

$$\Phi_{\mathrm{LJ}}(r) = 4\varepsilon \left\{ \left(\frac{\sigma}{r}\right)^{12} - \left(\frac{\sigma}{r}\right)^{6} \right\}, \tag{2.1}$$

have been reported in the literature, mainly by Broughton, Gilmer *et al.* [28–32]. Among other things, they performed nonequilibrium molecular dynamics simulations to calculate the growth rates of various crystal faces over a wide range of temperatures below the melting point. In this chapter, we present a method to calculate growth rates from fluctuations of the interface during an equilibrium simulation. We have applied this method to study the growth

[*] The work described in this chapter previously appeared in Phys. Rev. Lett. **79**(25), 5074 (1997). [25]

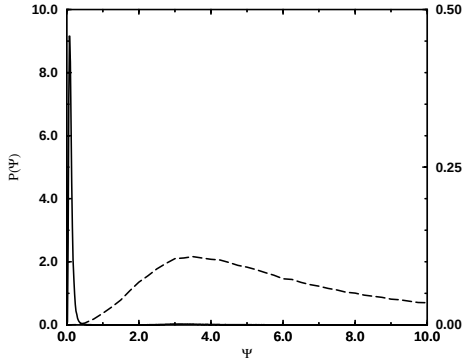

Figure 2.1: Distribution of the recognition function Ψ in bulk solid (solid line, left scale) and in bulk liquid (dashed line, right scale).

rate of the (100) face of a Lennard-Jones crystal growing from its melt, and checked the results by performing nonequilibrium simulations for very small deviations from equilibrium.

2.2 Solid-liquid recognition

In order to be able to decide whether a particle belongs to the crystal or to the melt, we have constructed a very simple recognition function. What distinguishes a particle in an FCC crystal from a particle in the liquid, is the fact that its surroundings have octahedral symmetry. We therefore have constructed, using the methods of Ref. [23], a function $X(\mathbf{r})$, which for every vector $\mathbf{r}$ pointing from the particle under investigation to one of its nearest neighbours, in a perfect crystal, takes the same value. When the fourfold symmetry axes of the octahedron are chosen along the three Cartesian axes, the simplest such function reads

$$X(\mathbf{r}) = \frac{x^4}{|\mathbf{r}|^4} + \frac{y^4}{|\mathbf{r}|^4} + \frac{z^4}{|\mathbf{r}|^4} - \frac{3}{5}. \tag{2.2}$$

The order parameter Ψ, which discriminates between crystal and liquid particles was next defined by

$$\Psi = \sqrt{\frac{\langle X^2 \rangle - \langle X \rangle^2}{\langle X \rangle^2}}, \tag{2.3}$$

where the averages were taken over all nearest neighbours residing within a cut-off radius of $1.39\,\sigma$. A slight amelioration was obtained by referring the positions of the neighbours, not to the central particle, but to the center of mass of the neighbours. The distributions of the values of Ψ during a simulation of a pure crystal and a simulation of a pure liquid are plotted in Fig. 2.1. It is seen that by calling crystal particles those particles for which $\Psi < 0.5$ and liquid particles those for which $\Psi > 0.5$, a perfect discriminator is defined. It is important to realize that crystalline structure will partly persist in the liquid phase near the interface. As a result our discriminator could slightly overestimate the number of solid particles. On the

other hand, crystalline particles in the interface that 'see' a crystal on one side and a liquid on the other, will not be classified as solid-like. This effect could lead to an underestimation of the number of solid particles. Overall, we expect that changes in the number of solid particles with respect to the average value will be correctly monitored.

2.3 Equilibrium simulations

In the case of simple monoatomic systems the melting temperature is found to be above the roughening transition (see also Sec. 1.3). Growth occurs at any point on the surface, and the growth mode is called normal growth [16, 35, 124]. In the case of small deviations from equilibrium, the growth rate of such a surface is proportional to the difference of the chemical potentials of the liquid and the solid phases, i.e.,

$$R = k\, d\, \frac{\mu_l - \mu_s}{k_B T}, \tag{2.4}$$

where d is the interplanar distance parallel to the interface. The growth rate is related to the increase of the number of solid particles dN_s/dt by

$$R = \frac{d}{A/a}\frac{dN_s}{dt}, \tag{2.5}$$

with a the specific area taken by a solid particle, and A the total area of the surface.

When the system is in equilibrium, no net growth takes place, and on average R equals zero. Instantaneous fluctuations of the number of solid particles do occur, however, and their dynamics is related to the above equations by means of Onsager's hypothesis. This hypothesis states [24, 36] that "slow equilibrium fluctuations on average decay according to macroscopic laws". We now first derive the macroscopic laws governing the relaxation of a small deviation $\Delta N_s = N_s - N_s^{\mathrm{eq}}$ of the number of solid particles from its equilibium value N_s^{eq}, in a closed system with constant volume and constant temperature. First we relate the difference between the chemical potentials occurring in Eq. 2.4 to the deviations from equilibrium of the molar volumes of both phases:

$$\mu_l - \mu_s = -\frac{1}{\kappa_l}\Delta v_l + \frac{1}{\kappa_s}\Delta v_s, \tag{2.6}$$

where κ is the isothermal compressibility. In order to calculate Δv_l and Δv_s we use the following relations

$$(N_l^{\mathrm{eq}} - \Delta N_s)(v_l^{\mathrm{eq}} + \Delta v_l) + (N_s^{\mathrm{eq}} + \Delta N_s)(v_s^{\mathrm{eq}} + \Delta v_s) = V, \tag{2.7}$$

$$\frac{\Delta v_l}{v_l^{\mathrm{eq}}\kappa_l} = -\Delta P = \frac{\Delta v_s}{v_s^{\mathrm{eq}}\kappa_s}, \tag{2.8}$$

where $N_l^{\mathrm{eq}} = N - N_s^{\mathrm{eq}}$. The second of these equations expresses uniformity of pressure during the simulations. This means that we assume that pressure gradients relax much faster than

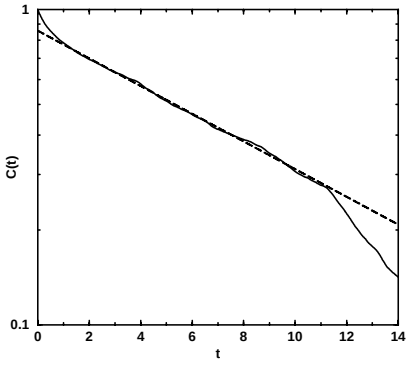

Figure 2.2: Normalized time-dependent autocorrelation function of ΔN_s. Timescale in units of $(m\sigma^2/\varepsilon)^{1/2}$.

the timescales we are interested in. Solving Eqs. 2.7 and 2.8 for Δv_l and Δv_s to first order in ΔN_s, and using the result in Eqs. 2.4 – 2.6, we obtain

$$\frac{d\Delta N_s}{dt} = -\frac{1}{\tau}\Delta N_s, \tag{2.9}$$

$$\frac{1}{\tau} = k\frac{A/a}{N}\left\{\frac{\left(v_l^{\rm eq}-v_s^{\rm eq}\right)^2}{v_s^{\rm eq}\kappa_s f_s^{\rm eq}+v_l^{\rm eq}\kappa_l f_l^{\rm eq}}\right\}\frac{1}{k_{\rm B}T}, \tag{2.10}$$

where $f_l^{\rm eq} = N_l^{\rm eq}/N$ and $f_s^{\rm eq} = N_s^{\rm eq}/N$. Eq. 2.9 says that ΔN_s decays from its initial value according to a simple exponential law.

We are now in the position to make use of Onsager's hypothesis in the form $\langle \Delta N_s(t)\rangle_{\Delta N_s(0)}$ $= \Delta N_s(0)\exp\{t/\tau\}$, from which we find

$$C(t) = \frac{\langle \Delta N_s(t)\Delta N_s(0)\rangle}{\langle \Delta N_s(0)^2\rangle} = \exp\left\{-\frac{t}{\tau}\right\}. \tag{2.11}$$

All simulations were done with the GROMOS87 package [19]. First, separate NPT simulations with $P = 2.546\times10^{-3}\,\varepsilon/\sigma^3$ and $T = 0.646\,\varepsilon/k_{\rm B}$ were carried out for a crystal and a liquid. The rates with which velocities and box volume were rescaled [18], were controlled by the relaxation times $\tau_T = 0.0747\ (m\sigma^2/\varepsilon)^{1/2}$ and $\tau_P/\kappa = 222.6\ (m\varepsilon)^{1/2}/\sigma^2$, with m the particle's mass. The timestep of the numerical integration of Newton's equations was $\Delta t = 0.0015\ (m\sigma^2/\varepsilon)^{1/2}$. The temperature was close enough to the equilibrium temperature for no structural changes to occur during neither of the two simulations. Next, the crystal box was surrounded by two liquid boxes along the y-axis. Subsequent simulations were done in the NVT ensemble with $T = 0.646\,\varepsilon/k_{\rm B}$; the number of particles was 1378, and the box dimensions were $L_x = L_z = 8.069\,\sigma$ and $L_y = 24.206\,\sigma$. Note that two interfaces occur in the box and that A in Eqs. 2.5 and 2.10 denotes the total surface area.

Correlation function $C(t)$ from Eq. 2.11 is plotted in Fig. 2.2. After a short transient time of about $1.5\ (m\sigma^2/\varepsilon)^{1/2}$, this correlation function decays exponentially with time constant $\tau = 9.887\ (m\sigma^2/\varepsilon)^{1/2}$, which amounts to $k = 0.5269\ (m\sigma^2/\varepsilon)^{-1/2}$. The value of

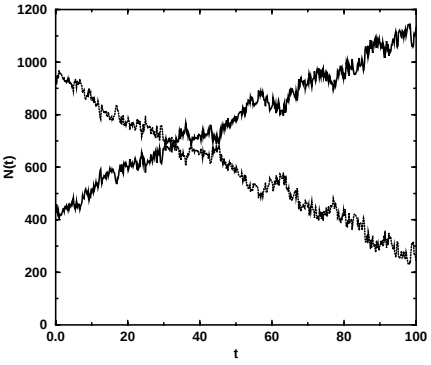

Figure 2.3: Characteristics of a growing crystal. The ascending line denotes the number of solid particles and the descending line the number of liquid particles. Timescale in reduced units. $T = 0.612\,\varepsilon/k_B$.

k was calculated from Eq. 2.10, using $d = 0.8113\ \sigma$, $v_s^{eq} = 1.0564\ \sigma^3$, $v_l^{eq} = 1.200\ \sigma^3$, $\kappa_s = 0.00428\ \sigma^3/\varepsilon$, $\kappa_l = 0.01412\ \sigma^3/\varepsilon$, $N_s^{eq} = 540.7$, and $N_l^{eq} = 837.3$. v_s^{eq}, v_l^{eq}, and d were measured from the bulk parts of the respective phases in the equilibrium simulation; κ_l was calculated using the equation of state given by Nicolas *et al.* [136]; κ_s was calculated according to $\kappa_s/\kappa_l = \Delta v_s/\Delta v_l \times v_l/v_s$ with v_s and v_l the specific volumes of the initial solid and liquid boxes, and $\Delta v_s = v_s^{eq} - v_s$ and $\Delta v_l = v_l^{eq} - v_l$; N_s^{eq} and N_l^{eq} were calculated from $N_s^{eq} v_s^{eq} + N_l^{eq} v_l^{eq} = V$ and $N_s^{eq} + N_l^{eq} = N$.

It is seen that for times larger than about 11 $(m\sigma^2/\varepsilon)^{1/2}$, large deviations from exponential decay occur. These deviations possibly reflect the influence of long-time temperature oscillations, caused by insufficient removal and supply of latent heat of crystallization and melting, respectively. They can further be due to insufficient statistical sampling of the longer correlation times (in *Chapter 5* we will review the method in much more statistical detail).

2.4 Nonequilibrium simulations

In order to check our results, we have done nonequilibrium simulations in the NPT ensemble with $P = 2.546 \times 10^{-3}\ \varepsilon/\sigma^3$ at various temperatures around the equilibrium temperature. An example of the evolution of $N_s(t)$ with time during such a simulation is given in Fig. 2.3. The fact that N_s is a linear function of time means that we have well succeeded in keeping constant the nonequilibrium conditions. Applying parameters for argon, the growth rate amounts to 14 m/s in good agreement with the results of Burke and Broughton.

For small deviations from equilibrium we may write

$$R = -\,k\,d\,\frac{h_l^{eq} - h_s^{eq}}{k_B T^{eq}}\,\frac{\Delta T}{T^{eq}}, \tag{2.12}$$

i.e., the growth rate is proportional to $\Delta T = T - T^{eq}$. In Fig. 2.4, the growth rates obtained for various temperatures are collected. The straight line is obtained from Eq. 2.12 using k from the equilibrium simulation and $h_l^{eq} - h_s^{eq} = 1.01\ \varepsilon$. h_l^{eq} and h_s^{eq} were obtained from short NVT simulations at the respective equilibrium densities and $T = 0.646\ \varepsilon/k_B$. It is seen that

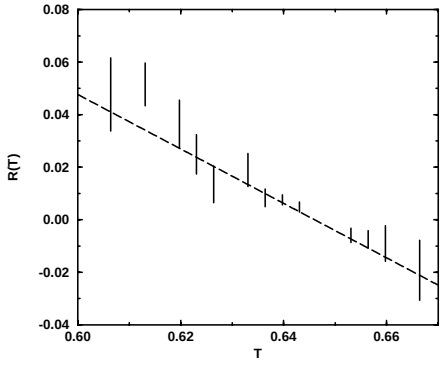

Figure 2.4: Nonequilibrium results of the growth rate vs. temperature (both in reduced units). The straight line represents growth rates calculated with the growth rate constant k obtained with the equilibrium simulation.

this line very well represents the data, and that therefore the equilibrium and nonequilibrium simulations are in good agreement with each other.

2.5 Discussion

The error bars in Fig. 2.4 roughly indicate the maximum and minimum values of the corresponding growth rates. For large values of $|\Delta T|$ the system rapidly melts or crystallizes. As a result the runs are very short and the difference between maximum and minimum slopes are relatively large. One way to obtain better statistics is to repeat the same simulation several times. A second way might be to use much larger boxes. This however is not an easy task because with such large growth or melting rates it will become increasingly difficult to maintain constant nonequilibrium conditions. As a consequence the nonequilibrium method which asks for many simulations for many different values of ΔT is much more costly than one equilibrium simulation. We will come back to these remarks in *Chapters 4 and 5*.

One disadvantage of the equilibrium method is that the (finite size) equilibrium temperature must be known fairly accurately, in order for the pressure not to change too much during the initial part of the NVT run. As a final remark we notice that the relaxation time which is actually measured, i.e., the relaxation time τ, is proportional to N/A, i.e., to the box size normal to the interface. This size must therefore not take part in the thermodynamic limit.

3 The crucial role of lattice imperfections

In this chapter, we present nonequilibrium simulations of growth and melting of the atomic FCC *(100) interface. Using Nosé-Hoover dynamics we have carefully studied size effects and approximated the dynamics of the solid-liquid interface in a large system as closely as possible. This led to a clear asymmetry of growth and melting rates close to equilibrium. It was possible to explain these findings in terms of the lattice imperfections in crystalline phases in contact with a liquid phase, which automatically developed during growth simulations but were absent in the melting simulations. It was shown that when melting simulations were started with appropriate starting configurations, the asymmetry could be made to disappear.*[*]

3.1 Introduction

Although much is known about the thermodynamics of the solid-liquid phase transition, the kinetics of this transition is still poorly understood. Part of this is due to the fact that, being a combination of two dense phases, the crystal-melt interface is not easily accessible to experiment. Therefore, computer simulations can be of great help in understanding the microscopic processes involved in crystallization or melting. Over the past few years, excellent reviews have appeared on computer modelling and on theories of the structure and dynamics of the crystal-liquid interface [95, 118, 121].

Most crystallization and melting processes are heterogeneous, i.e., they involve the motion of an interface throughout the system. Among the first to make an extensive study of this process, were Broughton *et al.* [28–30, 32]. They combined the solid and the liquid phase in one simulation box and calculated growth rates over a wide range of temperatures. They, however, did not study melting.

In *Chapter 2* [25], we studied the steady state velocity of the interface in a Lennard-Jones system at small undercoolings and superheatings. We established growth and melting rates as a function of the deviation from equilibrium by performing several nonequilibrium

[*] The work described in this chapter previously appeared in J. Cryst. Growth. **230**(1-2), 270 (2001). [169]

simulations. On the basis of Onsager's regression hypothesis, we were able to obtain the same information from fluctuations of the amount of crystalline material during one single equilibrium simulation. The same (universal) procedure was later succesfully applied to the calculation of transport diffusion of guest molecules in a zeolite (see *Chapter 8* [86]).

Over the past fifteen years much debate has evolved on the question whether the interface response should be symmetric around the equilibrium temperature. An argument on the basis of microscopic reversibility, already presented in the sixties [180], concluded that if molecules are added to or taken from similar interface sites, then the curves of crystallization rate and melting rate versus temperature should be continuous with the same slope through the melting temperature. The debate was initiated again, however, by Tsao *et al.* [176] who reported experiments of laser-induced zone melting of silicon, in which growth of the melt into the superheated solid appeared to be much faster than growth of the crystal into the undercooled liquid. Since they dealt with large deviations from equilibrium, no sharp conclusion can be drawn about a possible slope discontinuity at equilibrium.

Kluge and Ray [111] performed molecular dynamics simulations of crystallization and melting of silicon. They employed a Stillinger-Weber potential and considered large deviations from equilibrium. Their results show the same trends as the experiments by Tsao. Tymczak and Ray [178] did similar simulations on sodium crystals having BCC symmetry. They found a clear slope discontinuity at equilibrium with melting being substantially faster than crystallization. However, since they mimic the electron density dependence of the interactions by changing the potential with temperature, it is impossible also in this case to draw any conclusions about the occurrence of an asymmetry between growth and melting rate in systems interacting via Lennard-Jones potentials.

The only careful investigation at small undercoolings and superheatings was presented by Moss and Harrowell [133]. They performed dynamic Monte Carlo simulations of the FCC lattice gas and studied freezing and melting of the simple cubic phase. Besides a clear slope discontinuity, they also found a small range of supercoolings where the growth velocity essentially vanished.

From all of the above, no clear picture arises of the possibility or impossibility of a slope discontinuity in the interface response near equilibrium. In this chapter, we will present detailed measurements of the growth and melting rates in an atomistic simulation and will address some of the subtleties that arise in doing such simulations. We will show that a slope discontinuity arises when starting growth and melting simulations from well equilibrated liquid and solid phases. The discontinuity will be seen to disappear only when lattice imperfections occurring in rapidly growing crystals are also taken into account in the melting simulations.

3.2 Interaction model

To avoid possible complications with long-range attractions (which would lead to different long-range corrections in bulk and two-phase systems), we required a pair potential which is exactly zero beyond a certain cut-off radius. To this end, we employed the shifted force 12-6 potential as introduced by Clarke *et al.* [39] (where it has the general form of an $n-m$

potential). The potential has the following structure:

$$U(r_{ij}) = \alpha\varepsilon\left[\beta^{12}\left\{\left(\frac{r_0}{r_{ij}}\right)^{12}-\left(\frac{1}{\gamma}\right)^{12}\right\}-2\beta^6\left\{\left(\frac{r_0}{r_{ij}}\right)^{6}-\left(\frac{1}{\gamma}\right)^{6}\right\}\right] + 12\alpha\varepsilon\left(\frac{r_{ij}-\gamma r_0}{\gamma r_0}\right)\left\{\left(\frac{\beta}{\gamma}\right)^{12}-\left(\frac{\beta}{\gamma}\right)^{6}\right\} \tag{3.1}$$

with

$$\gamma = \frac{r_{\rm cut}}{r_0}, \tag{3.2}$$

$$\beta = \gamma\left(\frac{\gamma^7-1}{\gamma^{13}-1}\right)^{\frac{1}{6}}, \tag{3.3}$$

and

$$\alpha = \frac{1}{2\beta^6(1+\frac{6-7\gamma}{\gamma^7})-\beta^{12}(1+\frac{12-13\gamma}{\gamma^{13}})} \tag{3.4}$$

This form has the advantage over the standard shifted force potentials that both ε and r_0 (the well depth and the location of the minimum) retain their original meaning after the shifting process. In our simulations we will take the common value $r_{\rm cut} = 2.5\sigma$ where σ is implicitly defined by $r_0 = 2^{1/6}\sigma$. All properties will be presented in terms of ε, σ, and the mass m (common Lennard-Jones units).

3.3 Simulation method

We performed molecular dynamics simulations at constant number of particles (N), constant pressure (P), and constant temperature (T). In order to simulate a true isothermal-isobaric ensemble, we used Nosé-Hoover dynamics [87, 139] to integrate the equations of motion, in which the thermostat and barostat variables are taking part in the dynamics of the system. We did a careful study of pressure and temperature distributions in a bulk liquid and bulk solid in order to tune the thermostat and barostat relaxation times so as to ensure that the distributions had the correct width within reasonable simulation time and that the pressure and temperature fluctuations did not interact. This resulted in $\tau_T = 0.0748\,\sigma\sqrt{m/\varepsilon}$ and $\tau_P = 0.748\,\sigma\sqrt{m/\varepsilon}$, with a timestep of $\Delta t = 0.000748\,\sigma\sqrt{m/\varepsilon}$.

In order to derive the correct temperature dependence of the bulk densities, we performed NPT simulations on bulk systems of liquid (512 particles) and FCC solid (500 particles) at various temperatures and pressure $P = 0.0025\,\varepsilon/\sigma^3$. Average volumes were calculated over 200,000 timesteps. The volumes per atom were least-squares fitted to a straight function in T resulting in

$$v_l^* = 0.76111 + 0.77153 \times T^*, \qquad 0.580 < T^* < 0.630, \tag{3.5}$$

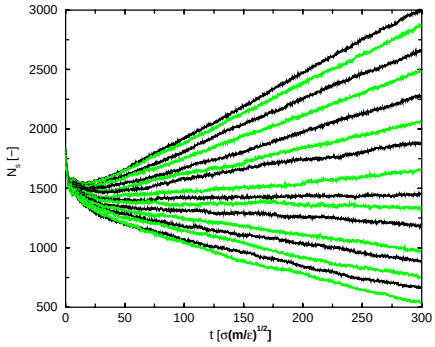

Figure 3.1: Growth and melting curves from nonequilibrium simulations showing the number of solid-like particles vs. time. Results are shown for a range of temperatures varying from $0.580\ \sigma\sqrt{m/\varepsilon}$ (upmost curve) to $0.630\ \sigma\sqrt{m/\varepsilon}$ (lowest curve).

and

$$v_s^* = 0.85370 + 0.35466 \times T^*, \qquad 0.580 < T^* < 0.630. \tag{3.6}$$

With the fitted volumes, new bulk simulations were performed at constant volume. The solid and liquid boxes were made such that they had equal cross-sections in the x,y-plane. The bulk NVT simulation were run for 100,000 timesteps of equilibration, whereafter coordinate files were written every 1000 timesteps. To make two-phase boxes, one liquid and one solid configuration were taken, both copied 4 times in the z-direction, and subsequently put on top of each other. This way, two interfaces appear in the boxes, with their surfaces along the x- and y-axes. The resulting boxes consisted of 2000 initially crystalline particles ($5 \times 5 \times 20$ unit cells) and 2048 particles initially belonging to the liquid phase. To release excessive potential energies due to particle overlap, 300 timesteps of NVT simulation were done with rigid temperature scaling at every timestep. After this, NPT runs were carried out to study growth and melting rates. The pressure scaling routine was adopted such that the volume relaxation in x-, y-, and z-directions took place independently.

3.4 Results

In order to calculate growth and melting rates, we used an order parameter to distinguish the crystal phase from the liquid phase. The order parameter, which was introduced in *Chapter 2* [25], takes advantage of the octahedral symmetry of the nearest neighbours around a particle in an FCC crystal. As can be seen in that chapter, a function Ψ could be derived which discriminates very well between 'solid-like' and 'liquid-like' particles. The advantage of the order parameter is that it is defined for each atom, so keeping track of the growth of one phase comes down to merely counting the number of particles belonging to the crystal.

Results of growth and melting simulations are presented in Fig. 3.1. Each curve stands for the average of 50 simulations at a given temperature. Because of the substantial temperature fluctuations in the isothermal-isobaric ensemble, a spreading naturally arises in the results from different runs at the same temperature. Therefore several runs with different

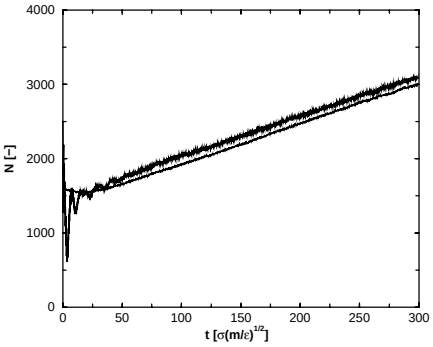

Figure 3.2: Comparison of growth curves derived via the two methods of calculating the number of solid-like particles: via the order parameter (lower curve) and via the volume measurement (upper, more fluctuating curve).

initial configurations (combinations of different configurations from the solid as well as from the liquid runs) had to be carried out to obtain good statistical accuracy. As can be seen from the figure, the overall behaviour is universal; after an equilibration period of less than 50 reduced time units, the number of crystalline particles increases or decreases linearly in time. This means that the supersaturation was kept constant and the two interfaces were separated far enough so as to not interact with one another.

Note that our system size is substantially larger (a factor 2.5) than the one used by Broughton *et al.* [30]. Their claim that their interfaces did not interact was underpinned by checking only static bulk properties and no dynamic properties. We found that with a system of half the present size, the region before the constant linear regime really sets in is almost twice as long, making it much harder to measure the growth rates accurately.

An alternative way of measuring growth rates is by monitoring the volume evolution of the system in time. The number of crystal particles at time t can then by estimated by

$$N_s(t) = \frac{N_{\text{total}} \times v_l - V_{\text{total}}(t)}{v_l - v_s} \tag{3.7}$$

The results of both methods for $T = 0.580\ \varepsilon/k_{\text{B}}$ are similar, which is demonstrated in Fig. 3.2. This implies that the density front in the simulation is moving at the same speed as the order front. This holds true for all temperatures we investigated.

From the linear part of the growth curves, growth rates were calculated and plotted versus temperature in Fig. 3.3 (filled circles). As can be seen from the figure, this procedure led to an apparent asymmetry of the growth and melting rates in the vicinity of the equilibrium point. We checked that this asymmetry was independent of the vertical box size by performing simulations of boxes of half the size. Moreover, since volume measurements and order parameter measurements gave the same results, we concluded that the asymmetry was not an artefact of the measurement method.

There was one feature of the method which was inherently asymmetric and therefore might be the cause of the asymmetry. That is, the crystals emerging from the growth simulations had incorporated certain imperfections which were not present in the bulk crystals. When looking at Fig. 3.4, where only the disordered ('liquid-like') particles have been drawn,

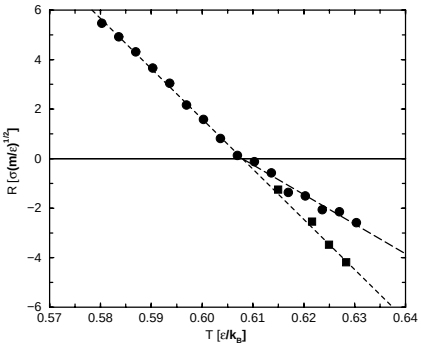

Figure 3.3: Temperature dependence of growth and melting rates. A clear asymmetry is seen between growth and melting rates from the first method (filled circles). Rates from melt simulations where lattice imperfections were taken into account are shown as filled squares.

one sees that the crystal at the end of a growth simulation (denoted with NPT) contains imperfections. An example of a starting configuration of a two-phase run (containing an equilibrated solid in the middle) is shown in the first snapshot of Fig. 3.4, which indeed shows no liquid-like particles in the crystalline phase. Unlike the discussion of imperfections by others like Burke *et al.* [32] and Huitema *et al.* [89], almost all of these imperfections were neither interstitial atoms, nor vacancies. Virtually all layers contained the maximum amount of particles, i.e., 50 (which was easily checked by integrating the longitudinal density profile layer by layer), but on average one particle per layer was located away from its lattice site. Burke *et al.* reported a substantial increase of the vacancy concentration upon decreasing temperature. Unfortunately, they did not explain the way they measured the vacancy concentration. Again, it should be noted that they investigated much larger undercoolings than we did. Huitema *et al.* reported on undercoolings comparable to ours, but their results suffer from poor statistics and they as well do not explain their way of quantification of the number of vacancies.

Since it is now clear that the crystals grown below equilibrium are structurally different from the crystals with which we started our melting simulations, the asymmetry might be explained by this difference. In order to check this we took the 50 end configurations of growth runs at a certain temperature and started new simulations therewith at temperatures at the same amount of superheating as the amount of undercooling at which they were produced. In other words, the systems were put on the mirror side of the equilibrium temperature (which was estimated from Fig. 3.3 to be $0.608\,\sigma\sqrt{m/\varepsilon}$). The result of one such experiment is shown in Fig. 3.5. As a guide, the mirror image of the original growth curve is plotted above the new melting curve. The slopes of both lines are in agreement. For comparison, two melting curves starting with ideal crystals at temperatures just below and just above the present temperature are also displayed. Clearly, the old method gives much smaller melting rates. The experiment was repeated for four different temperatures and displayed as squares in Fig. 3.3. The asymmetry of the interface reponse has now completely disappeared. This phenomenon has been completely attributed to the subtlety of preparing initial configurations. The much smaller melting rates from the totally ordered crystal might be the reason why Burke *et al.* [32] failed to produce steady state melting. Instead their overheating was that

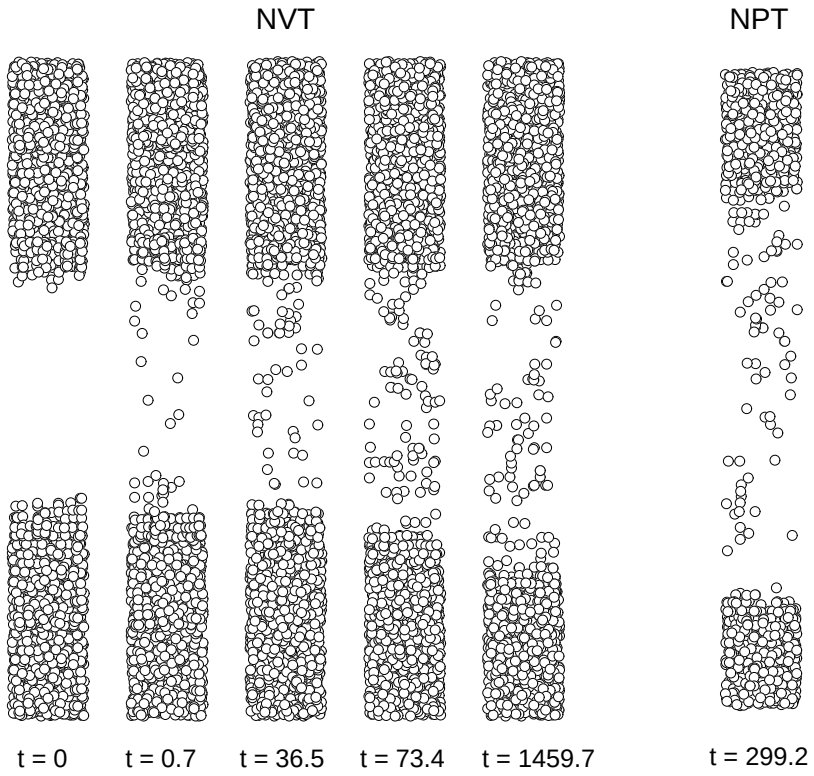

Figure 3.4: Snapshots of different stages in an equilibrium run (*NVT*) and of an end configuration of a nonequilibrium run (*NPT*) at $T = 0.587\ \varepsilon/k_{\mathrm{B}}$. Only the particles classified as 'liquid-like' are shown, providing a clear representation of the amount of mismatch in the crystalline lattice.

large that they reached the mechanical melting point, i.e., the point at which the whole crystal disintegrates at once.

It is important to note that not the constant pressure situation (which allows the crystal to relax its volume), but either the presence of an interface or the rapid incorporation of defects during growth causes the slightly disordered structure. In *Chapter 2* [25], we showed that the kinetic growth coefficient obtained from nonequilibrium simulations can also be obtained from the fluctuations of the number of crystalline atoms in an equilibrium simulation. In the light of the above, we investigated if the crystalline phase in such an equilibrium simulation contains an equal number of imperfections as seen in the nonequilibrium simulation. Snapshots of different stages in an extensive equilibrium simulation are shown in Fig. 3.4. Indeed, the number of imperfections is comparable. Note that the imperfections extend throughout the whole crystal, and not just in the regions where the crystal has melted and regrown during

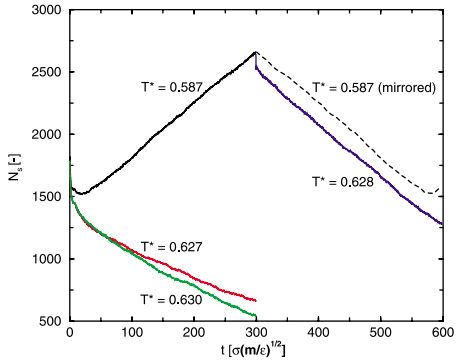

Figure 3.5: Growth and melting curves showing the difference between starting from configurations with and without lattice imperfections in the crystalline phase.

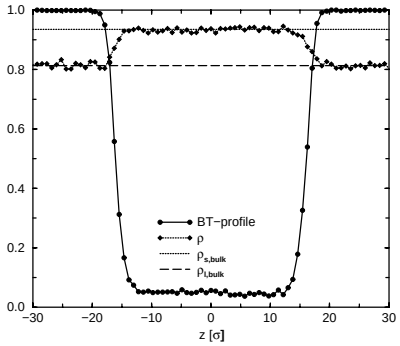

Figure 3.6: Laterally integrated density and order profile in an equilibrium simulation.

fluctuations. This means that it is the proximity of the liquid phase that causes the slight disorder in the crystal and not just the rapid incorporation of defects.

A more quantitative measure of the disorder is provided in Fig. 3.6. There we have calculated the BT-profile, as introduced by Jesson and Madden [97], which is the laterally integrated average number density of liquid material. Were the crystal totally ordered, the value would have dropped to zero. For comparison, also the laterally averaged density profile is shown. It can be seen that the densities in the liquid and in the solid agree perfectly with the bulk values obtained from the bulk simulations. This shows again that it is not enough to just look at static bulk properties in order to decide whether equilibrium is reached. In *Chapter 5*, we will undertake research to extract the kinetic growth coefficient from the equilibrium simulation in the spirit of *Chapter 2*.

3.5 Conclusions

In this chapter, we have investigated the response of the FCC (100) crystal-liquid interface to small superheatings and undercoolings with respect to the equilibrium melting temperature. This led to an asymmetry of the response, which was explained in terms of lattice imperfections in the crystalline phase. Such imperfections naturally evolved in the growing crystal in contact with a liquid phase, but were absent in the equilibrated bulk crystal and thus also in the melting simulations. When the melting simulations were started from configurations produced during growth of the two-phase systems (thus including imperfections in the crystalline lattice), the asymmetry between growth and melting rates around equilibrium completely disappeared.

Equilibrium simulations of a two-phase system were shown to produce lattice imperfec-

tions equivalent to the ones emerging in growth simulations. This implies that equilibrium simulations as advocated in *Chapter 2* [25] may provide an alternative for calculating the interface response near equilibrium in a more straightforward way.

4 Equilibration, relaxation, and long-time dynamics of the moving interface

In this chapter, we present nonequilibrium molecular dynamics simulations on the growth and melting of the Lennard-Jones (100) interface at small undercoolings and superheatings. Production runs were carried out after extensive equilibration at the melting point. Two regimes of linear growth rate were discovered: a short-time regime associated with interface relaxation and a long-time regime associated with the macroscopic limit of growth and melting. It was shown that, if system sizes or equilibration times are taken too small, one will find only the initial regime. On the basis of our very accurate results on the macroscopic growth rates close to equilibrium, the possibility of a discontinuity in the temperature dependence of growth and melting rates at the melting point was ruled out. [*]

4.1 Introduction

Understanding the microscopic processes associated with crystal growth from the melt is of major importance in the prediction of the growth rates of various crystal planes, and, eventually, the growth morphology of the crystal as a whole. Except for very large deviations from the melting temperature, where homogeneous nucleation may dominate the dynamics, the process of melting and freezing of a crystal takes place at the interface. Since this interface, being a combination of two dense phases, is not easily accessible to experiment, computer simulations provide a good means to elucidate the microscopic restructuring processes involved in crystallization and melting. In this study, we will use Molecular Dynamics (MD) simulations to look at the growth and melting of the Lennard-Jones (100) interface at small amounts of undercooling and superheating. In this regime, the interface is thermodynamically rough and defect growth does not play a significant role.

One of the first accounts of the steady-state motion of a crystal-melt interface in MD simulations has been the work of Broughton, Gilmer, and Jackson [28]. They combined a solid and a liquid phase in one simulation box and calculated the steady-state velocity of

[*] The work described in this chapter has been accepted for publication in J. Chem. Phys. [170]

the interface as a function of temperature. A theoretical prediction for this dependence is supplied by the Jackson-Chalmers representation of the Wilson-Frenkel theory [92] (see also Sec. 1.2), where the solid-liquid transition is assumed to take place through some intermediate or transition state. The rates R are given by:

$$R(T) = C_1 \exp\left(-\frac{Q}{k_B T}\right)\left[1 - \exp\left(\frac{(h_l - h_s)(T - T_m)}{k_B T \times T_m}\right)\right], \tag{4.1}$$

where Q is the activation energy for diffusion in the liquid, and h is the enthalpy per particle of the respective phase. Broughton *et al.* showed that for the Lennard-Jones FCC (100) surface, the incorporation of atoms on the surface of the crystal is not an activated process. This led them to replace the Arrhenius factor by a factor proportional to the thermal velocity of the atoms:

$$R(T) = C_2 T^{1/2}\left[1 - \exp\left(\frac{(h_l - h_s)(T - T_m)}{k_B T \times T_m}\right)\right], \tag{4.2}$$

which was shown to reproduce their data over a wide range of temperatures (albeit all below T_m). Both Eqs. 4.1 and 4.2 lead to the general observation that melting rates are larger than crystallization rates, at equal amounts of supersaturation. This might be one of the reasons that over the past decades a large number of simulation studies have appeared on the freezing of crystals, but comparatively few on melting. For instance, in a successive paper of the Broughton group [32], they tried to complement their growth studies with melting, but they failed to produce steady state melting. Instead they quickly reached the mechanical melting point, i.e., the point at which the whole crystal disintegrates at once. Note that the undercoolings and superheatings they used are enormous compared to the ones we will look at.

The asymmetry of freezing and melting kinetics was first shown experimentally for crystalline silicon (c-Si) growing from amorphous silicon (a-Si) by Tsao *et al.* [176]. Their results were later reproduced with MD simulations by Kluge and Ray [111], using a Stillinger-Weber potential, and by Iwamatsu and Horii [91] with classical Density Functional Theory (DFT). Note that, although they all report an asymmetry between melting and freezing in these systems, there is no slope discontinuity of the growth rate vs. temperature curve upon crossing the melting point. It was mentioned already in the 1920's, in an Ansatz by Tammann [165], that such a slope discontinuity can not occur. This was restated in the 1960's by Uhlmann *et al.* [180], who argued that an abrupt change in the kinetic coefficient (C_2 in Eq. 4.2) on going from freezing to melting would imply a violation of microscopic reversibility.

However, in their study of crystallization and melting of sodium, Tymczak and Ray [177, 178] found a clear slope discontinuity at the equilibrium temperature. Singularities at the melting point were subsequently reported with dynamic DFT calculations [157], a kinetic mean field theory [189], and lattice gas simulations [133]. The theory of Richards [145] tried to explain the asymmetry on the basis of the density change upon freezing or melting, but the major role of this density change was later contradicted by the work of Oxtoby and Harrowell [140]. Up till now, the question is still under debate.

In *Chapter 3* [169], we reported on nonequilibrium simulations for the FCC (100) interface with the Clarke [39] potential. There, we investigated the influence of system size

effects and carried out thorough thermodynamic averaging to arrive at very accurate statistics. This initially led to a clear asymmetry of growth and melting rates close to equilibrium, which was attributed to lattice imperfections in the growing crystals. It was shown that if the melting simulations were started with the initially grown crystals, the asymmetry was made to disappear, thus showing it to be an artefact of the simulations. A comparable asymmetry was found in the growth and melting simulations of Huitema *et al.* [89], but since they were mainly interested in crystallization rates, they did not discuss it.

In *Chapter 2* [25], we presented a method to extract the temperature dependence of the interface velocities from the fluctuations in an equilibrium simulation. Note that, for the applicability of this efficient method, it is crucial that no slope discontinuity exists at the equilibrium temperature.

In this chapter, we will carry out nonequilibrium simulations for a pure Lennard-Jones substance and extend our previous findings. We will demonstrate the crucial importance of good equilibration and we will report on the discovery of two time-regimes of growing and melting rates. The initial regime is associated with interface relaxation, while the second regime is associated with the macroscopic limit of growth. We will discuss the risk that when equilibration is not carried out to full extent, or when too small system sizes are used, only the initial regime will be observed, which can easily lead to erroneous conclusions about the temperature dependence of growth and melting rates. The procedures described here will be of general interest to the study of crystal-liquid interfaces in simple systems, both dynamically and in equilibrium, which continues to be the topic of many theoretical and simulation studies at present [82, 97, 122, 134].

This chapter is organized as follows. In the next section, we will describe our simulation system. First we mention how we tuned our thermostat and barostat to carry out the nonequilibrium simulations. Second, we describe the interparticle interactions and pay particular attention to how long-range corrections to the pressure should be carried out in simulations where two phases are present. In Sec. 4.3 we describe our equilibration method and show that proper equilibration is crucial to extract the correct rates. The succeeding section deals with the results of the nonequilibrium simulations and the discovery of the two regimes of linear growth rate. Finally, in Sec. 4.5, the temperature dependence of the rates will be presented and it will be shown that, for our system, a slope discontinuity does not exist at the melting point.

4.2 Simulation details

4.2.1 Nosé-Hoover dynamics

In this study, we simulated two-phase crystal-melt systems at constant number of particles (N), pressure (P), and temperature (T). In order to accomplish this, we employed Nosé-Hoover dynamics [87, 139]. This scheme is known to have a well-defined conserved quantity and to generate trajectories with the correct distribution of pressures and temperatures. Although thermodynamic properties like pressure and temperature are only rigorously defined as ensemble averages, we will use these terms also to refer to the instantaneous values of their

microscopic estimators:

$$\hat{T} = \frac{1}{N_f k_\mathrm{B}} \sum_{i=1}^{N} \frac{|\mathbf{p}_i|^2}{m_i} \tag{4.3}$$

and

$$\hat{P} = \rho k_\mathrm{B} \hat{T} + \frac{1}{3V} \sum_{i=1}^{N} \mathbf{r}_i \cdot \mathbf{f}_i, \tag{4.4}$$

with N_f the number of degrees of freedom.

In the Nosé-Hoover scheme both pressure and temperature are constrained to produce the desired distributions by coupling to a bath by means of parameters that rescale the volume and the particles velocities, respectively. The algorithm has been shown to be quite robust with respect to the speed at which momentum space and configuration space are rescaled [174, 175]. However, since we are dealing with systems that are not in thermodynamic equilibrium in this study, we do not only require that the scheme produces the correct distributions on average, but also within reasonable time. More specifically, in the case of a growth simulation, for example, we do not wish the system to have crystallized by a substantial amount before it has sampled a representative part of the temperature and pressure distributions. This additional requirement of fast thermostat and barostat equilibration makes the choice of both the timestep and the bath relaxation times much more delicate than in simulations at thermodynamic equilibrium.

In order to be on the safe side with respect to energy drifts (cf. Ref. [174], Table 2), we used a timestep of $7.480 \times 10^{-4} \sqrt{m\sigma^2/\varepsilon}$ (reduced Lennard-Jones units) in all our simulations. For tuning of the relaxation times, we studied the distributions of temperature and pressure in both a bulk liquid and a bulk solid of Lennard-Jones particles with a cut-off radius of $2.5\,\sigma$ and long-range corrections to the pressure and the energy. The distributions were calculated over short runs of 50,000 timesteps after equilibration. The temperature distributions were measured at constant NVT, and the pressure distributions at constant NPT (bulk liquid) or $N\bar{\bar{\sigma}}T$ (bulk solid). Here constant pressure tensor $\bar{\bar{\sigma}}$ means that both the box volume and shape were allowed to relax. Results are shown in Fig. 4.1. From this figure it can be seen that when a relaxation time is given too small a value, the corresponding property remains too close to the average value. Also, one can see that there is a steady 'overshoot', i.e., the values basically bounce back and forth between two values just below and above the average. From the time evolution (not shown here) it appeared that this process happens at one distinct frequency. On the other side of the spectrum, if relaxation times are chosen too large, the distribution does not have the correct width either, at least not within the 50,000 timesteps displayed here. In the end, the system will sample the whole distribution, but it does so by long-time fluctuations superimposed on the chaotic short-time oscillations (which again was seen from the time evolutions).

We also investigated the temperature distribution in the constant pressure simulations. They were nearly equal to the ones shown here (for NVT simulations), from which we conclude that for our choice of relaxation times, the thermostat and the barostat variables do not interact. For all the simulations in this study, we chose as thermostat relaxation time $\tau_T = 0.0748 \sqrt{m\sigma^2/\varepsilon}$ and as barostat relaxation time $\tau_P = 0.748 \sqrt{m\sigma^2/\varepsilon}$.

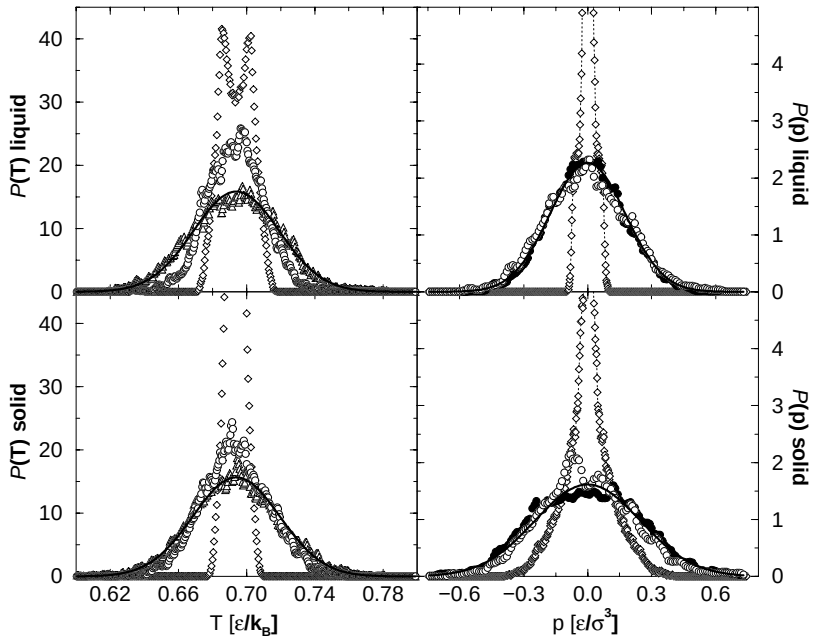

Figure 4.1: *Left side:* Normalized distributions (NVT) of the temperature estimator in a bulk liquid (512 atoms) and a bulk solid (500) atoms at $T = 0.694\ \varepsilon/\mathrm{k_B}$. Measurements are taken over 50,000 timesteps for $\tau_T = 0.00748\ \sqrt{m\sigma^2/\varepsilon}$ (diamonds), $\tau_T = 0.0748\ \sqrt{m\sigma^2/\varepsilon}$ (triangles), and $\tau_T = 0.748\ \sqrt{m\sigma^2/\varepsilon}$ (circles). The solid lines represent a Gaussian distribution with variance $2T^2/3(N-1)$. *Right side:* Normalized distributions (NPT) of the pressure estimator in a bulk liquid (512 atoms) and a bulk solid (500) atoms at $T = 0.694\ \varepsilon/\mathrm{k_B}$. Measurements are taken over 50,000 timesteps for $\tau_P = 0.0748\ \sqrt{m\sigma^2/\varepsilon}$ (diamonds), $\tau_P = 0.748\ \sqrt{m\sigma^2/\varepsilon}$ (triangles), and $\tau_P = 7.48\ \sqrt{m\sigma^2/\varepsilon}$ (circles). The solid lines represent fits to Gaussian distributions (variances $\sigma_P^{\mathrm{liquid}} = 0.031\ \varepsilon/\sigma^3$ and $\sigma_P^{\mathrm{solid}} = 0.061\ \varepsilon/\sigma^3$).

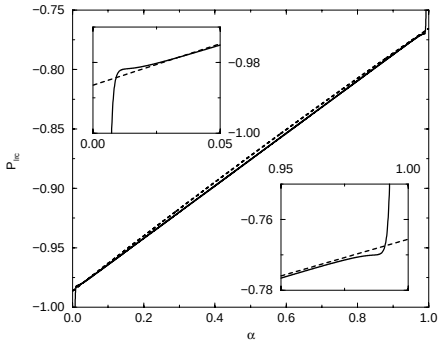

Figure 4.2: Long-range corrections to the pressure in a two-phase system as a function of the volume fraction α ($= V_l/V$). Shown are expressions 4.A.4 and 4.A.6.

4.2.2 The model system

In *Chapter 3*, we used the Clarke 12-6 potential [39] to model particle-particle interactions. This potential has the advantage that it goes smoothly to zero at a predescribed cut-off distance. However, since much more data exist both numerically and theoretically on the simpler Lennard-Jones potential, we chose the latter for the present study. All interparticle interactions were modelled with the standard Lennard-Jones 12-6 potential with a cut-off radius (r_c) of 2.5 σ. Accordingly, all properties in this chapter will be presented in terms of the well-depth ε, the radius σ and the mass m.

Because the potential is rigorously put to zero beyond the cut-off radius, the long-range tail of the (infinite) potential is missed, which must be corrected for in the energy and the pressure. Such corrections naturally depend on the density of the system. Since in constant pressure simulations the density changes during the run, the corrections must be made at run-time. This is usually done by assuming that the radial distribution function $g(r)$ is approximately equal to 1 for $r > r_c$ and then analytically integrating the interaction potential or the virial contribution (for energy and pressure, respectively) multiplied by the bulk density squared. In a system with two phases of different densities, however, there is no well-defined bulk density, which makes the procedure less straightforward. In the appendix of this chapter, an expression is derived for the long-range correction to the pressure in a system with two phases separated by a flat interface (see Eq. 4.A.4). The resulting values for different fractions by volume α of crystalline material are given in Fig. 4.2. As can be seen from the figure, there is surprisingly little difference between our improved expression and the correction made with the overall density.

It has recently been pointed out by Baidakov *et al.* [8] that in simulations where an interface is present, it can be extremely important to explicitly take into account enough of the long-range interactions. For example in their simulations of the Lennard-Jones liquid-vapour interface, they found extensive changes of thermodynamic properties, the surface tension and the thickness of the interface layer upon going from a small (2.6 σ) to a large (6.78 σ) cut-off radius. Thus, the asymmetry that was felt by particles due to the presence of the interface extended far into both phases. This would imply that a big difference is to be expected between

using our new expressions and rough estimates of long-range corrections, especially since our cut-off radius is not that large. No such differences were observed however. The reason for this may be that liquid-vapour interfaces and crystal-liquid interfaces differ in the density change upon crossing the interface. At least for monatomic systems, this change is quite small for the crystal-liquid interface and comparatively large for the liquid-vapour interface. (In our case $\rho_s/\rho_l = 1.135$).

There is another, more pragmatic, problem with our new expression. In order to use it at runtime in a simulation, one has to be able, at every single timestep, to tell the amount of solid and liquid material in the system. For this, we could use our solid-particle recognition criterion (see *Chapter 2*) but that slightly overestimates the amount of liquid material since it assigns most of the (diffuse) interface to the liquid phase. Another method, which connects more closely to the derivation we used in the appendix, is to look at the total instantaneous volume of the system. Since we know from our bulk simulations the volumes per particle for each phase, we could at every instance calculate the proportion between solid and liquid phases. This however, does not work either. Since instantaneous volume fluctuations will also take place in the bulk parts of the two-phase system, our average particle volumes are not a good measure. As a consequence, at certain instances, our prediction for α could exceed 1 or drop below 0. As can be seen from Fig. 4.2, the new expression diverges close to these values. Any other method that could be suggested to distribute the material over the two phases would suffer from comparable inaccuracies. Since the associated errors are most probably larger than the difference between the two expressions, we decided to keep using the overall average density in calculating instantaneous corrections to the pressure and the energy.

4.3 Equilibrating the two-phase system

In *Chapter 3*, we showed that proper preparation of the two-phase system plays a crucial role in the resulting growth and melting rates. There, we combined fully equilibrated bulk phases of liquid and solid in one simulation box. To release excessive potential energies due to particle overlap, 300 timesteps of NVT simulations were performed with rigid temperature scaling at every timestep. Thereafter, NPT runs were carried out at the appropriate temperatures and $P = 2.512 \times 10^{-3}$ to study growth and melting. We found that the crystals that were grown in the NPT simulations contained just a little more 'imperfections' (as defined by our solid-liquid discriminator, see *Chapter 2*) than the crystals that were melted directly after equilibration. This resulted in a clear asymmetry of growth and melting. It was also shown that imperfections eventually appeared in the crystalline phase when the system was run for a long time at the equilibrium temperature, which means that the crystals with imperfections really represent the thermodynamically favoured state. It was argued that the crystals lacking imperfections melt more slowly than realistic crystals would do. Indeed, when the crystals grown in the crystallization runs were used for the melting runs, the asymmetry was shown to disappear. Thus, an extensive and careful equilibration of the system at the melting point will most probably also give a symmetric behaviour of growth and melting.

In the present study, we chose to perform such a careful equilibration. Like before, we

carried out bulk simulations of liquid and solid phases at the appropriate densities, but this time only at the melting temperature. The densities were found by doing several NPT runs of the bulk phases at different temperatures and fitting the average volumes as a function of temperature. For the average volumes per particle this led to (in Lennard-Jones units):

$$v_l = 1.0312 - 0.15802 \times T + 0.53748 \times T^2 \tag{4.5}$$

and

$$v_s = 1.0513 - 0.34068 \times T + 0.46830 \times T^2, \tag{4.6}$$

for $0.640 < T < 0.747$.

First, we needed an estimate of the equilibrium temperature T_m. For this we used the most accurate collection of thermodynamic data for the Lennard-Jones system at this moment, the Johnson data for the liquid [100] and the van der Hoef data for the solid [85]. From these data we calculated the chemical potentials at the desired pressure and sought for the temperature at which the chemical potentials of the solid and the liquid are equal. This gave an estimate of $T_m = 0.687$. At this temperature, we performed a two-phase NVT simulation and measured the pressure. Next we slightly changed the temperature until the pressure reached the desired value. From this we found $T_m = 0.69659$ and thus, with the above fits, $v_l^{\mathrm{eq}} = 1.1819$ and $v_s^{\mathrm{eq}} = 1.0412$. At this temperature and pressure, the equations of Johnson and van der Hoef give $v_l = 1.1838$ and $v_s = 1.0446$, in quite good agreement with our calculations. The agreement of both the melting point and the associated densities is almost perfect, given the fact that for simple systems, the curves of free energies of the two phases vs. temperature have very similar slope. Thus a small error in the free energy of one phase with respect to the other leads to a large error in the predicted transition point.

With the densities found above, we performed NVT simulations of the bulk phases at the equilibrium temperature. Here the liquid boxes were elongated along the z-direction and were given the same cross-sectional areas in the x,y-plane as the solid boxes. The bulk simulations were first run for 100,000 timesteps of equilibration, whereafter co-ordinate files were written once every 1000 timesteps for 50,000 more timesteps in total. To make two-phase boxes, one liquid configuration and one solid configuration were taken, both copied four times in the z-direction, and subsequently put on top of each other. The resulting systems contained two solid-liquid interfaces and consisted of 2000 initially crystalline particles ($5 \times 5 \times 20$ unit cells) and 2048 particles initially belonging to the liquid phase.

This is the point were the new procedure starts to deviate from the one in the previous chapter. We used to continue with 300 timesteps of strict temperature scaling to release the particle-particle overlap caused by the combination of the two phases. Upon closer examination, however, it appeared that this had the side effect of removing any 'imperfections' that were present in the bulk crystal phase. So the imperfections, which belong to a well-equilibrated crystal, disappeared just because of those (very short!) simulations with strict temperature scaling. Therefore we decided to keep the solid phase atoms frozen at their positions and applied 750 timesteps of strict temperature scaling to the liquid only. This proved to be enough to get rid of most of the overlap energies. Thereafter the liquid was equilibrated for 100,000 timesteps, while still constraining the crystal to its original configuration. This

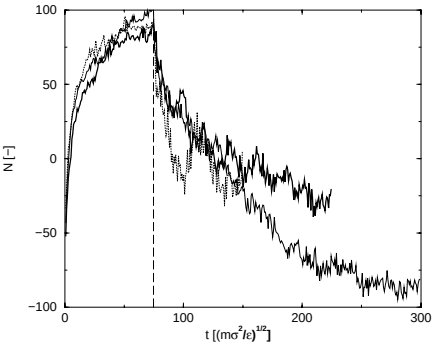

Figure 4.3: Increase and decrease of the number of solid-like particles during the equilibration process. Shown are the results for three different box sizes: 4048 particles (thin solid line), 8096 particles (thick solid line), and 16192 particles (dotted line). The dashed line denotes the point after which the crystal is allowed to relax.

way, the liquid was equilibrated against a crystal with the correct amount of imperfections, but with a temperature of essentially zero Kelvin. Therefore, the equilibration should not be extended too long, in order to avoid excessive 'freezing' of the liquid on the crystalline surface. After the liquid equilibration, the solid was finally relaxed as well and the whole system was run another 300,000 timesteps of equilibration. During the whole procedure, we counted the number of solid-like particles using our recognition function. This was done for 50 runs of different starting configurations and subsequently averaged at each time. We found that this number of 50 runs gave a good trade-off between accuracy and computational cost. We will also discuss this in the next section (Fig. 4.5).

Results for the averaged equilibration curves are shown in Fig. 4.3. Apart from the results of the 4048 particle system, curves are also shown for systems of double and quadruple size. In order to monitor processes at the interface, all three curves were shifted downwards by the number of solid particles that corresponds to the sizes of the bulk systems that were combined. In the bulk crystal simulations, on average 94.18 % of the particles were classified as solid particles by our discriminator. In the bulk liquid simulations, this was 0.05859 %. Accordingly the curve of the small box was shifted down by $0.9418 \times 2000 + 0.0005859 \times 2048 = 1885$ particles. The other curves were shifted by 3770 and 7539 particles, respectively.

All curves start below zero, as a result of the 750 timesteps with strict temperature scaling (not included in the figure) and the fact that particles that 'see' a crystal on one side and a liquid on the other, will no longer be classified as solid-like. (If it had been only for the latter effect, one would have expected a value of -100, corresponding to 2 interfaces of 50 atoms.) During the equilibration of the liquid against the constrained solid, the amount of crystalline material increases. This happens because a crystal-like interface is built up in the contact region between both phases. After the release of the solid phase, the amount of crystalline material drops again, because of relaxation in the crystalline part of the interface. For the smallest box, equilibrium is only reached after approximately 300,000 timesteps (corresponding to a simulation time of $224.4\ \sqrt{m\sigma^2/\varepsilon}$), which is extremely much larger than most other studies so far have assumed to be sufficient. The two larger boxes need less time to reach equilibrium. Note also that the double and quadruple box seem to converge to approx-

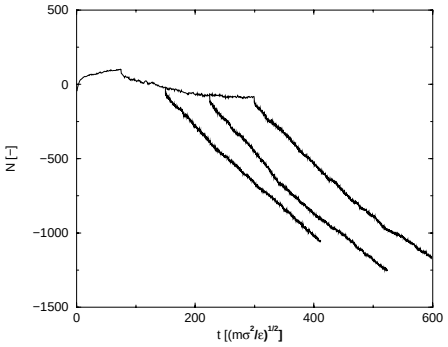

Figure 4.4: Melting curves at $T = 0.714\varepsilon/k_B$ started from three different stages in the equilibration process.

imately the same value of N. We will come back to these observations later when we discuss the system size effects on our production runs.

4.4 Nonequilibrium simulations

To carry out production runs of crystallization and melting, the well-equilibrated two-phase systems were quenched to the desired temperatures, by reassigning velocities from a Gaussian distribution with the appropriate mean and width. Then simulations were carried out in the NPT ensemble, with a Nosé-Hoover thermostat and barostat, applying the same parameters as in the bulk simulations (Sec. 4.2.1). The barostat was adopted such that the volume relaxation in the x-, y-, and z-directions took place independently. The production runs were again carried out over 50 independent starting configurations (the end configurations of the equilibration runs) at each temperature. During the runs, the number of crystalline particles was calculated once every 100 timesteps. Results of the 50 runs were subsequently averaged.

One example of an averaged melting run is shown in Fig. 4.4. To investigate the influence of equilibration time, we started melting runs from three different stages in the equilibration (100, 200, and 300 thousand timesteps after the release of the crystal phase). All three cases show an initial rapid drop of the number of crystalline particles. This reflects the relaxation of the system to the new temperature. Simultaneously, the volume of the box increased by a corresponding amount. After this short period, the (averaged) temperature and pressure had relaxed to their desired values.

Shortly after the initial box relaxation, the system started to melt with a constant velocity in both three cases. The experiment with the shortest equilibration time melted somewhat slower than the two others. A remarkable feature, however, of all three cases, is that they displayed a second regime, where the melting was again linear in time but took place at a smaller rate than initially. This crossover from an initial to a second regime was clearly noticeable for most of the temperatures at which we performed our measurements, though less pronouced for the crystallization runs than for the melting runs and less pronounced for temperatures very close to equilibrium. Note, however, that the effect is also quite subtle:

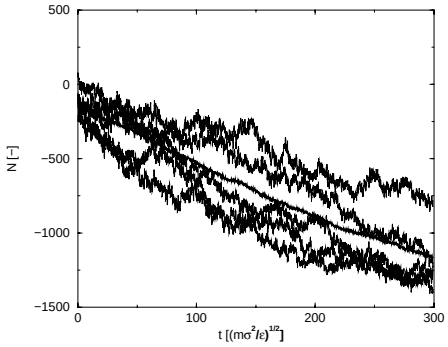

Figure 4.5: Melting curves at $T = 0.714\varepsilon/k_B$ showing a selection (5 runs) from different starting configurations, as well as the average over 50 runs (thick line).

in order for the effect to be seen, it is necessary to carry out averaging over many different runs. This is shown in Fig. 4.5, where a selection of single runs is drawn together with the curve averaged over all 50 boxes. On the temperature range that we study, the fluctuations of N_s in one single run are of the same order as the differences between the averaged curves of different temperatures.

The discovery of two distict regimes of growth and melting raises two questions: *'Is this an artefact of the simulation method (e.g. an effect of system size), or is it a real, physical effect?'* and *'If it is not an artefact, which one of the two regimes corresponds to the rates that are to be associated with macroscopic crystal growth such as would be seen in experiments?'*

In order to study system size effects, we repeated our simulations for systems of twice and four times the originial sizes. We could have constructed the new two-phase boxes by taking 8 or 16 periodic images of the bulk phases (instead of 4 for our smaller system). However, we chose to do the bulk (NVT) simulations anew at the actual sizes that we needed in the two-phase simulations. In this way, we made sure that we combined two completely randomized phases and did not introduce any undesired periodicity. In *Chapter 8* where we study density fluctuations of adsorbed species in nanopores, we will see that in order to sample long-wavelength fluctuations of the order of the box size, one has to completely randomize initial positions of the particles over the whole pore. There it will prove not to be sufficient, say, to divide the pores in four sections of equal length and distribute a fourth of the particles randomly over each of the sections (see Sec. 8.4). To summarize, the two-phase systems of 8096 particles were constructed from bulk liquids of 4096 particles and bulk solids of 4000 particles, and the two-phase systems of 16192 particles were constructed from bulk phases of 8192 and 8000 liquid and solid particles, respectively.

The resulting averaged curves for the same temperature as in Fig. 4.5 are shown in Fig. 4.6. The most striking feature of this graph is that all three curves seem to start with the same initial slope and to end with approximately equal slopes as well. Only the time over which the initial regime extends seems to shorten substantially with increasing box size. We suggest that both regimes belong to a physical process, which is reflected by the fact that neither slope does change significantly upon enlarging the box size. Since the second regime seems to be

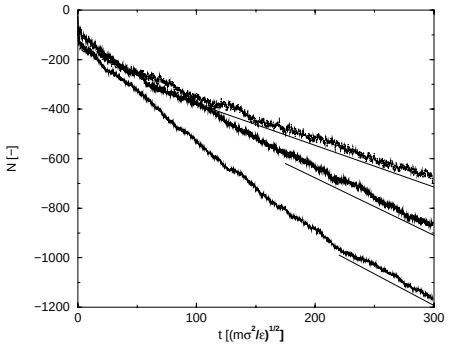

Figure 4.6: Averaged melting curves at $T = 0.714\ \varepsilon/k_B$ for different box sizes with a total number of particles of 4048 (50 runs, thin solid line), 8096 (50 runs, thick solid line), and 16192 (32 runs, dotted line), respectively.

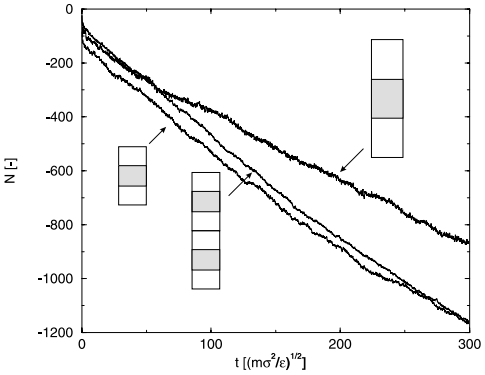

Figure 4.7: Comparison of melting curves for the small and intermediate box sizes, where either both phases are doubled or the whole system is copied twice.

persistent and becomes increasingly dominant when the system is enlarged, we infer that this regime is to be associated with the macroscopic limit of crystal growth (or melting). As can be seen from the figure, the slope of the second regime still changed somewhat upon enlarging the size, but for computational reasons we decided the results of the intermediate boxes were converged satisfactorily (this was a generic trend for all temperatures).

The initial regime may be a relaxation of the interface reflecting a change from the equilibrium shape at the melting point to a steady-state shape belonging to the actual temperature of the experiment. This is in accordance with kinetic mean field results of Williams, Moss, and Harrowell [189].

One might argue that if local density fluctuations are crucial and only the total number of particles in the simulation plays a role in the size of these fluctuations, the effect should also be seen in a system that is built as two copies of the original box (thus containing four interfaces per simulation cell). This we checked by comparing the results from the small box with those from the intermediate box and those from a system that was made by copying the small box twice in the z-direction. The results are shown in Fig. 4.7. One can see that the larger fluctuations in the 'doubled small' box give ease to a better buildup of the equilibrium interface (reflected in the starting point of the melt run which is close to that of the large box). In the nonequilibrium situation, however, the long-time behaviour is close to that of the small box. Thus it is really the bulky behaviour of the large phases in the larger box that makes the interface relax to its nonequilibrium shape. Note again that our 'small' system is of comparable size or larger than the maximum system sizes of most other studies. This means that those studies probably have been investigating interface relaxation rates rather than macroscopic crystal growth rates.

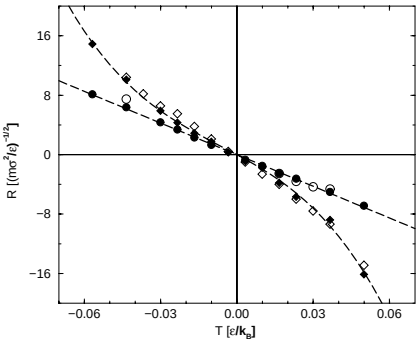

Figure 4.8: Dependence upon the supersaturation (deviation of the temperature from equilibrium) of the initial (pyramids) and long-time (circles) growth and melting rates. Shown are the results for the small (open symbols) and intermediate (closed symbols) box sizes.

A second concern that might be raised is that immediately after the initial quench, the crystal starts to grow (or melt) thereby releasing (consuming) latent heat of fusion. If the thermostat would not be able to remove all of the extra heat, the interface may heat up (cool down) until balance is reached between heat production and heat transport. This effect would slow down both growth and melting rates, since the final temperature at the interface would then be closer to the melting point than the overall temperature. In order to investigate this, we did a thorough study of temperature profiles by monitoring local averages of the kinetic energy, both averaged over the whole run and followed as time evolution. In neither case did we find any noticeable deviation of the interface temperature from the overall temperature. From this we conclude that our thermostat relaxation time was chosen small enough so as to effectively produce constant temperature experiments.

4.5 Temperature dependence of growth and melting rates

We carried out simulations with the small and intermediate boxes at several different temperatures below and above the equilibrium temperature. For all experiments, averages were calculated over 50 different initial configurations. The small box systems were equilibrated over 100,000 timesteps with frozen crystal configurations and 300,000 timesteps with the whole system relaxed, while the intermediate box systems were equilibrated over 100,000 steps with a frozen crystal and 200,000 steps with both phases relaxed. For the small systems, the initial slopes were calculated easily, but the second regime was only accurately measured in one growth and four melting experiments. The reason for this was that close to equilibrium, the second regime was not found, and far from equilibrium, there was only a very short time of second regime (if any) before the system had grown one of the two phases so far that the two interfaces in the box started to interact. Most of the intermediate size experiments showed both regimes over a substantial time. The results are shown in Fig. 4.8. It can be seen that over the whole range of temperatures studied, the agreement between both

system sizes is good. The long-time regime rates are perfectly linear with respect to temperature. We think that this is clear evidence of the Ansatz of Tammann [165] and supplies an extra confirmation of the fact that the long-time regime is indeed to be associated with the macroscopic limit of growth and melting.

The initial rates are not linear in temperature. This implies that improper equilibration might be one of the reasons why earlier researchers (including ourselves) have found nonlinearities or slope-discontinuities around equilibrium in the dependence of growth rates upon under- and supersaturation, even for roughly growing surfaces.

Finally, we investigated the dependence of the crossover time between the two regimes upon temperature. We started to make a linear fit through the second-regime growth rates (denoted by R_2). This resulted in:

$$R_2^{\text{fit}}(T) = 99.052 - 142.07\,T \tag{4.7}$$

Note that this leads to a definitive estimate of the equilibrium temperature for our system of $T_m = 0.6972\varepsilon/k_{\text{B}}$, in very close agreement with our earlier estimate. Next we fitted the initial-regime growth rates with a third-order polynomial in ΔT (the deviation of the temperature from equilibrium). This resulted in

$$R_1^{\text{fit}}(T) = -184.19\,\Delta T - 739.39\,\Delta T^2 - 38291\,\Delta T^3 \tag{4.8}$$

The accuracies of these fits can be appreciated from Fig. 4.8.

Now, for each experiment, we did not only measure the slopes of the growth curves, but also the intercepts with the N-axis. We fitted the intercepts (denoted A) of the initial regimes with a third-order polynomial in ΔT:

$$A_1^{\text{fit}} = -10.2 - 3850.4\,\Delta T - 17694\,\Delta T^2 + 1.2236 \times 10^5\,\Delta T^3 \tag{4.9}$$

Next we fitted the intercepts of the second regimes, while constraining the zeroth order term to the value of the initial intercepts. This means forcing both curves to coincide at equilibrium ($\Delta T = 0$).

$$A_2^{\text{fit}} = -10.2 - 6443.4\,\Delta T - 39576\,\Delta T^2 - 1.8772 \times 10^5\,\Delta T^3 \tag{4.10}$$

The results are shown in Fig. 4.9. The difference between A_1^{fit} and A_2^{fit} can be interpreted as a measure for the difference between the widths of the nonequilibrium interface and the equilibrium interface. The points at which both fits $A_i^{\text{fit}} + R_i^{\text{fit}} \times t$ intersect are our estimates for the crossover times:

$$t_{\text{cross}} = \frac{2593.0 + 21882\,\Delta T + 3.1008 \times 10^5\,\Delta T^2}{42.12 + 739.39\,\Delta T + 38291\,\Delta T^2} \tag{4.11}$$

In Fig. 4.10, we have drawn all growth and melting curves for the intermediate box size, including the fits to the linear regimes as well as Eq. 4.11. As can be clearly seen, the crossover time grows large upon approaching equilibrium, while at the same time the initial and the second-regime rates grow more and more equal.

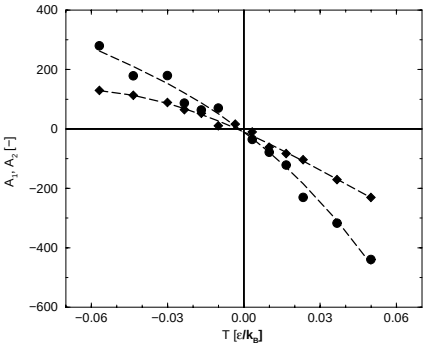

Figure 4.9: Temperature dependence of intercepts A_1 (diamonds) and A_2 (circles) of the growth and melting curves. The dashed lines represent the fits of Eqs. 4.9 and 4.10.

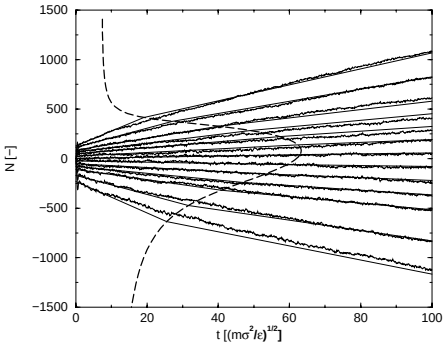

Figure 4.10: Growth and melting curves for all temperature at intermediate box size, showing both the measurement data and the fits to the initial and final slopes. The dashed line shows the calculated crossover times between both regimes.

4.6 Conclusions

We presented the most accurate simulations to date of crystal growth and melting rates of the Lennard-Jones (100) face at temperatures close to equilibrium. We proposed a way to carefully equilibrate two-phase systems to carry out subsequent nonequilibrium simulations and showed that our solid-liquid recognition function supplies a powerful tool to monitor the equilibration process.

We discovered two linear regimes. The initial regime was associated with interface relaxation and was shown to be most dominant for small system sizes and close to equilibrium. The second regime was associated with the macroscopic limit of growth and melting. The linear dependence of the macroscopic rates upon temperature provides clear evidence of the early observation of Tammann that roughly growing surfaces with one type of interaction sites can not have a slope discontinuity in the rate-temperature curve. This contrasts some earlier simulation studies. We showed that improper equilibration of the two-phase systems can result in the observation of only the initial (interface relaxation) regimes. Since these were shown not to vary linearly with temperature, some (or all) of the earlier observations of a slope discontinuity may be explained by this.

Now that the necessary hardware requirements have come into reach, it has become possible to study the effect of system size and simulation times upon dynamic measurements of two-phase systems. The results in this chapter prove that both of these have to be (much) larger than generally accepted in order to arrive at the correct rates. This reflects the fact that the interface present in two-phase systems has an effective interaction range that is appar-

ently much larger than any measure of the interface width would suggest. We think this study provides a good guideline to what dimensions should be used in such systems and may be a suitable starting point to study crystal-melt systems of more complex molecules, where the molecular correlation lengths are already much larger.

4.A Appendix. Long-range corrections to the pressure in a two-phase Lennard-Jones system

In this appendix, we derive an expression for the long-range correction to the pressure in a system where two phases are present. We restrict ourselves to the case of a pure substance (the interactions between all particles are identical), the only difference between the two phases being their respective densities. We write the pressure as $-1/6V$ times a double integral over space of the densities at two positions $\mathbf{r}_1$ and $\mathbf{r}_2$ multiplied by the virial function w, whose value depends on the distance r between $\mathbf{r}_1$ and $\mathbf{r}_2$. In the case of simple Lennard-Jones particles, this function reads

$$w(r) = r\frac{d\phi^{\mathrm{LJ}}}{dr} = -\frac{48}{r^{12}} + \frac{24}{r^6}. \tag{4.A.1}$$

In the integral, position $\mathbf{r}_1$ probes all material in the simulation box, so this co-ordinate is restricted to the box volume V, while the second co-ordinate represents all of the surroundings of the first one and thus, in principle, extends over infinite space:

$$P = -\frac{1}{6V}\int_V d\mathbf{r}_1 \int_\infty d\mathbf{r}_2 \rho(\mathbf{r}_1)\rho(\mathbf{r}_2) w(|\mathbf{r}_2 - \mathbf{r}_1|)\,. \tag{4.A.2}$$

Note that in the calculation of the 'uncorrected' pressure, the integral reduces to a double sum over nearest images, since all interactions beyond the cut-off radius are zero and box dimensions should be such that non-nearest images are more than r_c apart.

For the construction of the long-range correction, we apply the usual assumption [5] that beyond the cut-off radius, the central particle only 'sees' average surroundings (which for a pure substance comes down to assuming $g(r) = 1$ for $r > r_c$). Because of this assumption, we may substitute the average densities of the respective phases for $\rho(\mathbf{r})$, where the choice for either ρ_l or ρ_s depends on the region of the corresponding integral. Since there are two different phases, that can appear in four combinations, the long-range correction to the pressure can be split into four distinct integrals:

$$\begin{aligned} P_{\mathrm{lrc}} = & \\ -\tfrac{1}{6V} L_x L_y \rho_l \int_0^{\alpha L_z} dz_1 \; \Bigg\{ & \int_{-\infty}^{+\infty} dx_2 \int_{-\infty}^{+\infty} dy_2 \int_0^{+\infty} dz_2 \rho_l w(|\mathbf{r}_2 - \mathbf{r}_1|)\,\Theta(|\mathbf{r}_2 - \mathbf{r}_1| - r_c) \\ & + \int_{-\infty}^{+\infty} dx_2 \int_{-\infty}^{+\infty} dy_2 \int_{-\infty}^{0} dz_2 \rho_s w(|\mathbf{r}_2 - \mathbf{r}_1|)\,\Theta(|\mathbf{r}_2 - \mathbf{r}_1| - r_c) \Bigg\} \end{aligned}$$

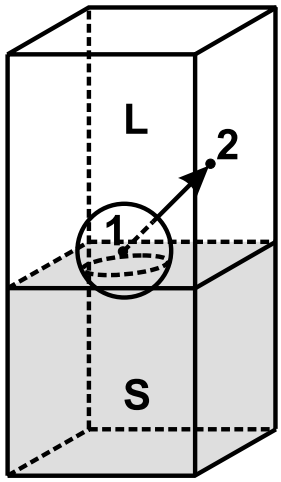

Figure 4.11: Sketch of the integration space as meant in Eq. 4.A.3. Position 1 traverses the whole simulation box while position 2 traverses infinite space. The drawn sphere denotes the volume within a radius r_c of position 1, which is excluded from the integral by means of the unit step function Θ.

$$-\tfrac{1}{6V}L_xL_y\rho_s \int_{-(1-\alpha)L_z}^{0} dz_1 \Bigg\{ \int_{-\infty}^{+\infty}dx_2\int_{-\infty}^{+\infty}dy_2\int_{0}^{+\infty}dz_2\rho_l w\left(|\mathbf{r}_2-\mathbf{r}_1|\right)\Theta\left(|\mathbf{r}_2-\mathbf{r}_1|-r_c\right) + \int_{-\infty}^{+\infty}dx_2\int_{-\infty}^{+\infty}dy_2\int_{-\infty}^{0}dz_2\rho_s w\left(|\mathbf{r}_2-\mathbf{r}_1|\right)\Theta\left(|\mathbf{r}_2-\mathbf{r}_1|-r_c\right)\Bigg\}, \qquad (4.A.3)$$

where the unit step function Θ is used to denote that only the region outside the cut-off range is taken into account. The integration space covered by the above expression is schematically drawn in Fig. 4.11.

If we take the further (legitimate) assumption that r_c is smaller than the length of either of the two phases along the z-direction, the above expression can be elaborated upon to give

$$\begin{aligned} P_{\rm lrc} = & \\ & -\pi\rho_s^2\left\{\left(\frac{16}{3}(1-\alpha)-2\beta+\frac{\beta^3}{3(1-\alpha)^2}\right)\frac{1}{r_c^3}-\left(\frac{32}{9}(1-\alpha)-\beta+\frac{\beta^9}{45(1-\alpha)^8}\right)\frac{1}{r_c^9}\right\} \\ & -\pi\rho_l\rho_s\left\{\left(4\beta-\frac{\beta^3}{3\alpha^2}-\frac{\beta^3}{3(1-\alpha)^2}\right)\frac{1}{r_c^3}-\left(2\beta-\frac{\beta^9}{45\alpha^8}-\frac{\beta^9}{45(1-\alpha)^8}\right)\frac{1}{r_c^9}\right\} \\ & -\pi\rho_l^2\left\{\left(\frac{16}{3}\alpha-2\beta+\frac{\beta^3}{3\alpha^2}\right)\frac{1}{r_c^3}-\left(\frac{32}{9}\alpha-\beta+\frac{\beta^9}{45\alpha^8}\right)\frac{1}{r_c^9}\right\}, \end{aligned} \qquad (4.A.4)$$

where we have used the following substitutions:

$$\begin{aligned} \alpha &= V_l/V = 1-V_s/V \\ \beta &= r_c/L_z. \end{aligned} \qquad (4.A.5)$$

The expression that has been found should be checked to give known results in limiting cases. The most obvious one is to take the densities of the two phases equal ($\rho_l=\rho_s$). This

leads to

$$P_{\text{lrc}} = -\pi\rho^2 \left(\frac{16}{3}\frac{1}{r_c^3} - \frac{32}{9}\frac{1}{r_c^9} \right), \tag{4.A.6}$$

which is equal to the well-known expression for the long-range correction to the pressure in a pure Lennard-Jones substance [5].

Another limit that could be looked at is the limit of infinite system size ($L_z \to \infty$, and thus $\beta \to 0$). In that limit the influence of the interface should become unimportant. The resulting expression is

$$P_{\text{lrc}} = -\left[\alpha\pi\rho_l^2 + (1-\alpha)\pi\rho_s^2\right] \left(\frac{16}{3}\frac{1}{r_c^3} - \frac{32}{9}\frac{1}{r_c^9} \right), \tag{4.A.7}$$

which can be seen as the analogue of Eq. 4.A.6, but in this case a squarely weighted average of the densities shows up. This is because the density appears as a square in the pressure expression.

It is instructive to see what would happen if one would just use the standard long-range corrections. This comes down to neglecting the situation of two different phases and just taking the number average density of the system as a whole:

$$\begin{aligned} \bar{\rho} &= \frac{N_l + N_s}{V} = \rho_l \frac{V_l}{V} + \rho_s \frac{V_s}{V} \\ &= \alpha\rho_l + (1-\alpha)\rho_s. \end{aligned} \tag{4.A.8}$$

This leads to

$$P_{\text{lrc}} = -\pi\left[\alpha\rho_l + (1-\alpha)\rho_s\right]^2 \left(\frac{16}{3}\frac{1}{r_c^3} - \frac{32}{9}\frac{1}{r_c^9} \right). \tag{4.A.9}$$

Note the subtle difference with expression 4.A.7.

5 Crystal growth and interface relaxation rates from equilibrium fluctuations

In this chapter, the kinetic coefficient of crystallization is calculated according to the previously introduced equilibrium method [Chapter 2]*. The existence of two regimes of interface relaxation and macroscopic growth, such as they were found in* Chapter 4*, is fully confirmed by the results of the equilibrium method. Special attention is given to the relation between pressure fluctuations and fluctuations of the amount of crystalline material. Furthermore, we investigate the density and order parameter profiles of the interface and make a clear distinction between the instantaneous structure and the time-averaged profile which is usually presented.*[*]

5.1 Introduction

Over the past few decades, molecular dynamics (MD) simulations have proved to be an extremely powerful tool in the study of crystal growth and melting processes [95, 118, 121]. Given the experimental difficulty in probing the interface between two dense phases, the atomistic details coming from MD methods have provided an excellent alternative in understanding the processes taking place at the interface.

Much information has been obtained on the structure (e.g., diffuseness, anisotropy) of various crystal-melt interfaces [46, 82, 89, 97], but on the dynamics of crystal growth from the melt there are still some open questions, even for the simplest model systems. As an example, concerning the growth and melting rates of atomic systems, there has been much debate on whether a slope discontinuity in the rates exists upon crossing the melting point. Such a singularity was claimed by Tymczak and Ray [177, 178] in their study of crystallization and melting kinetics in sodium, in clear contradiction with earlier theoretical considerations [165, 180]. In *Chapter 4* we did a very accurate investigation of growth and melting rates of the Lennard-Jones FCC (100) surface close to equilibrium. From this we were able to rule out the possibility of a singularity at the melting point and argued that any such findings for similar systems must be due to an artefact of the simulation.

[*] The work described in this chapter has been submitted to J. Chem. Phys. [171]

One of the main problems to get accurate dynamics data out of simulations of two-phase systems is that it is extremely difficult to ensure a properly prepared nonequilibrium interface. The crystalline surface induces order which extends far into the liquid, and dynamic correlation lengths are probably even much longer. In *Chapter 3*, for instance, we found a clear slope discontinuity between crystallization and melting rates. This was shown to disappear with the incorporation of lattice imperfections in the crystal that were only obtained after proper equilibration.

In *Chapter 4* we found that when nonequilibrium growth simulations were started after extensive equilibration of the system at the melting point, considerable time was needed for the interface to relax to its nonequilibrium shape (i.e., the shape that corresponds to the circumstances of the experiment). We discovered two regimes of linear growth: a short-time regime associated with interface relaxation and a long-time regime associated with the macroscopic limit of growth and melting. We studied the influence of size effects and found that the second regime could only be measured accurately for sufficiently large systems (larger than mostly used in earlier simulations). In a system of $8.044\sigma \times 8.044\sigma \times 69.595\sigma$ (4048 atoms), the initial regime lasts much longer than in a system of $8.044\sigma \times 8.044\sigma \times 139.19\sigma$ (8096 atoms), which makes an accurate calculation of the long-time dynamics in the smaller system quite cumbersome. To sum up, in simulations where two phases are combined, it is of utmost importance to take large enough system sizes, equilibration times and run times, meaning generally much larger than in simulations of bulk systems.

In *Chapter 2* we introduced a method to extract the kinetic coefficient (i.e., the slope of the rates R vs. temperature T) from fluctuations of the number of solid particles in one simulation at equilibrium. Apart from avoiding the computational cost of having to do numerous nonequilibrium simulations at a range of temperatures, this method has the advantage that the simulations can be carried out principally *ad infinitum*, providing as accurate statistics as one wishes. Unless special measures are taken against it, nonequilibrium simulations are limited to the time during which the whole box becomes crystalline or liquid. Given the enormous growth rates for atomic systems, this time can become unmanageably short even for moderate supersaturations.

It is the main goal of the present paper to investigate whether the equilibrium method gives accurate results for the system sizes of our previous nonequilibrium study (i.e., 4048 and 8096 atoms, respectively). In particular, we would like to find further evidence for the presence of two growth regimes. A second objective is to find a method to calculate the kinetic coefficient of normal growth exclusively using data from one and the same two-phase equilibrium simulation, where in our previous approach we needed external input to calculate this coefficient.

The paper is organized as follows. First we will briefly describe the model system and the way we carried out the equilibration. Then we will study the relation between number fluctuations and pressure fluctuations. We will suggest the substitution of a factor from the original derivation (containing equilibrium thermodynamic properties of the bulk phases) by a correlation factor which can be measured directly in the two-phase system. We will elaborate on this by considering the influence of fluctuations of the pressure that are not directly related to fluctuations of the amount of crystalline material. In the subsequent section, we will compare the prediction of the kinetic coefficient from the equilibrium method with

the nonequilibrium data from the previous study and discuss the influence of system size on the accuracy. After this, we will describe in detail the structure of the interface and make a clear distinction between instantaneous interface profiles and the overall, time-averaged, profile which is usually presented. We close with discussion and suggest several routes for future investigations.

5.2 Simulations

In this study, we performed extensive simulations of the two-phase atomic crystal-melt system at equilibrium. In all cases, the direction of growth was perpendicular to the FCC (100) surface. Interatomic interactions were modelled by the Lennard-Jones potential, so that all properties will be presented in Lennard-Jones units (i.e., ε for unit energy, σ for unit length, and $(m\sigma^2/\varepsilon)^{1/2}$ for unit time). In *Chapter 4* the equilibrium temperature for this system was estimated to be $T^{\mathrm{eq}} = 0.6972\ \varepsilon/\mathrm{k_B}$ at a pressure of $P = 2.512 \times 10^{-3}\ \varepsilon/\sigma^3$. This is also the state point for our present simulations, which were all carried out at constant number of particles (N), constant volume (V), and constant temperature (T).

The simulations were performed with the DL_POLY package [162], applying Nosé-Hoover dynamics to keep the average temperature at the desired value. We employed a timestep of $7.480 \times 10^{-4}\ \sqrt{m\sigma^2/\varepsilon}$ and a thermostat relaxation time of $\tau_T = 0.0748\ \sqrt{m\sigma^2/\varepsilon}$. (See *Chapter 4* for an extensive discussion of the tuning of these parameters.) Two box sizes were studied: a total of 4048 particles and a total of 8096 particles. In correspondence with our previous study, these sizes will be referred to as the 'small' and the 'intermediate' box size, respectively.

To properly equilibrate the two-phase systems, we started with NVT simulations of bulk liquid (2048 and 4096 particles, respectively) and bulk crystal (2000 and 4000 particles, respectively). Both the liquid and the crystal boxes were constructed with equal cross-sectional areas in the x- and y-directions (5×5 unit cell lengths) and with elongated axes in the z-direction to give the desired equilibrium volumes (at this state point, $v_l = 1.1823\ \sigma^3$ and $v_s = 1.0414\ \sigma^3$). After 100,000 timesteps of bulk simulations, we wrote configuration files once every 1000 timesteps. From those configuration files, one liquid and one crystal box were put on top of each other (in the z-direction) to create two-phase simulation boxes. For both system sizes we thus created four different samples.

In order to release excessive potential energies due to particle overlap in our two-phase system, we performed 300 timesteps of NVT simulations with rigid temperature scaling at every step. Thereafter, 200,000 timesteps of Nosé-Hoover dynamics were carried out before production runs were started. Production runs from which the data in this study were gathered lasted for 20,000,000 timesteps for the small box and 10,000,000 for the intermediate box.

5.3 Correlation between pressure fluctuations ΔP and number fluctuations ΔN_s

In this section, we will briefly review the derivation of Eq. 2.10 and investigate if the factor that contains bulk equilibrium parameters can be replaced by a factor that can readily be obtained from the two-phase simulation. Special attention will be given to the correlation between pressure and number fluctuations and to the difference in decay of the autocorrelation of both of them.

In *Chapter 2* we introduced an order parameter Ψ to assign particles either to the solid or to the liquid phase. Thus we could, at every instant, calculate the deviations $\Delta N_s = N_s - N_s^{\mathrm{eq}}$ of the number of 'solid-like' particles from their equilibrium value N_s^{eq}. We measured the decay of fluctuations of N_s

$$\langle \Delta N_s(t)\Delta N_s(0)\rangle = \langle \Delta N_s(0)\Delta N_s(0)\rangle \exp\{-t/\tau\}, \tag{5.1}$$

which we could relate to the kinetic coefficient k that represents the temperature dependence of growth and melting rates close to equilibrium:

$$R(T) = k\frac{\mu_l - \mu_s}{k_{\mathrm{B}}T} \approx -k\frac{h_l^{\mathrm{eq}} - h_s^{\mathrm{eq}}}{k_{\mathrm{B}}T}\frac{\Delta T}{T^{\mathrm{eq}}}. \tag{5.2}$$

(Note that in the present chapter we present growth rates in terms of numbers of particles per unit time, instead of distance per unit time as in *Chapter 2*. Therefore the factor A/a in Eq. 2.10 and d in Eq. 2.12 will be dropped.)

The basic assumption we make is that number fluctuations ΔN_s induce a volume and consequent pressure change of the crystal and the liquid phase which is instantaneous and homogeneous throughout both phases. In other words, we propose that mechanical equilibrium be reached on a much shorter timescale than the timescale of the crystallization process. The pressure change results in a chemical potential difference between both phases, which acts as the driving force back to equilibrium:

$$\begin{aligned}
\frac{d\Delta N_s}{dt} &= \frac{k}{k_{\mathrm{B}}T}(\mu_l - \mu_s) \\
&= \frac{k}{k_{\mathrm{B}}T}\left\{\left(\frac{\partial \mu_l}{\partial P}\right)_T^{\mathrm{eq}}\Delta P - \left(\frac{\partial \mu_s}{\partial P}\right)_T^{\mathrm{eq}}\Delta P\right\} \\
&= \frac{k(v_l^{\mathrm{eq}} - v_s^{\mathrm{eq}})}{k_{\mathrm{B}}T}\Delta P,
\end{aligned} \tag{5.3}$$

where in the second line we have used the equilibrium condition $\mu_l^{\mathrm{eq}} = \mu_s^{\mathrm{eq}}$.

Now we need a relation between ΔP and ΔN_s, which is provided by the condition of constant total volume:

$$\begin{aligned}
V &= (N_l^{\mathrm{eq}} - \Delta N_s)(v_l^{\mathrm{eq}} + \Delta v_l) + (N_s^{\mathrm{eq}} + \Delta N_s)(v_s^{\mathrm{eq}} + \Delta v_s) \\
&= (N_l^{\mathrm{eq}} - \Delta N_s)(v_l^{\mathrm{eq}} - v_l^{\mathrm{eq}}\kappa_T^l\Delta P) + (N_s^{\mathrm{eq}} + \Delta N_s)(v_s^{\mathrm{eq}} - v_s^{\mathrm{eq}}\kappa_T^s\Delta P) \\
&\approx N_l^{\mathrm{eq}}v_l^{\mathrm{eq}} - N_l^{\mathrm{eq}}v_l^{\mathrm{eq}}\kappa_T^l\Delta P - \Delta N_s v_l^{\mathrm{eq}} + N_s^{\mathrm{eq}}v_s^{\mathrm{eq}} - N_s^{\mathrm{eq}}v_s^{\mathrm{eq}}\kappa_T^s\Delta P + \Delta N_s v_s^{\mathrm{eq}}.
\end{aligned} \tag{5.4}$$

Note that the first line is equivalent to using the classical definition of a Gibbs dividing surface (see also Ref. [89]). In the first step we have assumed that both phases respond to the pressure change in the same way as bulk phases. The approximation in the second step is to neglect second-order terms. Now with $V = N_l^{\mathrm{eq}} v_l^{\mathrm{eq}} + N_s^{\mathrm{eq}} v_s^{\mathrm{eq}}$ we find

$$\Delta P = -c\Delta N_s = -\frac{v_l^{\mathrm{eq}} - v_s^{\mathrm{eq}}}{N_l^{\mathrm{eq}} v_l^{\mathrm{eq}} \kappa_T^l + N_s^{\mathrm{eq}} v_s^{\mathrm{eq}} \kappa_T^s} \Delta N_s. \tag{5.5}$$

This completes the macroscopic law for the decay of number fluctuations

$$\frac{d\Delta N_s}{dt} = -\frac{k}{k_{\mathrm{B}}T} \frac{(v_l^{\mathrm{eq}} - v_s^{\mathrm{eq}})^2}{N_l^{\mathrm{eq}} v_l^{\mathrm{eq}} \kappa_T^l + N_s^{\mathrm{eq}} v_s^{\mathrm{eq}} \kappa_T^s} \Delta N_s. \tag{5.6}$$

Taking the hypothesis of Onsager [25, 36] that "slow fluctuations at equilibrium on average decay according to macroscopic laws" we find, with Eq. 5.1:

$$\frac{1}{\tau} = \frac{k}{k_{\mathrm{B}}T} \frac{(v_l^{\mathrm{eq}} - v_s^{\mathrm{eq}})^2}{v_s^{\mathrm{eq}} \kappa_T^s N_s^{\mathrm{eq}} + v_l^{\mathrm{eq}} \kappa_T^l N_l^{\mathrm{eq}}}. \tag{5.7}$$

In *Chapter 2* we measured τ in an equilibrium simulation and the kinetic coefficient k derived from it was shown to give good agreement with data from nonequilibrium simulations.

In essence, Eq. 5.5 is just the statement that an instantaneous correlation exists between ΔN_s and ΔP. Thus, assuming instantaneous linear response, we could also have written

$$\Delta P(t) = \frac{\langle \Delta P(0) \Delta N_s(0) \rangle}{\langle \Delta N_s(0) \Delta N_s(0) \rangle} \Delta N_s(t). \tag{5.8}$$

The latter expression has the advantage that all the information in it can be taken from one and the same two-phase simulation. No reference has to be made to separate bulk simulations. In Tables 5.1, 5.2 and 5.3 we have listed the relevant bulk data and the factor of Eq. 5.8. The calculation of the bulk data is described in full detail in the appendix. The agreement of Eqs. 5.5 and 5.8 is very good for both system sizes.

Now we turn to the decay of pressure fluctuations. It is difficult to conceive that an exact *instantaneous* relation exists between pressure fluctuations and number fluctuations. One would rather think that Eq. 5.5 holds true after averaging over fast fluctuations. As a consequence one may not equate the decay times of $\langle \Delta P(t) \Delta P(0) \rangle$ and $\langle \Delta N_s(t) \Delta N_s(0) \rangle$. To investigate this point, we write the pressure fluctuation at time t as an instantaneous response to the number fluctuation $\Delta N_s(t)$ (with for the moment an unknown proportionality constant $-c$) plus a random component $\xi(t)$:

$$\Delta P(t) = -c\Delta N_s(t) + \xi(t). \tag{5.9}$$

Multiplying on both sides with $\Delta P(0)$ and taking the ensemble average gives

$$\begin{aligned} &\langle \Delta P(t) \Delta P(0) \rangle \\ &\quad = \quad c^2 \langle \Delta N_s(t) \Delta N_s(0) \rangle - c \langle \Delta N_s(t) \xi(0) \rangle - c \langle \xi(t) \Delta N_s(0) \rangle + \langle \xi(t) \xi(0) \rangle \\ &\quad = \quad c^2 \langle \Delta N_s(t) \Delta N_s(0) \rangle - c \langle \Delta N_s(t) \Delta P(0) \rangle - c \langle \Delta P(t) \Delta N_s(0) \rangle \end{aligned}$$

$X^{\rm fit}(T)$	$X^{\rm fit}(T^{\rm eq})$	$X^{\rm EoS}(T^{\rm eq})$
$v^s = 1.0513 - .34068 \times T + .46830 \times T^2$	1.0414	1.0419
$v^l = 1.0312 - .15802 \times T + .53748 \times T^2$	1.1823	1.1842
$h^s = -7.6916 - .11602 \times T + 3.2364 \times T^2$	-6.199	-6.195
$h^l = -8.313 + 3.953 \times T + 0.9729 \times T^2$	-5.084	-5.047
$c_v^s = 1.132 + 4.559 \times T - 3.2554 \times T^2$	2.728	2.751
$c_v^l = 3.1172 + .75039 \times T - 2.0286 \times T^2$	2.654	1.398
$\gamma_V^s = -1.5643 + 27.041 \times T - 20.177 \times T^2$	7.481	7.665
$\gamma_V^l = 11.739 - 2.1269 \times T - 7.8532 \times T^2$	6.439	5.714
$\kappa_T^s = .53244 - 1.5627 \times T + 1.2256 \times T^2$	.03867	.03989
$\kappa_T^l = -.031853 + .076666 \times T + .11392 \times T^2$	.07697	.07664
$\alpha_P^s = .26616 - .55169 \times T + .85314 \times T^2$	.2962	.3058
$\alpha_P^l = -2.1881 + 7.1913 \times T - 4.7838 \times T^2$	.5003	.4380
$\kappa_S^s = \{1/\kappa_T^s + (\gamma_V^s)^2/c_V^s \times vT\}^{-1}$	.02454	.02464
$\kappa_S^l = \{1/\kappa_T^l + (\gamma_V^l)^2/c_V^l \times vT\}^{-1}$	.03866	.03093

Table 5.1: Thermodynamic data for the bulk Lennard-Jones crystal and liquid. Fits are given for the temperature dependence at constant pressure ($P = 2.512 \times 10^{-3}\ \varepsilon/\sigma^3$). See the appendix for computational details. Values at $T^{\rm eq} = 0.6972\ \varepsilon/k_{\rm B}$ are shown in the second column, and in the last column comparison is made with the thermodynamic data of Johnson [100] and van der Hoef [85].

$$
\begin{aligned}
& + \langle \xi(t)\xi(0)\rangle + c\langle(\Delta P(t) - \xi(t))\Delta N_s(0)\rangle + c\langle \Delta N_s(t)(\Delta P(0) - \xi(0))\rangle \\
= \quad & -c\,\langle \Delta N_s(t)\Delta P(0)\rangle - c\,\langle \Delta P(t)\Delta N_s(0)\rangle - c^2\,\langle \Delta N_s(t)\Delta N_s(0)\rangle + \langle \xi(t)\xi(0)\rangle \\
= \quad & -2c\,\langle \Delta P(t)\Delta N_s(0)\rangle - c^2\,\langle \Delta N_s(t)\Delta N_s(0)\rangle + \langle \xi(t)\xi(0)\rangle\,, \qquad (5.10)
\end{aligned}
$$

where in the second step we have substituted Eq. 5.9. The final step was made on the basis of time symmetry. The accuracy of equating $\langle \Delta P(t)\Delta N_s(0)\rangle$ with $\langle \Delta N_s(t)\Delta P(0)\rangle$ was checked in our simulations and was shown to hold perfectly.

Given the correspondence of Eqs. 5.5 and 5.8 that we found above, the best estimate of c would be

$$
c = -\frac{\langle \Delta P(0)\Delta N_s(0)\rangle}{\langle \Delta N_s(0)\Delta N_s(0)\rangle}. \qquad (5.11)
$$

In Fig. 5.1 we plotted the various contributions to the pressure fluctuation autocorrelation function, with the above estimated value of c substituted. Clearly, the agreement of the lower two lines is almost perfect. We found that any other value of c gave worse agreement. It is also seen that there is a non-negligible difference between the decay of $\langle \Delta N_s(t)\Delta N_s(0)\rangle$ and $\langle \Delta P(t)\Delta P(0)\rangle$, so that it is not possible to perform an accurate calculation of the kinetic

	(1)	(2)	(3)	(4)
N_s	1764.38	1794.81	1784.39	1776.84
N_l	2283.62	2253.19	2263.61	2271.16
c (Eq. 5.5)	.00050526	.00050807	.00050711	.00050641
c (subst. κ_S for κ_T)	.00094267	.00094655	.00094522	.00094425
$\langle \Delta P \Delta P \rangle$	.0066787	.0065477	.0063718	.0063196
$\langle \Delta N_s \Delta N_s \rangle$	8391.6	8187.1	7006.3	7234.5
$\langle \Delta P \Delta N_s \rangle$	-4.8498	-4.6732	-4.1939	-4.4266
$-\langle \Delta P \Delta N_s \rangle / \langle \Delta N_s \Delta N_s \rangle$	.00057794	.00057080	.00059859	.00061187

Table 5.2: Results from the fluctuations of N_s and P at equilibrium (NVT) for the small system (4048 particles). The columns show the results after 20,000,000 timesteps of experiments with four different starting configurations.

	(1)	(2)	(3)	(4)
N_s	3579.47	3576.11	3652.22	3597.42
N_l	4516.53	4519.89	4443.78	4498.58
c (Eq. 5.5)	.00025380	.00025372	.00025550	.00025422
c (subst. κ_S for κ_T)	.00047295	.00047284	.00047529	.00047353
$\langle \Delta P \Delta P \rangle$	.0030865	.0029436	.0031182	.0028032
$\langle \Delta N_s \Delta N_s \rangle$	13108	12292	13693	10381
$\langle \Delta P \Delta N_s \rangle$	-3.8981	-3.5878	-4.0642	-2.9783
$-\langle \Delta P \Delta N_s \rangle / \langle \Delta N_s \Delta N_s \rangle$	.00029738	.00029188	.00029681	.00028690

Table 5.3: Results from the fluctuations of N_s and P at equilibrium (NVT) for the intermediate size system (8096 particles). The columns show the results after 10,000,000 timesteps of experiments with four different starting configurations.

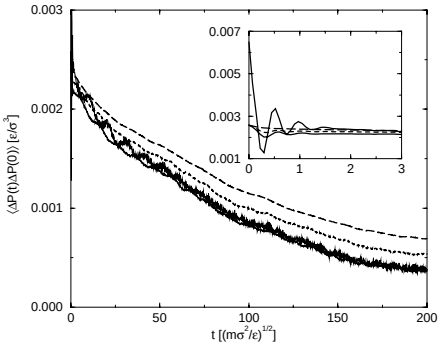

Figure 5.1: Autocorrelation of pressure fluctuations in the small simulation box (4048 atoms). Shown are various terms of Eq. 5.10: $c^2\langle\Delta N_s(t)\Delta N_s(0)\rangle$ (dashed line), $-c\langle\Delta P(t)\Delta N_s(0)\rangle$ (dotted line), $\langle\Delta P(t)\Delta P(0)\rangle$ (bumpy line), and $-2c\langle\Delta P(t)\Delta N_s(0)\rangle - c^2\langle\Delta N_s(t)\Delta N_s(0)\rangle$.

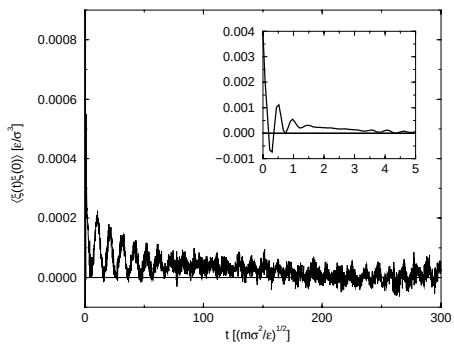

Figure 5.2: Autocorrelation of the random component ξ of the pressure fluctuations in the small simulation box (4048 atoms), taken from Eq. 5.10.

coefficient by using the pressure fluctuations alone. This shows the merits of our solid-liquid discriminator which makes the counting of solid particles possible.

In Fig. 5.2 we plotted the function $\langle\xi(t)\xi(0)\rangle$. It drops rapidly to very small values, which is not surprising since one expects that the major contribution to ΔP at long times would come from ΔN_s. The function remains fluctuating, however, over a long range of correlation times, much longer than the pressure autocorrelation function in bulk simulations. This is indicative of the fact that ξ does not represent the autonomous pressure fluctuations such as they would occur in a bulk system, but should merely be interpreted as the deviation from an exact instantaneous correlation of ΔP and ΔN_s.

We once more turn to the agreement between Eq. 5.5 and 5.8. One might argue that, although the overall system is thermostatted, local fluctuations can have a distribution different from the canonical one. For instance, if local pressure fluctuations are so fast that no energy transfer is possible, the local subsystem behaves adiabatically and the relation between ΔP and Δv would be given by the isentropic compressibility κ_S instead of the isothermal one. For comparison, the factor c of Eq. 5.5 is also given in Tables 5.2 and 5.3 with κ_S substituted for κ_T. Clearly, the κ_T expression behaves much better. From this we conclude that at the interface, temperature fluctuations are canonical. This conclusion is justified, since we are not looking at the time decay here, but only at the average response of ΔP to ΔN_s.

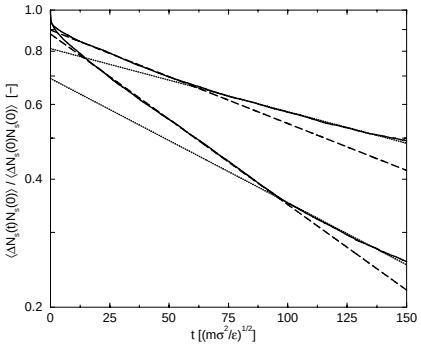

Figure 5.3: Fluctuation autocorrelation functions of the number of solid particles averaged over 4 simulations with 4048 atoms (bottom line) and over 4 simulations with 8096 atoms (top line). Also shown are the fits to the initial regimes (dashed lines) and the long-time regimes (dotted lines).

5.4 Comparison of equilibrium and nonequilibrium results

Normalized autocorrelation functions of the number fluctuations (Eq. 5.1) were averaged over the four independent experiments (for each box size). The result is displayed in Fig. 5.3. Clearly, two regimes can be distinguished. To investigate if these regimes can be associated with the regimes of interface relaxation and macroscopic growth — such as they were found in the nonequilibrium simulations —, we fitted them to single-exponential functions. Note that the crossover time from the initial to the second regimes is smaller for the intermediate box than for the small box, in accordance with the findings of *Chapter 4*. From the relaxation times we calculated kinetic coefficients via Eq. 5.7, once as it is printed, and once with coefficient c according to Eq. 5.11. The results are shown in Table 5.4, together with the linear coefficients from the fits of Eqs. 4.7 and 4.8. There is some statistical scatter in the data, but the trends for both box sizes are the same.

In Fig. 5.4, we have plotted the interface relaxation rates as found from the nonequilibrium simulations together with the predicted curves from Table 5.4. Within the statistical accuracy, the results lie between the linear component of the relaxation rates and the full curve. We conclude that the fluctuations of the interface are such that a substantial part of the *non*linear response is probed by the system. From the figure, it can be roughly estimated that the chemical potential differences associated with fluctuations are equivalent to undercoolings and superheatings of maximum $\pm 0.03\,\varepsilon/k_B$. It can also be seen that they do not depend too much on system size. We will come back to this in the next section (Fig. 5.6).

In Fig. 5.5, we have plotted the results for the second regime, both from equilibruim and nonequilibrium simulations. The results of both box sizes correspond very well with each other and agree well with the nonequilibrium line. From an analysis of the results for different stages of the run, we found that the statistical uncertainty in the slopes presented in Table 5.4 is of the same order as the difference between the two expressions used. Given the present statistical accuracy, we cannot draw further conclusions as to the validity of Eq. 5.11.

	Interface relaxation	Macroscopic growth
Small system		
τ	108.14	148.70
k (Eq. 5.7)	90.304	65.672
k (Eqs. 5.7 + 5.11)	77.582	56.420
$dR/d(\Delta T)$ (Eq. 5.7)	-207.14	-150.64
$dR/d(\Delta T)$ (Eqs. 5.7 + 5.11)	-177.96	-129.42
Intermediate system		
τ	197.27	292.63
k (Eq. 5.7)	98.631	66.491
k (Eqs. 5.7 + 5.11)	85.537	57.664
$dR/d(\Delta T)$ (Eq. 5.7)	-226.24	-152.52
$dR/d(\Delta T)$ (Eqs. 5.7 + 5.11)	-196.21	-132.27
Nonequilibrium results (Eqs. 4.7 and 4.8)		
$(dR/d(\Delta T))^{\mathrm{eq}}$	-184.19	-142.07

Table 5.4: Relaxation times τ and their associated kinetic coefficients as measured from Fig. 5.3 and Tables 5.2 and 5.3. For the small system τ was calculated from fit regions of 10-90 and 90-150 $(m\sigma^2/\varepsilon)^{1/2}$, and for the intermediate system from fit regions of 15-60 and 60-150 $(m\sigma^2/\varepsilon)^{1/2}$, respectively.

5.5 The equilibrium interface

In this section we will take a closer look at the nature of the interface fluctuations at equilibrium. It is generally known that the Lennard-Jones FCC (100) crystal-melt interface is very diffuse and extends over several interlayer spacings [32, 89]. The melting temperature lies well above the thermodynamic roughening transition, which means that growth can occur everywhere on the surface without two-dimensional nucleation barriers. Furthermore, for the FCC (100) surface, all growth sites are equivalent (in contradiction to for instance the (111) surface).

In Fig. 5.6, we have plotted the distribution of the number of solid particles N_s. The distribution is very smooth with no indication of any 'preferred' numbers. This may serve as evidence that the interface is perfectly rough. Would it have been only slightly faceted, then certain numbers would have shown peaks in the distribution. (Note that the surfaces in both systems contain 50 atoms, so the distribution of N_s represents growth and melting over several layers.) The distribution of N is broader in the intermediate box than in the small box. This is to be expected, since the larger bulk phases in the intermediate box can more easily relax local pressure fluctuations and thus give more ease to fluctuations of the interface. As a consequence, the broadness of any time-averaged interface profile would depend on

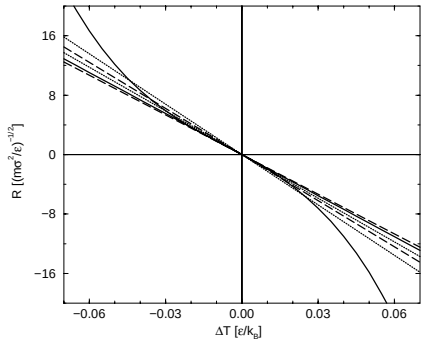

Figure 5.4: Interface relaxation rates vs. temperature. The curved solid line shows the fit of Eq. 4.8, the straight solid line shows its linear component. The other lines show equilibrium results for the small box (dashed) and the intermediate box (dotted). For both boxes, the lines with the largest slopes refer to Eq. 5.7, the others to Eqs. 5.7 + 5.11.

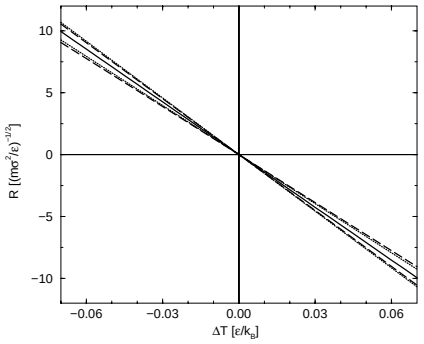

Figure 5.5: Crystal growth and melting rates vs. temperature. The solid line shows the fit of Eq. 4.7. The other lines show equilibrium results for the small box (dashed) and the intermediate box (dotted). For both boxes, the lines with the largest slopes refer to Eq. 5.7, the others to Eqs. 5.7 + 5.11.

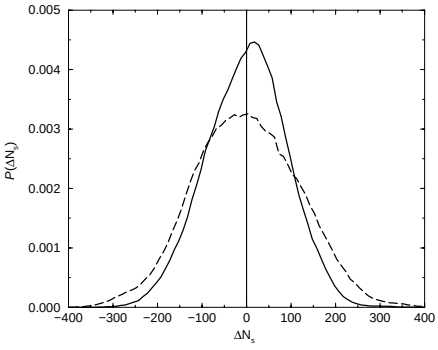

Figure 5.6: Equilibrium distributions of the number of solid particles in the small box (solid line) and the intermediate box (dashed line).

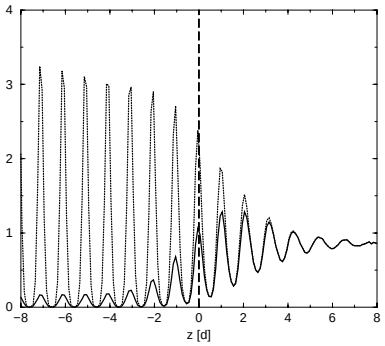

Figure 5.7: Time-averaged profiles of the density and the order parameter for the small box, calculated over 1,000,000 timesteps.

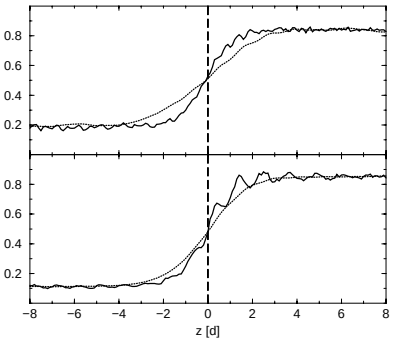

Figure 5.8: Time-averaged (dotted lines) and instantaneous (solid lines) interface profiles for the small box (bottom half) and the intermediate box (top half).

the overall size of the system, while the local instantaneous interface profile would hardly be affected. The fact that the macroscopic growth rates we found in Fig. 5.5 are almost independent of system size is a good indication of this point.

In Fig. 5.7 we have plotted the time-averaged equilibrium profile (over 1,000,000 timesteps) of one interface. Shown are both the density profile and the order parameter profile which is defined (for each histogram bin z_i with a width Δ) as

$$\Phi(z_i) = \frac{1}{A}\left\langle \sum_{k=1}^{N} \Theta(\Psi_k - 0.5)\delta(z_i - z_k) \right\rangle, \tag{5.12}$$

with Θ the unit step function, A the cross-sectional area, and δ the discretized delta function, i.e., $\delta(x) = 1/\Delta$ for $0 < x < \Delta$ and zero otherwise. The order parameter profile represents the counting of liquid-like particles in each bin (cf. the BT-profile in Ref. [97], which is essentially the same, but divided by ρ). The order profile coincides with the density of the liquid at the bulk liquid side and would give zero at an ideal crystal side (the little bumps in the crystalline region represent the average amount of imperfections). The order parameter in conjunction with the density profile provides a much more revealing representation of the equilibrium interface than the density alone. We have used the interlayer spacing d as unit on the z-axis. It can nicely be seen that, on going from the crystal to the liquid phase, the interlayer spacings gradually grow larger, in good accordance with the results of others [32, 89].

To investigate the instantaneous structure of the interface, we took 5 representative stages in the long (20,000,000 timesteps) run of the small box. At each stage, we performed a simulation of 100,000 timesteps and wrote 10 subsequent configurations (one timestep apart) once every 200 timesteps. To obtain sufficient accuracy, the atomic positions of the 10 con-

figurations were averaged and profiles were calculated. We conjecture that these averaged positions are still representative of the instantaneous interface. The profiles were smoothed with a Gaussian filter as follows (see also Hayward and Haymet [82]):

$$\Phi'(z) = \int_{-n}^{n} dz' w(z-z')\Phi(z'), \tag{5.13}$$

with

$$w(z-z') = \frac{1}{\sigma\sqrt{2\pi}} \exp\left(-\frac{1}{2\sigma^2}(z-z')^2\right), \tag{5.14}$$

where we took the interlayer spacing d as width σ of the Gaussian. The smoothed Φ-profiles were then fitted to a tanh funcion:

$$\Phi^{\text{fit}}(z) = \phi_l[1-f(z)] + f(z)\phi_s, \tag{5.15}$$

with

$$f(z) = \frac{1}{2}\left[1 - \tanh\left(\frac{z-z_0}{w}\right)\right]. \tag{5.16}$$

For each 10-step-averaged frame, the position z_0 of the right-hand interface was taken to be the new origin. Profiles (of the right-hand interface) were then constructed on the basis of the atomic positions with respect to this origin. The thus found instantaneous interface profile is plotted in the bottom half of Fig. 5.8 (solid line). The solid line thus represents the *instantaneous* interface profile, as all interface positions z_0 were put on top of each other. We also calculated the *time-averaged* profile, i.e., the distribution of the order parameter with respect to the center of mass of the crystal. This profile was then shifted to have its inflexion point at the origin and drawn as the dotted line in Fig. 5.8. It is shown that the width of the instantaneous interface is smaller than the one of the time-averaged interface. We repeated the procedure for the intermediate box size (now with 4 runs of 100,000 timesteps), the results of which are shown in the top half of the same figure. The time-averaged profile of the larger box is broader than that of the smaller box (in accordance with the findings of Fig. 5.5), whereas the widths of the instantaneous profiles are hardly affected by the overall box size.

5.6 Conclusions and discussion

We have investigated the performance of a previously introduced method (*Chapter 2*) to extract the kinetic coefficient for crystal growth from fluctuations in an equilibrium simulation. We applied the method to the same two system sizes that we used in an earlier nonequilibrium study (*Chapter 4*). We showed that the two regimes that were found previously (an initial regime of interface relaxation and a long-time regime of macroscopic growth) were consistently reproduced by the equilibrium method. This also implies that the same amount of caution must be exercised in calculating growth kinetics from equilibrium simulations as in the nonequilibrium counterpart. In both cases, long runtimes, long observation times, and

large box sizes are needed to avoid the confusion of growth rates with interface relaxation rates.

We found that the crossover time between the initial regime and the long-time regime becomes smaller when the size of the system is increased, again in accordance with the nonequilibrium study. This raises the question whether the initial regime would disappear completely in the limit of infinite system size. We interpreted the initial regime to be associated with a relaxation of the equilibrium interface shape to the shape that corresponds to the (nonequilibrium) circumstances of the experiment. If this interpretation is correct, it seems reasonable to conjecture that there must be a size limit where the crossover time levels off, which means that the initial regime should not disappear completely. It would be interesting to further investigate this.

We slightly modified the equilibrium method to incorporate only properties that can directly be evaluated from the two-phase simulation, whereas the earlier approach required external input from separate bulk simulations. Within the statistical accuracy, it was shown that both approaches agree well, although we could not conclude which one of them gives the most reliable results.

With the modification of the method, we found that, on average, a close correlation exists between pressure fluctuations and fluctuations of the amount of crystalline material. We studied the decay of the autocorrelation function of pressure fluctuations and found that, because the above-mentioned correlation is not instantaneous, this cannot be equated to the decay of the autocorrelation function of number fluctuations. The number fluctuations of solid particles $\langle \Delta N_s(t) \Delta N_s(0) \rangle$ provide the most direct route to calculate k from equilibrium simulations.

Finally, we studied the density and order parameter profiles of the equilibrium interface. A clear distinction could be made between the time-averaged overall profile and the average instantaneous profile of the interface, the latter being noticeably smaller. This is of major importance in for example classical Density Functional Theory (DFT) where averaged profiles are mostly used to calculate both energy and entropy contributions to the free energy of the system, whereas it seems reasonable that for energetic considerations the instantaneous profile should be used.

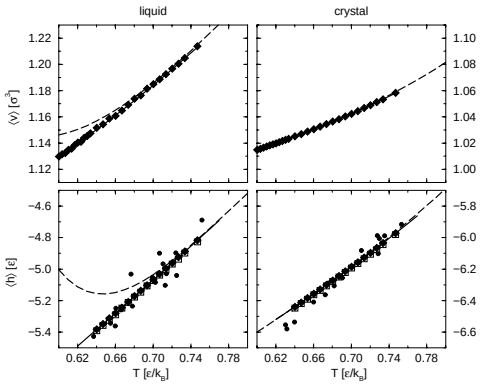

Figure 5.9: Enthalpies and volumes per atom vs. temperature, as measured from 4,950,000 production steps in a bulk liquid (512 atoms) and a bulk crystal (500 atoms) in different ensembles: NPT (filled diamonds), NVT (open squares), and NVE (filled circles). The solid lines represent our fits over the measurement domain (see also Table 5.1). The dotted lines represent the expressions of Johnson (liquid) and van der Hoef (crystal).

5.A Appendix. Bulk thermodynamic properties of the Lennard-Jones crystal and liquid

In this appendix, we will describe how we derived the bulk thermodynamic properties for the Lennard-Jones liquid and FCC crystal as shown in Table 5.1. Most of these could also have been derived from collections (and fits) of thermodynamic data on the Lennard-Jones system by others, the two most recent ones being the Johnson expression [100] (for the liquid) and the van der Hoef expression [85] (for the crystal). The use of these data, however, requires some caution. They represent fits over a limited range of state points and one has to be careful that all state points that one wants to use are covered by the expression. In the following, we will compare our own results with both expressions from the literature.

The procedures for both phases were exactly the same. All liquid calculations were done on a system of 512 particles and all crystal simulations on a system of 500 particles. We used cubic boxes with periodic boundaries. All simulations were run for 5,000,000 timesteps of which 50,000 timesteps were regarded as equilibration and thus disregarded in the evaluations. Nosé-Hoover dynamics were applied with a timestep of $7.480 \times 10^{-4}\sqrt{m\sigma^2/\varepsilon}$ and relaxation times $\tau_T = 0.0748\sqrt{m\sigma^2/\varepsilon}$ (for thermostatted simulations) and $\tau_P = 0.748\sqrt{m\sigma^2/\varepsilon}$ (for barostatted simulations).

To obtain the appropriate densities, we started out with NPT simulations at a range of temperatures and at the desired pressure. The average particle volumes are plotted in the top half of Fig. 5.9. In all figures, the solid lines represent our fits through the data (see also Table 5.1) and the dashed lines represent the expressions of Johnson and van der Hoef. It is clear that the van der Hoef expression describes our results well over the entire range of temperatures. The Johnson expression starts to deviate for lower temperatures. This is not surprising since at that point we enter the metastable liquid region, which is not covered by the data used by Johnson *et al.* Their fit region ranged from $T = 0.7$ to $T = 2.0$. Our figure clearly shows the danger of extrapolating fitted results out of the fitted region (which becomes even more apparent in the thermodynamic response functions in subsequent figures).

Over the entire temperature range, we subsequently performed NVT and NVE simula-

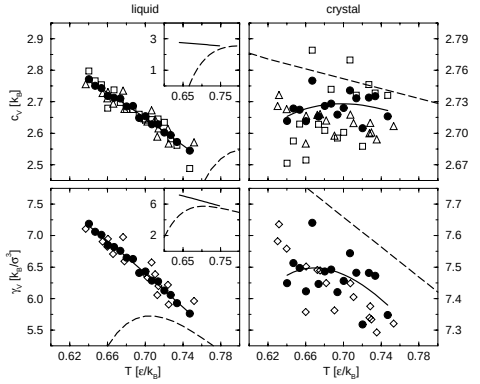

Figure 5.10: Isochoric heat capacity and thermal pressure coefficient vs. temperature in a bulk liquid and a bulk crystal. Symbols denote results from Eqs. 5.A.2 (filled circles, solid line shows fit), 5.A.1 (open squares), 5.A.3 (open triangles), 5.A.4 (filled circles, solid lines show fits), and 5.A.5 (open diamonds). Dashed lines represent the expressions of Johnson (liquid) and van der Hoef (crystal).

tions, at the densities that we found with the NPT simulations. In all ensembles, we calculated the average enthalpy per particle h, the results of which are shown in the bottom half of Fig. 5.9.

For calculating the thermodynamic response functions, we evaluated the average fluctuations of several quantities in our simulations. For a detailed discussion of the use of fluctuation formulas to this end, the reader is referred to the literature [4, 5, 72]. The isochoric heat capacity per atom ($c_V = N^{-1}(\partial U/\partial T)_V$) was calculated from the fluctuations of the total energy and of the potential energy, both in the NVT ensemble, and from the fluctuations of the kinetic energy in the NVE ensemble:

$$\langle \Delta U \Delta U \rangle_{NVT} = k_B T^2 N c_V \tag{5.A.1}$$

$$\langle \Delta \Phi \Delta \Phi \rangle_{NVT} = k_B T^2 (N c_V - \frac{3}{2} N k_B) \tag{5.A.2}$$

$$\langle \Delta \hat{T} \Delta \hat{T} \rangle_{NVE} = \frac{3}{2} N k_B^2 T^2 \left(1 - \frac{3 N k_B}{2 N c_V}\right) \tag{5.A.3}$$

The results are shown in Fig. 5.10. Clearly, Eq. 5.A.2 gives the best statistics, so that data were used for the fit.

The thermal pressure coefficient ($\gamma_V = (\partial P/\partial T)_V$) was calculated from:

$$\langle \Delta \Phi \Delta \hat{P} \rangle_{NVT} = k_B^2 T^2 (\gamma_V - \rho k_B) \tag{5.A.4}$$

$$\langle \Delta \hat{P} \Delta \Phi \rangle_{NVE} = \frac{N k_B^2 T^2}{V} \left(1 - \frac{3 V \gamma_V}{2 N c_V}\right), \tag{5.A.5}$$

the results of which are also plotted in Fig. 5.10. Given the small variations of both c_V and γ_V for the crystal over this temperature range (see the scale in the figures), the van der Hoef expression gives satisfactory results. The Johnson expression seems to be way off for both properties, but the insets in the figures show that the data converge to the expression just above $T = 0.7$.

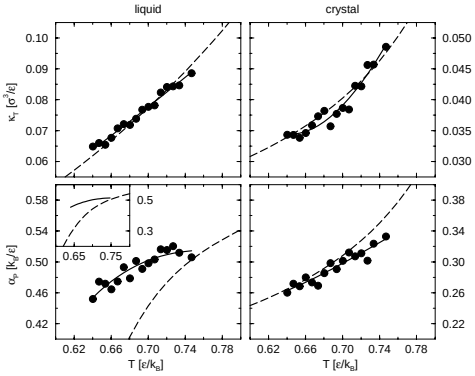

Figure 5.11: Isothermal compressibility and thermal expansion coefficient vs. temperature in a bulk liquid and a bulk crystal. Symbols denote results from Eqs. 5.A.4 (filled circles, solid lines show fits), 5.A.5 (open diamonds), and 5.A.7 (filled circles, solid line shows fit). Dashed lines represent the expressions of Johnson (liquid) and van der Hoef (crystal).

Finally, the isothermal compressibility ($\kappa_T = -V^{-1}(\partial V/\partial P)_T$) and the thermal expansion coefficient ($\alpha_P = V^{-1}(\partial V/\partial T)_P$) were calculated with

$$\langle \Delta V \Delta V \rangle_{NPT} = V k_B T \kappa_T \tag{5.A.6}$$

and

$$\left\langle \Delta V \Delta (U + \hat{P}V) \right\rangle_{NPT} = k_B T^2 V \alpha_P. \tag{5.A.7}$$

Results for the latter two properties are shown in Fig. 5.11.

Adams [1] has emphasized that when fluctuation formulas such as the above are used in a computer simulation, it is advisable to cross-check them with the thermodynamic identity $\alpha_P = \kappa_T \gamma_V$. A quick check with the equilibrium values in Table 5.1 shows that the agreement is good.

Part III

Self and transport diffusion in unidirectional zeolites

6 Diffusion in zeolites: a historical perspective

In this chapter, a brief overview will be given of the development of zeolite science and technology, from the early discovery of the mineral in the 18th century to present-day applications. We will start with the ancient mineralogical studies, followed by the development of industrial synthesis routes and commercial applications. In the third section, we will focus on the scientific understanding of transport of guest molecules in zeolitic channels, both from theory and experiment. Finally, we will present an outline of the chapters to follow.

6.1 Those boiling stones

Son of a renowned army officer, the Swede Axel Fredrik Cronstedt (1722-1765) was destined to follow in his father's footsteps. For a sound preparatory education, he was sent to study mathematics at the university of Uppsala. But when he once found himself in the audience of Valerius' lectures on mineralogy, he could not think of anything else anymore and his studies went off in a new direction. By the year 1742, he had mastered most of the mineralogy courses and entered the college of rock science as a student teacher. During subsequent years he undertook many field trips into the local mountains, both on his own and accompanied by the famous scientists of his time. Soon he received widespread fame for his creativity and original scientific methods. He was among the first to stress the importance of the chemical constituents of minerals. In 1751, he isolated a new element from the mineral niccolite and named it 'Nickel'. For this achievement he was admitted to the 'Vetenskapsakademien' (scientific academy) in 1753.

Cronstedt became also known for his introduction of the blowpipe in mineralogy. This was a long, narrowing tube which, when blown into at the wide end, produced a concentrated jet of air at the narrow end. This jet, directed into a flame, was used to locally heat the mineral to very high temperatures. Information concerning the nature and composition of the mineral could then be gathered from the colour of the flame, the nature of the vapours formed, the oxides or metallic substances left behind, and so on. The blowpipe remained a key tool in chemical analysis and has been used in university courses of mineralogy far into the 20th century. So much knowledge was gained by the chemical analysis that Cronstedt felt justified

in suggesting that minerals be classified according to their chemical structure instead of their appearance (such as outer shape and physical properties). Well aware of the revolutionary character of this idea, he published his new scheme anonymously in 1758 [42]. Nevertheless, it was a great success and the book was translated into Danish, English, German and French.

Two years earlier, his blowpipe had led him to yet another discovery when he used it on the mineral stilbite. He observed that this mineral released excessive amounts of steam upon heating. Intrigued by this peculiar behaviour, he named the material 'zeolite' [41] after the Greek words ζέω (to boil) and λίθος (stone, rock, cf. 'lithography'). Soon he identified zeolites as a new class of minerals and found that they were hydrated aluminosilicates of the alkali and alkaline earths.

After this early observation, several decades passed before the importance of zeolites was recognized outside the field of mineralogy. In 1840, Damour observed that crystals of zeolites could be reversibly hydrated with no apparent change in their transparency or morphology [43]. Shortly thereafter, in 1857, Eichhorn showed the reversibility of ion exchange on zeolite minerals [49]. The first synthesis of a zeolite (levynite) was reported as early as 1862, by de St. Claire-Deville [38]. Friedel in 1896 [62] brought up the picture of a dehydrated zeolite as an open spongy framework after his observation that it absorbs various liquids such as alcohol, benzene, and chloroform. Today, the mineralogist Friedel is best known of his work in organic chemistry (the 'Friedel-Crafts reaction').

All early investigators studied the naturally occurring zeolites chabazite, heulandite and analcite. The dehydrated forms were referred to as 'activated zeolites' since it is only after the removal of the included water that the absorption characteristics appear. Several workers at the end of the 19th century discovered the ability of activated chabazite to remove odours from the air (for which it is still widely used today). Its absorption of ammonia, air, hydrogen, and other molecules was reported by Grandjean (1909) [69]. The first account of its capability of selective absorption appeared in 1925, when Weigel and Steinhoff [185] reported the rapid occlusion of water, methyl alcohol, ethyl alcohol or formic acid, and the simultaneous exclusion of acetone, ether or benzene. This ability to selectively take in molecules into their porous structure, whilst rejecting others on the basis of their molecular dimensions, has given zeolites the name 'molecular sieve', a term introduced by McBain in his review article of 1932 [126]. By that time, the Friedel picture had become firmly established by experiments. This became possible after the invention of X-ray structure determination which had been first applied to zeolites in 1930 by Taylor and Pauling [143, 144, 166].

6.2 The birth of zeolite science and technology

By the mid-1930's, most of the properties of zeolites which today are considered fundamental for their numerous applications (e.g., ion exchange, absorption, molecular sieving) had been described in the literature. Besides their physico-chemical properties, the basics of their structures had also been elucidated. Zeolites were known to be microporous aluminosilicates with a well-defined pore structure of atomic dimensions. Most were found to be thermally stable even after the removal of the 'zeolitic' water. Few accounts of artificial hydrothermal synthesis of zeolites had been reported.

Despite the slow but steady increase of knowledge over the first 180 years, their rarity — they typically occur as minor constituents in cavities in basaltic or volcanic rock — prevented an extensive commercial use of zeolites. The interest of the scientific community, however, was aroused when a man now regarded as the 'founding father' of zeolite science, Richard M. Barrer, started a thorough and systematic study of the sorption of polar and non-polar gases by zeolites. In his 1938 paper [9], he related the sorptive properties to the structural properties known from X-ray measurements. For example, the absorption isotherm of hydrogen in chabazite expressed as $\log x/p$ vs. $\log x$ was found to show an inflexion point. This was interpreted as an indication that not all available sites in the chabazite skeleton were similar, hence the resultant isotherm should be composed of two superposed isotherms. (Note that many decades later, this behaviour was also found in Monte Carlo simulations, for example for the absorption of heptane in silicalite [182]).

Barrer remained active in the field of zeolites during his scientific career until he passed away in 1996. His many papers include not only accounts of absorption and molecular sieving properties, but also many syntheses of zeolitic structures. He was among the first to propose a scheme for naming zeolites (in 1945), but it would last until the 1970's before he laid down a scheme that was adopted as the current IUPAC standard [13]. In 1968, he initiated the annual International Zeolite Conferences, which are still held every 3rd year. In 1975, Passaglia and Pongiluppi named a newly discovered zeolite of the stilbite topology 'Barrerite' [142].

Inspired by the huge potential of zeolites, together with their rare occurence in nature, two researchers at the Linde division of Union Carbide Corporation, Milton and Breck, set out to search for synthetic routes to produce zeolite structures. Between 1949 and 1954, they (internally) reported the synthesis of zeolites A (now known as LTA = 'Linde Type A'), X, and Y, which appeared in the 'open' patent literature around the 1960's [22,129,130]. Milton and Breck found a way to synthesize these materials under mild hydrothermal conditions (i.e., $< 100\,^{\circ}$C and at atmospheric pressure). In fact, their *reactive gel crystallization* method — where Al_2O_3 and SiO_2 are combined with an alkali hydroxide into a reactive gel from which the zeolite is formed — is still the basis for most present-day synthesis routes.

The first commercial zeolites were mainly applied to dry refrigerant gas or natural gas. In 1959, Union Carbide introduced the ISOSIV process for normal-/iso-paraffin separation, and in the same year they developed a zeolite Y-based catalyst for isomerization reactions. Mobil Oil introduced the use of zeolite X as a refinery cracking catalyst in 1962. Easily separable and fully re-usable, zeolites provided a huge potential in clean catalytic processing. Encouraged by the 1963 US Clean Air Act, this resulted in an explosive growth of their use in the oil industry.

Barrer took the next step in zeolite synthesis in 1961 [12] by introducing alkylammonium cations into the reactive gel. With tetramethylammonium (TMA) in sodium aluminosilicate gels, he synthesized N-A, the siliceous analogue of zeolite A. Around the same time, Kerr [109], synthesized the new structures ZK-4 and ZK-5 (ZK = 'Zeolite Kerr') also using organic cations. It was shown that the organic additives formed clusters in the gel that acted as precursors for the final shape of the zeolitic channels. In this way, many new forms could be produced, including zeolites with a higher Si/Al ratio than naturally occurring zeolites. It was soon discovered that zeolite structures with higher Si content were more stable. Also, because Al^{3+} ions at tetrahedrally co-ordinated sites were replaced by Si^{4+}, high silica frameworks

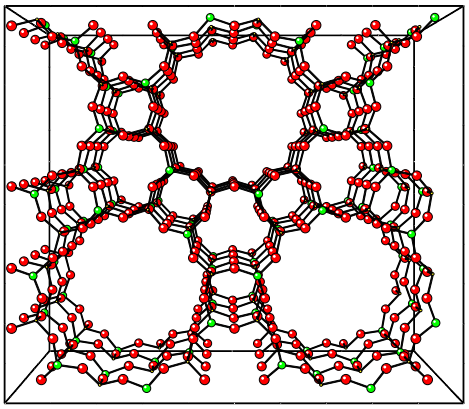

Figure 6.1: $AlPO_4$-5 structure, viewing down the unidirectional pores.

were less charged. This made them less suitable for ion-exchange applications (since there were less counterions present), but all the more suitable for catalyzing reactions that had to take place in an hydrophobic/organophilic environment, such as those in the petrochemical industry. For this reason, all the efforts in zeolitic synthesis were directed towards increasing the Si content, which by the end of the 1960's led to the discovery of high silica zeolites such as Beta [183] and ZSM-5 [6, 113] (ZSM = 'Zeolite Secony Mobil'). The latter provided the perhaps biggest technological innovation when it was discovered that methanol could be converted to gasoline over ZSM-5 [128] in a single step. Up until then, this was done via the Fischer-Tropsch process which produces a wide range of hydrocarbons, necessitating many seperation and upgrading steps to make commercial fuel.

The success of the organic-additive driven synthesis led in the early 1980's to the discovery by Wilson *et al.* [191] of a completely new class of materials, the aluminophosphate molecular sieves. These are made of neutral $AlPO_4$ building blocks and display no ion-exchange properties. On the other hand, they can be made with a wide variety of pore dimensions (ranging from 0.35 to 1.25 nm), both in structural analogues of the aluminosilicate molecular sieves and in new forms. The absence of counterions in the pores and of charges in the lattice makes them less suitable for catalysis, but all the more suitable for molecular sieving since there is no blocking by couterions. One member of the aluminophosphate family is the unidirectional pore structure $AlPO_4$-5 [17, 146] (see Fig. 6.1), which is the object of study in *Chapters 7 – 9*.

Today, zeolites (both synthetic and natural) are used in numerous applications in a wide variety of fields. To name but a few: odour removal from the air, cleaning of nuclear waste (by absorbing heavy atoms), waste water treatment (absorbing ammonia), removal of moisture and odours from cat litter boxes, irrigation in agriculture (taking in water during heavy rains and slowly releasing it during dry periods), water softening in detergents, and many, many more. For a more detailed description of these (and other) fields in zeolite science, the reader is referred to several books [15, 37, 48].

6.3 Diffusion in zeolites

To succesfully apply or, eventually, design a proper shape-selective catalyst or molecular sieve for industrial processing, it is of utmost importance to understand how the channel network influences the movement and/or the reaction pathway of the molecules inside. In an isotropic medium, the driving force for molecular diffusion is the concentration gradient $\partial\rho/\partial z$. (Throughout this study, we will represent concentration by the number density ρ.) The diffusion coefficient D_t is the proportionality constant relating the particle flux to the driving force, as expressed in Fick's first law [56]:

$$J = -D_t \left(\frac{\partial \rho}{\partial z} \right). \tag{6.1}$$

There are several regimes to be identified in the diffusion in porous solids, depending on the (mean) size of the pores. For pores of the order of 1 μm or larger, normal *gaseous diffusion* prevails ($D \sim 10^{-5}$ m^2/s). When the pores become smaller than the mean free path of gas molecules (10^{-7}–10^{-8} m), collisions with the wall occur more frequently than collisions with each other. In the ultimate limit, each molecule diffuses independently with the mean free path determined by the pore diameter. This regime is called *Knudsen diffusion* and the diffusion coefficient only depends on the mean thermal velocity of the molecules and the pore diameter (and is independent of concentration or pressure):

$$D_{\text{Knudsen}} = \frac{1}{3} \left(\frac{3 k_{\text{B}} T}{m} \right)^{1/2} R_{\text{pore}}. \tag{6.2}$$

Diffusion coefficients in this regime typically fall in the range 10^{-5}–10^{-8} m^2/s, which is the prevalent range for most 'macroporous' catalysts. Diffusion coefficients measured in the microporous zeolites, however, span an enormous range from 10^{-8} to less than 10^{-20} m^2/s. The mass transport within the pores of zeolites is influenced by both sorbate-wall interactions and sorbate-sorbate interactions. This regime has been named *configurational diffusion* by Weisz in 1973 [187].

The first theoretical foundations of zeolitic diffusion were presented by Barrer and Jost in 1949 [11]. They were based on classical diffusion theory as expressed by Fick's first law (Eq. 6.1). Assuming the diffusion coefficient is independent of concentration, this law can be transformed into Fick's second law, which gives the change of concentration in a fixed volume element with time. In one dimension:

$$\left(\frac{\partial \rho}{\partial t} \right) = D_t \left(\frac{\partial^2 \rho}{\partial z^2} \right). \tag{6.3}$$

Barrer's group performed many uptake measurements, i.e., experiments in which the time to load the zeolite was measured. With certain assumptions on the pore size, diffusion coefficients could be deduced from the measurements. It appeared that the diffusivities were highly temperature dependent and displayed an Arrhenius behaviour:

$$D_t = A \exp\left(-\frac{E_a}{RT} \right). \tag{6.4}$$

Activation energies E_a ranging from 0.3 to as much as 25 kcal/mole were reported by several authors over the years. Barrer tried to relate the pre-exponential factor to a jumping frequency between adsorption sites. This can be seen as the first account of a hopping picture of diffusion in zeolites, as early as 1941 [10]. It was soon realized, however, that substantial deviations from Eq. 6.3 could be expected since (1) zeolites are generally not isotropic, (2) not all molecules will be equally mobile, and (3) channels may become blocked at high loadings, which would render D_t concentration dependent.

It was argued in the paper of Barrer and Jost that, since diffusion is essentially the macroscopic manifestation of the tendency to approach equilibrium, the true driving force should not be the concentration gradient, but the gradient in the chemical potential μ. In fact, this was first explicitly stated by Einstein [51]. The flux is then expressed as

$$J = -F(\rho)\rho\left(\frac{\partial\mu}{\partial z}\right) = -F(\rho)\rho\left(\frac{\partial\mu}{\partial\rho}\right)\left(\frac{\partial\rho}{\partial z}\right), \tag{6.5}$$

with the relation between D_t and the mobility F given by

$$D_t = F\rho\left(\frac{\partial\mu}{\partial\rho}\right). \tag{6.6}$$

Assuming the absorbens inside the pore is in equilibrium with the gas outside the pore, this leads to

$$D_t = F\rho k_B T\left(\frac{\partial\ln f}{\partial\rho}\right) = Fk_B T\left(\frac{\partial\ln f}{\partial\ln\rho}\right) = D_0\left(\frac{\partial\ln f}{\partial\ln\rho}\right), \tag{6.7}$$

with f the activity of the gas ($= p$ in the case of an ideal gas) and D_0 the so-called *corrected diffusivity*. The above relation between D_t and D_0 is usually called the Darken equation [44]. (Note that it is the corrected diffusivity that also appears as the Maxwell-Stefan diffusivity in the Maxwell-Stefan formalism for multicomponent diffusion [125, 163]).

Transient uptake measurements remained the main method of measuring diffusion coefficients in zeolites for many decades. One of the groups that contributed most to this field is the group of Ruthven in Canada [151]. The measured diffusivity D_t is also called the *transport diffusivity*, i.e., the transport coefficient as measured in the presence of a macroscopic gradient. This is to be distinguished from the tracer or *self-diffusion coefficient* which describes the motion of a tagged particle in equilibrium with like particles. The latter is given by for instance the Einstein equation, which reads (in one dimension):

$$\left\langle z^2\right\rangle = 2D_s t. \tag{6.8}$$

It was argued that in the limit of infinite dilution, where no correlations exist between adsorbed particles, D_0 should become equal to D_s. Hence (at low loadings, via the Darken equation), the uptake experiments could be used to measure both D_t and D_s.

Some controversy remained, however. In 1967, Weisz and Zollinger [186] suggested that in the presence of strong adsorption sites, part of the molecules could become immobile, thus not taking part in the diffusion process. For that reason, the concentration of the mobile species should be taken as the driving force. Their model, however, was derived for macropore systems (the uptake of dye molecules in fibers) and Riekert in 1971 [147] argued that,

because of the small pore diameters in zeolites, the coexistence of a gaslike phase with an immobile phase would be hardly conceivable.

Serious complications arose in the late 1970's when the group of Pfeiffer and Kärger pioneered a new technique and started to measure intracrystalline self-diffusivities by Pulsed Field Gradient (PFG) NMR spectroscopy. In this method a magnetic field gradient is applied, causing the precession of the transverse magnetization of the nuclear spins to depend on their spatial co-ordinates. Two successive gradient pulses are applied of equal magnitude and opposite sign. If particles have not moved in between the pulses, the effect of both pulses is exactly cancelled, but when they have moved the intensity of the transverse magnetization will not be fully restored. From this the self-diffusion of the particles can be derived.

Even after taking into account all the correction factors, large discrepancies were found between the PFG-NMR measurements and the results of Ruthven. In a joint effort lasting many years, the two groups tried to resolve the problems, exchanging zeolite crystals and performing both methods on the same samples. In 1989, Kärger and Ruthven [103] concluded that some of the discrepancies could not be removed and must reflect real intracrystalline phenomena. They added the remark that there is a large difference in timescale of the measurements: PFG-NMR is limited to the order of a few milliseconds, whereas most uptake methods operate on the scale of seconds. The problem of timescales will also be addressed by us in *Chapter 7*.

In their struggles to overcome the discrepancies, Ruthven's group has found several possible problems associated with uptake measurements: (1) there are large gradients involved (beyond the linearity of Fick's law), (2) the methods inherently involve unsteady states, and (3) the experiments are often irreversible. Yasuda introduced the Frequency Response (FR) technique [192–194]. In this method the external pressure is periodically varied, which might more easily eliminate the influence of external resistances. The diffusivity is obtained from the characteristic response curve within the regime of Henry's law. In the late 1980's, Eic and Ruthven introduced the Zero Length Column (ZLC) method. In this method, the zeolite is first equilibrated with the sorbate at a very low external concentration. At time zero the sample is desorbed by a purge gas (Ar or He), and the sorbate concentration in the purge gas is followed chromatographically. By using very high purge rates, the sorbent concentration at the crystal surface is kept close to zero, which eliminates any external mass transfer resistance.

In recent years, several other methods have been introduced, to study both self- and transport diffusion: in Fourier Transform Infrared spectroscopy (FTIR) [137] the increase in IR band intensity is followed in time. In Quasi-Elastic Neutron Scattering (QENS) [34] the hydrogen atoms of the absorbent serve as scattering centers; the magnitude of the Doppler shift of the outgoing wave depends on the mobility of the scattering centers. Just very recently, the QENS technique was used to simultaneously measure self- and transport diffusion, by using both hydrogen and deuterium atoms in the absorbent [99]. For a more detailed description of experimental methods, we refer to the book of Kärger and Ruthven [106] and references therein.

To sum up, several experimental methods exist, each with their own specifics regarding timescales, length scales, and their being equilibrium or nonequilibrium methods. Some of the differences between the results can be attributed to these specifics, while others are due

to deviations from the Darken equation, or even anomalous diffusion.

It seems only natural with the advent of molecular dynamics simulations and stochastic simulations, that several attempts have been made to reproduce the results of one or more experimental measurements. Being computationally much simpler, most simulations have thus far been aimed at self-diffusion (Eq. 6.8) and not at transport diffusion. At this point we mention one particular example where simulations have been of great help in understanding experiments: the case of single-file diffusion. When pore sizes are such that molecules cannot pass each other in the pores, the Einstein equation does not hold anymore. Instead, the mean square displacement scales with the square root of time. This effect has been found both by theory [104] and experiment [115]. In an extensive simulation study of the influence of system sizes and boundary conditions, Hahn and Kärger [75] could predict the conditions at which the anomalous behaviour should be found.

The first calculation of transport diffusion by molecular dynamics simulations was done by Maginn *et al.* [123]. They mimicked the experimental nonequilibrium situation in several ways in their simulation system.

Space it too limited here to mention all the topics where molecular simulations have contributed to the understanding of transport phenomena in zeolites. For an excellent review, the reader is referred to Keil *et al.* [108].

6.4 Outline of subsequent chapters

In the following three chapters our object of study will be the aluminophosphate $AlPO_4$-5. This pore system provides a suitable model system to study configurational diffusion in zeolitic channels for several reasons. First, it consists of unidirectional, non-interconnected pores. This way, we can focus on the movement in single channels, without complications by the interplay of diffusion in different (mostly anisotropic) directions. Second, the aluminophosphate zeolites have neutral lattices. This is advantageous in simulations as one does not have to calculate the Coulombic interactions which scale with $1/r$ and thus have a much longer range than dispersion interactions (which scale with $1/r^6$). Finally, in neutral zeolite networks there are no counter-ions present, which means that the guest molecules will not be hindered by the presence of other substances.

In *Chapter 7* we will study the self-diffusion of methane in the $AlPO_4$-5 channels. The size of methane molecules is such that two molecules may just about pass each other in the channels. The question whether or not this is possible has enormous implications on the type of diffusion they will display. Nevertheless, experimental investigations on this question give contradictory results [74, 98, 115, 138]. Besides short-timescale molecular dynamics simulations, we will describe the construction of a simple stochastic model simulation, which enables us to go to much larger length and time scales than in molecular dynamics. With this model, we will show that, due to infrequent passings, a normal diffusive regime is found at long times.

In *Chapter 8* we will study the movement of (substantially smaller) argon atoms in the same system. Here we will focus on calculating the transport diffusion coefficient. Others in earlier simulations studies have calculated this quantity by various nonequilibrium methods.

We will extract this nonequilibrium property from density fluctuations in an equilibrium simulation. To do so, we make use of Onsager's regression hypothesis, in the same way as we calculated the kinetic coefficient of crystal growth from equilibrium simulations in *Chapters 2 and 5*. An advantage of the presented equilibrium method is that it provides a direct way to investigate if, and when, the linear response regime is reached. This is because our formula contains an explicit dependence of the diffusion coefficient D_t on the k-value of the probed density wave. In the linear response regime D_t is seen to level off to a plateau value (i.e., D_t becomes independent of k).

Just very recently, some groups have used an Einstein expression to derive the collective diffusion coefficient from nonequilibrium simulations (where we use the Green-Kubo approach). Their representation, however, does not have an explicit k-dependence [153, 154, 161]. In *Chapter 9* we will compare their approach with ours and look at the advantages and disadvantages of both methods.

7 Unidirectional diffusion of methane in $AlPO_4$-5

Tracer diffusion of methane molecules in the unidirectional channels of $AlPO_4$-5 has been studied by means of molecular dynamics simulations. A one-dimensional hop-and-cross model is introduced and shown to be able to reproduce the molecular dynamics results accurately with the profit of an extensive speed-up in computation time. After elimination of system size effects by using the new model, two regimes can be recognized: a short-time regime where the mean square displacement is proportional to $t^{0.6}$, and a long-time regime where the proportionality is linear.[*]

7.1 Introduction

Zeolites and other molecular sieves have found widespread applications in catalysis, ion-exchange and separation technologies. They owe their high (shape-)selective power mainly to their well-defined nanoporous structures, which allow some molecules to pass through the pores and forbid the transport of others. The confinement of a fluid in pores of nanometer scale largely influences its diffusion mechanism, and sometimes leads to deviations from Fickian behaviour. Because of their importance for diffusion-limited catalytic reactions and separation processes, these phenomena have attracted the interest of both experimentalists and theoreticians.

In the case of zeolites with straight non-connected pores, like ZSM-12, $AlPO_4$-5, and VPI-5, diffusion takes place in one single direction. If moreover the diffusing molecules are of such dimensions that they cannot pass each other in the channels, the diffusion becomes of single-file type. The time dependence of the mean square displacement can be written in the following general form:

$$\langle z^2 \rangle = 2Ft^{\alpha} \tag{7.1}$$

Whereas in the case of normal diffusion α would be equal to 1 (in which case the factor F would correspond with the tracer diffusion coefficient D), the case of single file diffusion

[*] The work desribed in this chapter previously appeared in J. Chem. Phys. **110**(23), 11514 (1999). [168]

leads to $\alpha = 0.5$. The latter result had already been established theoretically in the late seventies by Fedders *et al.* [54, 55, 155], and has later been derived in alternative ways by, among others, van Beijeren *et al.* [14] and Kärger *et al.* [73, 104]. For methane in $AlPO_4$-5, the typical single-file behaviour has been observed experimentally by PFG-NMR measurements of Kukla *et al.* [74, 115], although this was contradicted by findings of Nivarthi *et al.* [138] (Fourier transform PFG-NMR) and Jobic *et al.* [98] (QENS), both indicating normal diffusion behaviour for this system. The three studies correspond to quite different timescales of observation (Kukla *et al.*: 1-100 milliseconds; Nivarthi *et al.*: 1-6 milliseconds; Jobic *et al.*: several nanoseconds) and moreover they all use $AlPO_4$-5 crystals of different origin (which may mean different crystal size distributions and/or presence of defects). A further discussion on the discrepancies can be found in the paper of Jobic *et al.* and in the final section of this chapter. At this point we can clearly say that current experimental observations are not decisive as to whether the system shows normal or single-file behaviour.

Molecular simulations, enabling the researcher to follow the pathways of individual molecules directly, can provide complementary insights and are often more easy to interpret than experiments. A straightforward way to study tracer diffusion in zeolites is the direct calculation of the mean square displacement from molecular dynamics simulations and investigation of its time dependence (see Eq. 7.1). This, however, is still not without pittfalls. First, just like with experimental methods, there is the matter of time regimes. When molecules are of such size that they cannot pass each other very easily, they will expectedly show a single-file type diffusion on short timescales, but on the longer timescales, infrequent passings will start to dominate the diffusion mechanism and normal diffusion behaviour will prevail. This effect can be totally missed if simulation times are not long enough. Also, when time regimes are not separated well enough, it is possible to find 'transitional' behaviour, as has been shown by Keffer *et al.* [107]. Unfortunately, these authors did not search for a transition to normal diffusion in the long-time limit. Second, system size effects can play an important role. When using periodic boundary conditions, too short a simulation box can level off the mean square displacement curve at large correlation times [75]. (Clearly, for the pure single-file case, when one particle has travelled all the way round, all other particles must have done so as well, which is not possible when the center of mass of the system is kept fixed). In addition, Kärger *et al.* [105] reported for very dense systems a deviation to ordinary diffusion when the box was chosen too small, which is in fact rather unintelligible under the above remarks.

In this chapter, molecular dynamics simulations will be used to calculate mean square displacements of methane molecules in $AlPO_4$-5. Next, a simple hop-and-cross model will be introduced that is able to reproduce the molecular dynamics results quite accurately. The increased computational speed of the simplified model allows us to do an in-depth investigation of system size effects and enables us to make a trustworthy classification of observed regimes. Such a study with the system sizes that we will use would have been impossible if one had had to do the full MD simulations. An additional advantage of the hop-and-cross model is that the dependence of the diffusion behaviour on the two model parameters can be studied easily.

7.2 Molecular dynamics simulations

The zeolite system used in this study is the aluminophosphate $AlPO_4$-5, which consists of a neutral crystal lattice with one-dimensional, non-interconnected pores. Pore cross-sections are nearly circular with minimum window size of ca. 7.3 Å. The unit cell is hexagonal with dimensions $a = 13.7707$ Å and $c = 8.3789$ Å and contains 12 aluminium, 12 phosporous, and 48 oxygen atoms [17, 127, 146]. In the simulations, a rectangular periodic box was used with dimensions $2 \times 2 \times 60$ unit cells. In this box, the *x*-axis runs parallel to the crystal *a*-axis, the *y*-axis makes an angle of 30 degrees with the crystal *b*-axis and the *z*-axis runs parallel to the *c*-axis of the crystal and thus parallel to the pore direction as well. Constructed this way, the simulation box contains four pores of 60 unit cell lengths. The reason we choose for this configuration, as opposed to simulating one pore of quadruple length, is twofold: first, this way we are sure to include interactions between particles in different pores and second, each simulation constitutes an average over four initial configurations (the rather small system with constrained motion might be quite sensitive for initial conditions).

We assumed the zeolite lattice to be rigid and host-guest interactions were evaluated on a grid with cell lengths of 0.2 Å, with cubic interpolation between the grid points. It has been shown previously that this approximation does not influence the diffusion of small particles very much [101], which was confirmed by tests of our own (deviations of energies from simulations without using a grid were less than 1 promille). Since the walls of the pores are formed by 6- and 12-rings of oxygens pointing inwards, and the interactions with the oxygen atoms therefore dominate host-guest interactions, the zeolite was modelled by its oxygen sites only (following the idea of Kiselev *et al.* [110]). The molecular dynamics simulations were done with the GROMOS87 package [19], adapted to our own needs. Among the adaptations are the incorporation of the grid evaluation of the host-guest interactions and a change of the temperature scaling routine, which made it possible to scale the particle velocities in the different pores independently. A timestep of 2 fs was used and temperature scaling was carried out by partial rescaling of the velocities in order to get a smooth relaxation towards the target temperature, with a relaxation time of 0.1 ps. This procedure is also known as the Berendsen thermostat [18]. To prevent accumulation of center of mass movement, this motion was removed once every timestep [120].

7.2.1 Argon adsorption

Before being able to carry out reliable simulations, potential parameters had to be optimized for the system. Since there are good adsorption data for argon in $AlPO_4$-5 available [79], we decided to extract semi-empirical oxygen parameters from these data. The Lennard-Jones parameters for argon we used were $\varepsilon_{Ar} = 0.96605$ kJ/mol and $\sigma_{Ar} = 3.4050$ Å, and the Lorentz-Bertelot mixing rules were applied to determine interactions between particles of different kinds. The Widom particle insertion method [188] was used to calculate the chemical potential of argon in the pores of $AlPO_4$-5 at $T = 87$ K at different loadings. The result was then equated to the chemical potential of the gas outside the pore. Assuming ideal gas behaviour outside the pore, the adsorption isotherm at the above temperature was constructed. The result was compared with the experimental adsorption isotherm of argon in $AlPO_4$-5 [79].

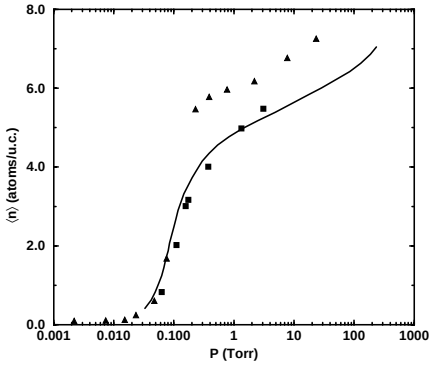

Figure 7.1: Adsorption curves for argon in $AlPO_4$-5; experimental results (Hathaway *et al.* [79], drawn line), MD results (this study, squares), and GCMC results (Boutin *et al.* [21], triangles).

The procedure was repeated for various zeolite oxygen parameters until the closest possible match was obtained. This resulted in $\varepsilon_O = 0.66516$ kJ/mol and $\sigma_O = 3.3687$ Å. The correspondence between simulation and experiment is shown in Fig. 7.1, together with the GCMC results of Boutin *et al.* [21]. Our potential markedly better reproduces the jump in the amount of adsorbed material in the transition region.

7.2.2 Methane diffusion

To model methane we used Lennard-Jones parameters $\varepsilon_{CH_4} = 1.13908$ kJ/mol and $\sigma_{CH_4} = 3.8220$ Å, and to model the zeolite, the oxygen parameters found above were used. Dynamics runs were carried out in the NVT ensemble (with separate temperature scaling per pore) at a temperature of 300 K. The pores were filled to a density of 0.7 molecules per unit cell.

To study the tracer diffusion of the methane molecules, a 50 ns production run was carried out after equilibration and the mean square displacement of the particles was calculated for correlation times up to 30 ns. The results are displayed in Fig. 7.2. The exponent α in the time dependence of the mean square displacement (Eq. 7.1) clearly shows two different regimes. The apparent deviation from the normal diffusion line at the highest correlation times is most probably due to a lack of statistics. Not only does one have fewer measurements of the displacements for such long correlation times, but also do these values scatter much more than those of the shorter correlation times and therefore need more sampling to obtain similar reliability.

In the short-time limit, where particle passings are so infrequent that they do not play a major role in the diffusion, a single-file type diffusion might be expected ($\alpha = 0.5$). Indeed the exponent α is much less than 1, but the value of 0.625 that is actually found indicates a profound deviation of strict single-file behaviour. Evidently, particle crossings, although infrequent, influence the diffusion already at short correlation times. Such a transitional behaviour has been reported before by Keffer *et al.* [107].

Note that with our potential parameters, passing is most probably allowed, which is in contrast to what was proposed experimentally by Kukla *et al.* [115]. As to be expected when

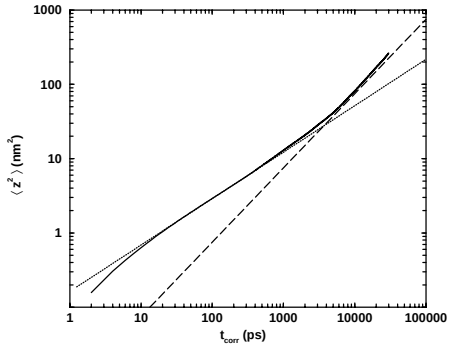

Figure 7.2: Mean square displacement curve for methane in $AlPO_4$-5 (molecular dynamics simulation results). Guide lines are drawn as $\propto t^{0.625}$ (dotted line) and $\propto t$ (dashed line).

particles can pass each other, the long-time limit shows an approach to normal diffusion $\alpha = 1$. However, since it was claimed by Kärger *et al.* [105] that such a transition might also be caused by the imposition of periodic boundary conditions, it is not yet clear at this point if the transition shown in our graph is of physical origin or just an artefact of using too small a box. To be sure that the picture is not troubled by system size effects, a closer study was necessary. In order to be able to do so within reasonable computation times, we developed a simplified one-dimensional hop-and-cross model to mimic the molecular dynamics simulations, which will be described in the next section.

7.3 The hop-and-cross model

The dynamics to be described in this section takes place on a one-dimensional sequence of sites, on which periodic boundaries are implied (the last site is connected with the first site). In the initial stage, particles are distributed randomly over these sites, with the restriction that no double occupancy is allowed. Then, in the dynamics stage, trial moves are carried out sequentially for randomly chosen particles. For a given particle, there are three possibilities: a turn to the left, a turn to the right, or a rest at its original location. For a turn to the left or to the right there are again two situations: the neighbouring site is either empty or occupied. In case it is empty the change of the particle to move to this site is given by the probability p_{hop}. If on the other hand the neighbouring site is occupied, the probability of the particle to move to that site is given by p_{cross}, which at the same time involves the movement of the neighbouring particle to the site the original particle is coming from (i.e., both particles are interchanged). The probability for a particle to remain at its position thus depends on the occupancies of its neighbouring sites and is given by the complement of the changes to go either to the left or to the right. When the number of trial moves has become equal to the number of particles in the system, we say that one timestep has passed. The timestep used in the hop-and-cross model can be substantially larger than the one in the molecular dynamics simulation. In the latter case, the timestep should be so small as to ensure a stable numerical solution to the equations of motion, whereas in the hop-and-cross model the timestep can be

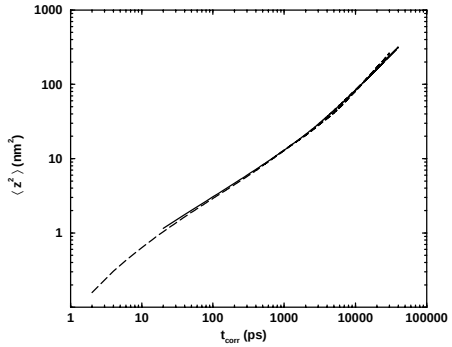

Figure 7.3: Mean square displacement curves showing agreement between hop-and-cross model (straight line) and molecular dynamics results (dashed line).

of the order of time in which a particle would travel from one site to another. In the $AlPO_4$-5 unit cell, there are two 12-rings and two 6-rings of oxygens, and adsorption takes place on the latter ones. Thus one crystallographic unit cell in the molecular dynamics simulation box corresponds to two sites in the hop-and-cross model.

7.3.1 Reproduction of MD results

To start the investigation, we first tried to mimic the MD simulation as closely as possible. Therefore, each pore of the simulation box was divided into 120 sites (there were 60 unit cells in the *z*-direction), with the dividing planes at the potential energy maxima. Hopping probabilities were calculated by counting the number of times that a particle had moved from one site to an empty neighbouring site between two time frames. The time interval between two frames was 0.2 ps, so this also sets the timestep in the hopping model to 0.2 ps. On the one hand, this proved to be large enough to get a reasonable hopping probability and on the other hand short enough to prevent particles from moving through more than one site between two successive time frames. For the current loading of 0.7 molecules per unit cell and at the chosen temperature of 300 K, a hopping probability $p_{\mathrm{hop}} = 0.125$ was found.

The crossing probability proved to be more difficult to calculate from the MD simulations, since a molecule that moves in the direction of an occupied site, sometimes resides together with the neighbouring particle in the same site for a while which leads to ambiguities in the counting procedure and on the other hand, actual crossings often are followed by rapid recrossings, which leads to an overestimation of the effective crossing probability. This is not easily accounted for, since the timescale at which recrossings settle down is not seperated well from the timescale of hopping to free sites. For these reasons we decided to keep p_{cross} as a yet unknown parameter that could be determined later by fitting the mean square displacement curve from the one-dimensional model to that of the MD simulation.

To mimic the molecular dynamics system as closely as possible, we set up our one-dimensional system as 120 sites with 42 particles (0.7 molecules per unit cell corresponds to 0.35 particles per site). Periodic boundary conditions were applied to the system. Initially, particles were distributed randomly over the sites (with the restriction of no double

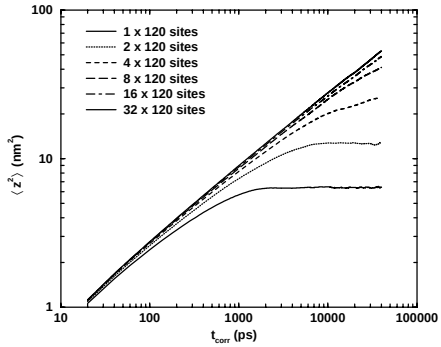

Figure 7.4: Study of system size effects for strict single-file system ($p_{\mathrm{cross}} = 0$).

occupancies) and subsequently, equilibration runs were carried out for 1,000,000 timesteps of 0.2 ps. Then production runs were carried out for another 24,000,000 timesteps (4.8 μs simulation time). These extensive run times proved to be necessary to obtain good statistics. Apparently, the one-dimensional calculations are more sensitive to statistical error than the MD calculations in this respect.

From the production runs, mean square displacements were calculated up to correlation times of 40 ns. The mean square displacements were calculated for particle trajectories that were corrected for center of mass motion (at all times, the center of mass motion was subtracted from the trajectories). The closest approximation of the MD results was reached with the crossing probability p_{cross} equal to 0.0008. The good correspondence is shown in Fig. 7.3.

With p_{hop} and p_{cross} both being determined accurately, the model is complete and has been shown able to reproduce the MD results. Now with the new model we can set out to study system size effects.

7.3.2 System size effects

To study the effect of the size of the periodic box, we did several model simulations with various box sizes. We started out this study by forbidding particle crossings ($p_{\mathrm{cross}} = 0$, $p_{\mathrm{hop}} = 0.125$). The reason for this is that this should yield strict single-file motion, for which the theoretical result is known ($\alpha = 0.5$). The results are plotted in Fig. 7.4, where the box size is given in units of 120 sites. As can be seen, for the original box length, the results already start to deviate at ca. 1000 ps correlation time. This is due to the fact that there is a limitation to the distance that particles can travel in the periodic box, since sooner or later they will bumb into their colleagues travelling in the opposite direction. This fact was recognized earlier by Hahn and Kärger [75]. The turnover displacements in our plot are in agreement with the analytical estimate for this quantity as presented by them. From the results in Fig. 7.4, it can be learned that, if we want to reveal the real nature of the crossover we found previously at a correlation time of about 3 ns, we have to go up to box sizes of at least 8 times 120 sites (corresponding to more than 400 nm).

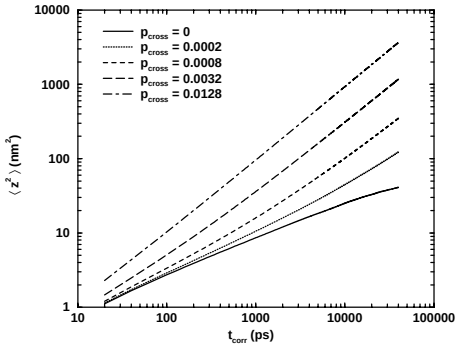

Figure 7.5: Range of diffusive behaviour from single-file to normal diffusion for different crossing probabilities. $n_{size} = 8$.

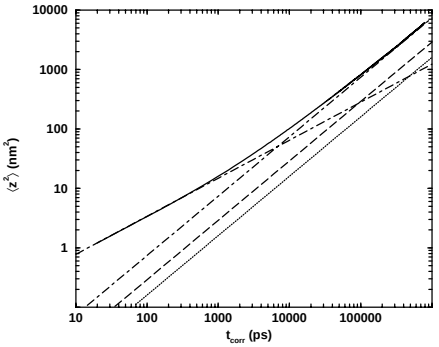

Figure 7.6: Final MC result for short and long-time diffusive regimes. $p_{\mathrm{cross}} = 0.0008$, $n_{size} = 8$. The dashed-dotted guidelines are drawn as $\propto t^{0.64}$ and $\propto t$ and the others show the extrapolated experimental results of Jobic *et al.* (dotted) and Nivarthi *et al.* (long dashed).

7.3.3 Large box results

To study the sensitivity of the system's behaviour to the crossover probability, we performed several model simulations with a box size of 8×120 sites, for different values of p_{cross}. The results can be seen in Fig. 7.5. The whole range of nearly single-file up to normal diffusion is covered in two to three orders of magnitude of the crossing probability. Notice that even the smallest value of p_{cross} largely influences the mean square displacement as a function of time, and that already a $p_{\mathrm{hop}}/p_{\mathrm{cross}}$ ratio as small as 1/10 produces normal diffusion over the whole time domain, down to the Newtonian timescale.

Finally, the mean square displacement is plotted for $p_{\mathrm{cross}} = 0.0008$ (the one which most closely resembled the MD simulation), but now with the large box size (Fig. 7.6). It is clear that a crossover can still be recognized, though less pronounced than in the original small-size simulation. Since the crossover takes places at a correlation time long before the system size effects the results, it is thus shown to be a real physical crossover.

7.4 Discussion

In this chapter, both molecular dynamics simulations and a simple Monte Carlo model have been used to investigate unidirectional diffusion of methane in the zeolite $AlPO_4$-5. First, molecular dynamics simulations on a rather small system were used to derive the time dependence of the mean square displacement. Next, a simple hop-and-cross model was introduced

to mimic the molecular dynamics simulations. After the tuning of a single parameter (the crossing probability), the results were reproduced very satisfactorily.

With the increased computational efficiency of the simplified model, we were able to carry out a thorough study of system size effects. These effects have shown to be of great importance and hence very large system sizes were needed to eliminate the influence of periodic boundaries on the longer timescales. Since these large sizes are not easily accessible by normal molecular dynamics simulations, the simplified model proved to be of great use.

Also after elimination of system size effects, the motion of the guest molecules is not strictly single-file in nature. Though infrequent, crossing events may occur, leading to a normal diffusive regime on large timescales. On short timescales, an intermediate behaviour is found, where the mean square displacement is proportional to $t^{0.64}$, while at a time of about 7 ns, a crossover to normal diffusion is found. These findings are in contrast with the experimental observation of single-file diffusion reported by Kukla *et al*. [115] in 1996, using Pulsed Field Gradient NMR, although the timescale of their experiments was far beyond the crossover time mentioned above. Their conclusions on methane in $AlPO_4$-5, however, are somewhat questionable. For CF_4 in $AlPO_4$-5, they observe a slowing down of the mean square displacement at large timescales which they attribute to blockages of the zeolite channels caused by impurities and imperfections. This effect sets a maximum length scale over which diffusion can trustfully be studied. In the case of methane however, the molecules have travelled a distance much longer than this length at all times accessible to the experiment. It is very well possible that the corresponding slowing down of the mean square displacement by the channel blockages has hidden the real character of the diffusion motion.

Two experimental studies confirming our findings have appeared in the literature: one, using Fourier transform PFG-NMR, by Nivarthi *et al.* [138] ($D = 2.9 \times 10^{-9}$ m^2/s), and one by Jobic *et al.* [98] ($D = 1.6 \times 10^{-9}$ m^2/s), using quasi-elastic neutron scattering (QENS). Both studies report normal diffusion on their accessible timescales, which are larger than ours, and are thus in agreement with our findings. The experimental mean square displacements, extrapolated to shorter timescales, along with our final results are plotted in Fig. 7.6. It can be seen that our mean square displacement has almost reached the linear regime, and that the diffusion coefficient we find ($D = 7.4 \times 10^{-9}$ m^2/s) is somewhat larger than the experimental ones. There is one very obvious way to repair this discrepancy, i.e., by changing the crossing probability p_{cross}. Fig. 7.5 shows that the slightest change in this value can have a large effect on the diffusion curve. There are several reasons one could think of why p_{cross} might be slightly overestimated. First it is possible that our fit in Fig. 7.3 could be ameliorated, and second the model system in the MD simulation could be improved, for instance the diameter σ_{CH_4} of the guest molecules could be enlarged, a potential other than a Lennard-Jones type could be used, or host lattice vibrations could be taken into account.

8 Transport diffusion of argon in $AlPO_4$-5

Transport diffusion of argon in the unidirectional channels of the molecular sieve $AlPO_4$-5 has been studied using molecular dynamics simulations. Using the Green-Kubo formalism, this nonequilibrium property is, for the first time, extracted from just one equilibrium simulation. Apart from the computational advantages above nonequilibrium simulations, the new method also provides a way to check the validity of the assumption of linear response, which is at the basis of both methods. The transport diffusion coefficient for argon at 87 K and half the maximum loading is found to be equal to $D_t = (1.4 \pm 0.1) \times 10^{-5}$ cm^2/s, of which approximately 20 % can be attributed to correlated, collective motion.[*]

8.1 Introduction

Unrestricted molecular transport in one-, two- or three-dimensional systems usually proceeds by ordinary diffusion. This is at the basis of the proportionality of the observation time and the mean square displacement of a tagged particle (tracer diffusion). The transport mechanism can change drastically, however, when molecules reside in restricted geometries. If for example particles are forced to move along one-dimensional channels such that they are restricted to maintain their sequential order, i.e., such that they are unable to pass each other, their mean square displacement becomes proportional to the square root of the observation time [54, 104, 155]. The underlying mechanism is called single-file diffusion.

The concept of single-file diffusion is a well-known phenomenon in ion transport through biological membranes, being introduced already in the 1950's [84]. In many cases, transmembrane ion diffusion takes place via pore-like channels, formed by large biomolecules, of which Gramicidin A is a classic example. In the Gramicidin A channel, the large discrepancy between the flux ratios of protons and other ions can be explained by the single-file nature of the transport of water molecules and Na^+ and K^+ ions, whereas the transport of protons occurs via a 'proton-wire' formed by the file of water molecules [57, 148].

[*] The work described in this chapter previously appeared in J. Chem. Phys. **113**(16), 6875 (2000). [86]

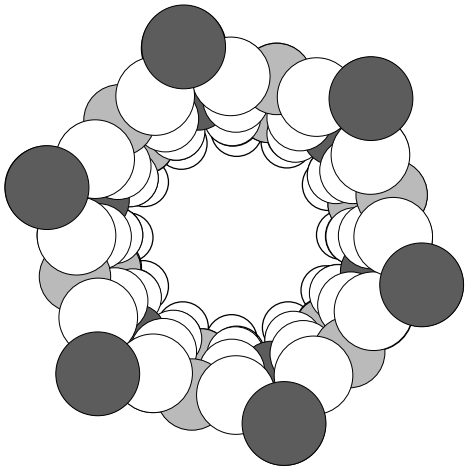

Figure 8.1: Pore structure of an $AlPO_4$-5 channel, showing only the oxygen atoms. The 12-rings of oxygen are in white and the alternating 6-rings in greyscale. For clarity, the van der Waals radii of the atoms have been reduced.

After its recognition in biophysics, anomalous diffusion in unidirectional channels was reported subsequently in a large variety of other systems, including the surface diffusion of chemisorbed species on crystal surfaces [67], ion transport along the chains of polymer electrolytes [47], molecular transport in zeolites [71, 74, 115] and most recently the diffusion of colloids in one-dimensional channels of micrometer scale [184]. Over recent years, zeolitic systems have become more and more recognized as ideal model systems to study the above-mentioned anomalous diffusion effects. They have well-defined pore structures and can nowadays almost be tailor-made with respect to pore sizes and network topologies. Besides their being suitable model systems, they also have huge commercial importance as environmentally friendly catalysts, ion-exchangers and molecular sieves.

The study of this work concerns diffusion of guest molecules in $AlPO_4$-5. This particular zeolite consists of a neutral crystal lattice with one-dimensional, non-interconnected pores. The pore cross sections, formed by 12-rings of oxygen, are nearly circular, with a minimum window size of approximately 7.3 Å. A sketch of the oxygen positions in the system can be seen in Fig. 8.1. The 12-rings are clearly directed inwards and constitute the main geometry of the pore. More outwards, alternating 6-rings can be found. For clarity, the van der Waals radii of the atoms have been reduced in the picture. In *Chapter 7* [168] we discussed the tracer diffusion of methane in this zeolite. Experimentally there has been a lot of debate whether methane would display single-file or normal diffusive behavior in the channels of $AlPO_4$-5. Kukla and co-workers performed pulsed field gradient (PFG)-nuclear magnetic resonance (NMR) measurements [74, 115] and claimed single-file diffusion, which was contradicted later by experiments of Nivarthi *et al.* [138] (Fourier transform PFG-NMR) and Jobic *et al.* [98] [quasielastic neutron scattering (QENS)]. In our study, we were able to relate these discrepancies to the difference in timescales probed by the experiments. We showed that the long-time limit of methane transport in this system should be diffusive and we succeeded in reproducing an approximate self-diffusion constant in close agreement with experiment. In this chapter, we will focus on argon diffusion in the same system. Being substantially

smaller (Lennard-Jones σ-parameter of 3.4050 Å vs. 3.8220 for methane), this molecule will not display single-file behavior. To further rule out the possibility of anomalous effects, we will make sure throughout this study to extend our correlation functions up to the nanosecond scale, which showed to be beyond the diffusive limit for methane as well (see *Chapter 7*).

Notwithstanding the relevance of the aforementioned experimental techniques, most practical applications of molecular transport in zeolites occur under nonequilibrium conditions, in particular situations in which a *macroscopic* concentration or chemical potential gradient is present. The diffusion coefficient that accounts for the collective motion of particles under the influence of a concentration gradient is called the transport diffusion coefficient D_t (as opposed to the self or tracer diffusion coefficient D_s). Nowadays, there is a whole class of macroscopic experiments available that probe the transport diffusivity, such as uptake rate measurements [150], permeation rate measurements [80], and frequency response analyses [181]. Just very recently, two *microscopic* techniques have become available that measure intracrystalline transport diffusion [99, 156], but they have not yet been applied to unidimensional pore systems.

Up till now, only few simulation techniques have been developed for diffusion under nonequilibrium conditions. Müller-Plathe *et al.* [135] used nonequilibrium simulations to study the transport of small gas molecules through an amorphous polymer matrix. The first application to diffusion in zeolites was shown by Maginn *et al.* [123] in the same year 1993. They used two nonequilibrium molecular dynamics methods to study the transport diffusion of methane in the two-dimensional silicalite network. The gradient relaxation molecular dynamics (GRMD) method more or less mimics a macroscopic situation: a (periodic) concentration profile is set up in the simulation box and subsequently let to relax. Profiles resulting from the relaxation of different initial configurations are being fit to the general solution of Fick's law to obtain transport diffusivities. For obtaining reasonable accuracy, this method is computationally very demanding. Furthermore, the method relies on the assumption that the system is in the linear response regime. A check thereof is in principle possible by repeating the procedure for different concentration gradients and checking whether the diffusion coefficient is not influenced by that, but this would increase the computational demands by yet another order of magnitude. Therefore an alternative approach, called color field nonequilibrium molecular dynamics (NEMD), was presented as well. In this method, a particle flux is generated by giving each particle a 'color' charge and then applying a corresponding color field. This color field thus replaces the chemical potential gradient present in a concentration profile as the driving force for diffusion. Although this method is much easier to use than the GRMD, it still requires several nonequilibrium simulations.

Note that with the term 'nonequilibrium', we refer to systems that are thermodynamically not in equilibrium. The above simulation techniques all try to mimic an experimental technique, either a relaxation experiment (where an initial chemical potential gradient is allowed to relax), or a steady-state experiment (where the gradient is kept intact by the application of an external force). Both methods probe the same property, i.e., the transport diffusion coefficient. This in contrast to the self-diffusion coefficient, which is typically evaluated under thermodynamic equilibrium (experimentally for instance with NMR measurements or in simulations by calculating the mean square displacement of tracer particles in a system without gradients).

In this chapter, we present a method to extract the nonequilibrium transport diffusivity from the fluctuations in an equilibrium simulation. The method is based on Onsager's regression hypothesis, and will now for the first time be applied to the study of collective diffusion in zeolites. (A similar application of Onsager's hypothesis was used in *Chapters 2 and 5* to calculate the kinetic coefficient of atomic crystal growth.) The benefit on computational grounds is twofold: there is no more need to maintain a rather difficult nonequilibrium situation and there is essentially no limit in the occupancies one can manage. In the next section we will present the theories we use and in subsequent sections we will present our results for the macroscopic transport diffusivity of argon in $AlPO_4$-5 and elucidate two distinct contributions, i.e., self motion and collective motion.

8.2 Theory

The diffusion of particles under the influence of a spatial density variation is adequately described by Fick's second law:

$$\frac{\partial \rho(\mathbf{r},t)}{\partial t} = D_t \nabla^2 \rho(\mathbf{r},t), \tag{8.1}$$

where $\rho(\mathbf{r},t)$ denotes the time-varying density profile and D_t the transport diffusion coefficient. In general, this relation is used for systems subjected to a macroscopic density gradient, but it also holds for an equilibrium situation where $\rho(\mathbf{r},t)$ accounts for fluctuations around the equilibrium density profile $\rho_{\mathrm{eq}}(\mathbf{r})$. In fact, as Onsager stated already in the 1930's, in a system close to equilibrium one cannot distinguish between spontaneous fluctuations and deviations from equilibrium that are externally prepared [36]. Thus, according to Onsager's regression hypothesis, microscopic equilibrium fluctuations on average decay according to their corresponding macroscopic law. In the present case, the macroscopic law is given by Eq. (8.1) and can be solved in Fourier space to yield

$$\hat{\rho} = \hat{\rho}_0 e^{-D_t k^2 t}. \tag{8.2}$$

In combination with Onsager's statement, this leads to the following expression for density fluctuation correlations at equilibrium:

$$\langle \hat{\rho}(\mathbf{k},t)\hat{\rho}^*(\mathbf{k},0)\rangle = \langle \hat{\rho}(\mathbf{k},0)\hat{\rho}^*(\mathbf{k},0)\rangle\, e^{-D(k)k^2 t}. \tag{8.3}$$

Here $\hat{\rho}(\mathbf{k},t)$ stands for a Fourier component of a density fluctuation with respect to the equilibrium density

$$\hat{\rho}(\mathbf{k},t) = \int d\mathbf{r} \left\{ \rho(\mathbf{r},t) - \rho_{\mathrm{eq}}(\mathbf{r}) \right\} e^{i\mathbf{k}\cdot\mathbf{r}}, \tag{8.4}$$

where

$$\rho(\mathbf{r},t) = \sum_n \delta\left(\mathbf{r} - \mathbf{r}_n(t)\right), \tag{8.5}$$

and $\rho_{eq}(\mathbf{r})$ is the equilibrium density at position $\mathbf{r}$; $\mathbf{r}_n(t)$ is the position of particle n at time t. For future use (Eq. 8.8) we notice

$$\frac{\partial\hat{\rho}(\mathbf{k},t)}{\partial t} = \frac{\partial}{\partial t}\sum_n e^{i\mathbf{k}\cdot\mathbf{r}_n(t)} = i\sum_n \mathbf{k}\cdot\mathbf{v}_n(t)e^{i\mathbf{k}\cdot\mathbf{r}_n(t)}, \tag{8.6}$$

where $\mathbf{v}_n(t)$ is the velocity of particle n at time t.

Note that in Eq. (8.3) we introduced a k-dependence of the diffusion coefficient, since Onsager's hypothesis strictly speaking only applies in the linear response regime, i.e., for not too rapidly varying density profiles (small k-vectors).

We are now in the position to elaborate Eq. (8.3) somewhat further [24]. By taking the time derivative of the left and right hand sides we arrive at

$$-\frac{1}{k^2}\frac{\partial}{\partial t}\langle\hat{\rho}(\mathbf{k},t)\hat{\rho}^*(\mathbf{k},0)\rangle = \langle\hat{\rho}(\mathbf{k},0)\hat{\rho}^*(\mathbf{k},0)\rangle D(k)e^{-D(k)k^2t}. \tag{8.7}$$

Writing the left hand side as the integral of its derivative we obtain:

$$\begin{aligned} -\frac{1}{k^2}\frac{\partial}{\partial t}\langle\hat{\rho}(\mathbf{k},t)\hat{\rho}^*(\mathbf{k},0)\rangle &= -\int_0^t d\tau\,\frac{1}{k^2}\frac{\partial^2}{\partial\tau^2}\langle\hat{\rho}(\mathbf{k},\tau)\hat{\rho}^*(\mathbf{k},0)\rangle \\ &= \int_0^t d\tau\,\frac{1}{k^2}\left\langle\frac{\partial\hat{\rho}(\mathbf{k},\tau)}{\partial\tau}\frac{\partial\hat{\rho}^*(\mathbf{k},0)}{\partial\tau}\right\rangle, \end{aligned} \tag{8.8}$$

where in the final step we have made use of the time symmetry of equilibrium correlation functions. If we now substitute Eq. (8.6), we arrive at a Green-Kubo expression which relates the diffusion coefficient to velocity correlations (where the double sum runs over all pairs of particles):

$$\begin{aligned} &D(k)\,\langle\hat{\rho}(\mathbf{k},0)\hat{\rho}^*(\mathbf{k},0)\rangle\,e^{-D(k)k^2t} = \\ &\quad\int_0^t d\tau\left\langle\frac{1}{k^2}\sum_{l,m}(\mathbf{k}\cdot\mathbf{v}_l(\tau))(\mathbf{k}\cdot\mathbf{v}_m(0))e^{i\mathbf{k}\cdot(\mathbf{r}_l(\tau)-\mathbf{r}_m(0))}\right\rangle \end{aligned} \tag{8.9}$$

Since we are interested in diffusion on macroscopic length and time scales, we can simplify our expression by taking the appropriate limits. Taking the limit of zero wave vector (corresponding to density fluctuations with large wavelengths), will put the exponent to unity. The macroscopic timescale is reflected by subsequently taking the limit of $t\to\infty$. Note that the order in which these limits are taken is crucial. Our final simplification comes from the fact that in the present study, we present an application to diffusion in the *unidirectional* channels of $AlPO_4$-5, i.e., we are only interested in k-vectors parallel to the z-axis. This leaves us with only one term of all inner products:

$$\begin{aligned} &D(k_z)\frac{1}{N}\,\langle\hat{\rho}(k_z,0)\hat{\rho}^*(k_z,0)\rangle = \\ &\quad\int_0^\infty d\tau\left\langle\sum_{l,m}\frac{1}{N}v_{lz}(\tau)v_{mz}(0)e^{ik_z(z_l(\tau)-z_m(0))}\right\rangle. \end{aligned} \tag{8.10}$$

From now on we will stick to this one-dimensional representation. In the limit of $k \to 0$, the fluctuations become of macroscopic size and the limiting value represents the macroscopic transport diffusivity D_t.

The last factor on the left-hand side of Eq. (8.10) divided by the number of particles in the system, N, equals the structure factor $S(k)$:

$$S(k) = \frac{1}{N} \langle \hat{\rho}(k,0) \hat{\rho}^*(k,0) \rangle . \tag{8.11}$$

From the thermodynamic compressibility equation, it follows [78] that the zero wave vector limit of the structure factor is given by

$$\lim_{k \to 0} S(k) = \rho k_B T \kappa_T , \tag{8.12}$$

with κ_T the isothermal compressibility:

$$\begin{aligned} \kappa_T &= -\frac{1}{V} \left(\frac{\partial V}{\partial P} \right)_T = \frac{1}{\rho} \left(\frac{\partial \rho}{\partial P} \right)_T = \frac{1}{\rho^2} \left(\frac{\partial \rho}{\partial \mu} \right)_T \\ &= \frac{1}{\rho^2 k_B T} \left(\frac{\partial \rho}{\partial \ln f} \right)_T = \frac{1}{\rho k_B T} \left(\frac{\partial \ln \rho}{\partial \ln f} \right)_T . \end{aligned} \tag{8.13}$$

The right-hand side of Eq. (8.10) is usually called the corrected diffusivity, D_0, which can be split into an autocorrelation part and a part containing cross-correlations. The autocorrelation term represents the self-diffusion of the particles and taking zero wave vector we arrive at the usual Green-Kubo relation for the macroscopic self-diffusion constant:

$$D_s = \frac{1}{N} \sum_l \int_0^\infty d\tau \, \langle v_{lz}(\tau) v_{lz}(0) \rangle \tag{8.14}$$

This, together with Eqs. (8.10) – (8.13), provides us with a relation between the macroscopic self and transport diffusion coefficients:

$$D_t = \left(\frac{\partial \ln f}{\partial \ln \rho} \right)_T \left\{ D_s + \lim_{k \to 0} \int_0^\infty d\tau \left\langle \sum_{l \neq m} \frac{1}{N} v_{lz}(\tau) v_{mz}(0) e^{ik(z_l(\tau) - z_m(0))} \right\rangle \right\} . \tag{8.15}$$

The summation over the cross terms in Eq. (8.15) represents the way in which the motion of a single particle is influenced by the initial motion of its surrounding particles. At very low particle densities, those cross-correlations will be negligible and the corrected diffusivity will equal the self-diffusion coefficient. In that limit, we arrive at the familiar Darken equation:

$$D_t \cong D_s \left(\frac{\partial \ln f}{\partial \ln \rho} \right)_T . \tag{8.16}$$

All relations have been derived for fluctuations in the equilibrium density distribution. Eq. (8.10) thus provides us with a tool to calculate the product $D(k)S(k)$ for different wave vectors from one equilibrium simulation. Note the big advantage over nonequilibrium simulations, where each different k-vector would stand for a separate simulation. Furthermore,

the structure factor $S(k)$ can be directly determined using its definition in Eq. (8.11). The combination gives us $D(k)$ which for $k \to 0$ will equal the macroscopic transport diffusion constant. By comparison with the self-diffusion coefficient in Eq. (8.14), the contribution of correlated motions can be determined and the validity of the Darken equation can be checked. Note that we cannot simply put k equal to zero in Eq. (8.10), since then the right hand side will be zero because of conservation of momentum.

8.3 Simulations

Molecular dynamics simulations were performed in the canonical ensemble on a system of argon adsorbed in $AlPO_4$-5. All simulations were done at a temperature of 87 K and at a loading of 3 molecules per unit cell, which roughly corresponds to half of the maximum loading. This loading was chosen such that interactions between guest molecules on the one hand are large enough to lead to collective motions and on the other hand are small enough to allow for substantial displacements. The $AlPO_4$-5 unit cell is hexagonal with lattice constants $a = 13.7707$ Å and $c = 8.3789$ Å [17, 127, 146]. The lattice was assumed to be rigid and host-guest interactions were restricted to interactions between the guest and the oxygen atoms of the lattice, which has been shown to be sufficiently accurate to calculate the diffusion of small spherical particles in this system [110]. The Lennard-Jones interaction parameters for argon we used were $\varepsilon_{Ar} = 0.96605$ kJ/mol and $\sigma_{Ar} = 3.4050$ Å, and for oxygen $\varepsilon_O = 0.66516$ kJ/mol and $\sigma_O = 3.3687$ Å. The latter were determined by fitting the argon adsorption isotherm to experimental values in the way as described in *Chapter 7* [168]. Throughout the simulations, we used a rectangular simulation box consisting of $2 \times 2 \times 60$ unit cells, thus containing four separate channels, directed along the z-axis. Potentials were cut off at 1.15 nm, so interactions between atoms in different channels were neglected and the four channels can be regarded as separate systems. The simulations were performed using an adapted version of the GROMOS simulation package [70]. Thermostatting is achieved by weak coupling to an external bath [18], for which we used a relaxation time of 0.1 ps. We adapted the thermostat so as to treat the individual pores independently, thus preventing non-interacting particles in different pores from influencing each other via the thermostat. This also included a routine to remove the center of mass movement in each pore at each timestep. On top of this, an extra routine was added to perform the calculation of the correlation term in Eq. (8.10) on-the-fly. Rewriting this equation in a summation of a real and an imaginary part gives:

$$D(k)S(k) = \frac{1}{N}\int_0^\infty dt\, \langle C(t) + iS(t)\rangle\,, \tag{8.17}$$

with

$$\begin{aligned} C(k,t) &= \{\sum_i v_{iz}(t)\cos(kz_i(t))\}\{\sum_j v_{jz}(0)\cos(kz_j(0))\} \\ &+ \{\sum_i v_{iz}(t)\sin(kz_i(t))\}\{\sum_j v_{jz}(0)\sin(kz_j(0))\} \end{aligned}$$

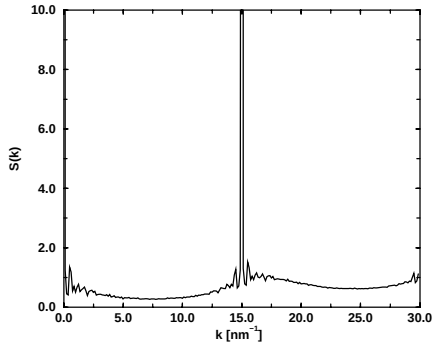

Figure 8.2: Structure factor as a function of wavenumber for argon in $AlPO_4$-5.

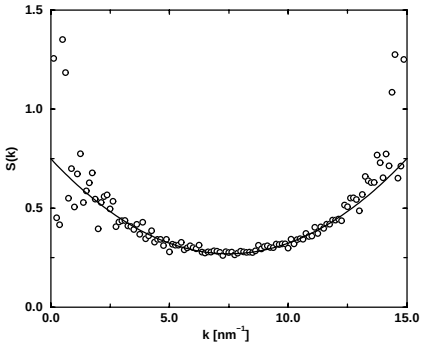

Figure 8.3: Low k-region of the structure factor of Fig. 8.2. The circles denote the results from the simulations and the solid line shows a quadratic fit of the points in the region between the two major peaks.

$$\begin{aligned} S(k,t) &= \{\sum_i v_{iz}(t)\sin(kz_i(t))\}\{\sum_j v_{jz}(0)\cos(kz_j(0))\} \\ &- \{\sum_i v_{iz}(t)\cos(kz_i(t))\}\{\sum_j v_{jz}(0)\sin(kz_j(0))\}. \end{aligned}$$

Thus, for each time-frame only two summations were needed for every wave vector k that was evaluated.

8.4 Results

First, the structure factor was calculated with the aid of Eq. (8.11) from a 500 ps simulation over a wide range of k-values. The result is given in Fig. 8.2. A major peak with several smaller harmonics can be seen at a wavenumber of 15.0 nm^{-1}, corresponding to a wavelength of $\lambda = 0.419$ nm which is just half of the corresponding unit cell axis. It can be surmized that the argon atoms preferentially occupy two rings of adsorption sites per unit cell, which was confirmed by density plots we calculated from the output of our simulations. These rings are located near the 6-rings of oxygen atoms in the $AlPO_4$-5 structure (see Fig. 8.1). This is consistent with the view of diffusion that occurs through atoms hopping from one site to another [104]. In Fig. 8.3 the interval between zero and the first peak of the structure factor is highlighted. These data were fitted by a quadratic function (also indicated in the figure), which yielded an extrapolated value for $S(k)_{k\to 0}$ of 0.75. This value should be equal to the inverse of the Darken factor $(\partial \ln f/\partial \ln \rho)_T$ at this particular loading. This information can directly be extracted from the adsorption isotherm. In Fig. 8.4 the adsorption isotherm (see also *Chapter 7*) is presented on a log-log scale. The tangent corresponds to a structure

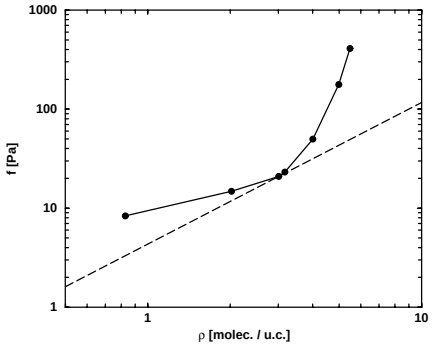

Figure 8.4: The adsorption curve (Fig. 7.1) presented on a log-log scale. The Darken factor is given by the tangent to this curve at a loading of 3 molecules per unit cell.

factor of 0.70, given by a four-point numerical differentiation. This is in close agreement with the previously determined result. As is clear from both approaches, the determination of the Darken factor via the first method is much more accurate, especially at this particular loading, where the adsorption isotherm displays its steep rise. However, the calculation of the structure factor over the whole k-range has not been a trivial task either. In order to get accurate results for small values of k, which is equivalent to probing density fluctuations of large wavelengths, the randomization of initial particle positions is extremely important. It appears that when one constructs initial configurations by putting exactly three particles in every unit cell and randomizes their positions within the unit cell, the structure factor drops to zero at small k. Only when distributing the total of 180 particles randomly over the whole pore of 60 unit cell lengths, does one find the right results at small values of k.

For the evaluation of $D(k)S(k)$ a 5 ns simulation was performed to calculate the four terms in Eq. (8.17) for twelve wave numbers k. As the correlation functions are the Fourier transforms of density fluctuations and the latter are real and even functions, the imaginary part of these functions should be zero. Deviations of the imaginary part from zero thus give an estimate of the accuracy of the real part. The product $D(k)S(k)$ for each wavenumber was obtained by integration of the real part $\langle C(t)\rangle$ in Eq. (8.17).

As an example, the integral of the correlation function at $k = 0.50\ \mathrm{nm}^{-1}$ as a function of its upper integration limit is shown in Fig. 8.5. The dashed lines give the approximate error margins as obtained by integration of the imaginary part. From this graph we determine a value of $D(k)S(k) = (0.95 \pm 0.10) \times 10^{-5}\ \mathrm{cm}^2/\mathrm{s}$ for the appropriate wave vector.

The same procedure has been repeated for the whole range of wave numbers, and the graph of $D(k)S(k)$ versus k is shown in Fig. 8.6. With the previously obtained quadratic fit of $S(k)$ in the relevant region we are now able to calculate $D(k)$, the result of which is presented in Fig. 8.7. Clearly, $D(k)$ reaches a plateau value for k approaching zero, which indicates that for those values of k we have reached the macroscopic limit (where D should be independent of the wave vector). The limiting value for $k \to 0$ gives us the macroscopic transport diffusion coefficient. Thus, for the transport diffusion of argon in $AlPO_4$-5 at a loading of 3 molecules per unit cell and a temperature of 87 K, we arrive at $D_t = (1.4 \pm 0.1) \times 10^{-5}\ \mathrm{cm}^2/\mathrm{s}$.

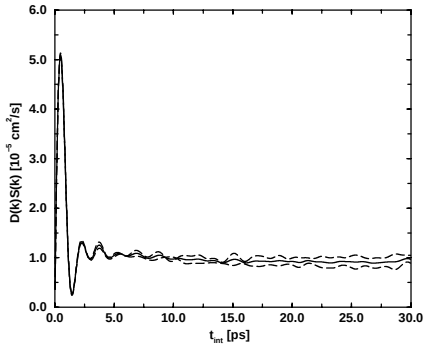

Figure 8.5: $D(k)S(k)$ vs. integration time for $k = 0.50$ nm^{-1}.

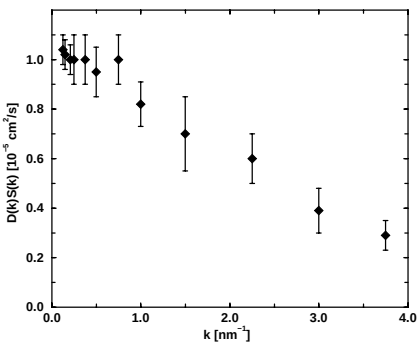

Figure 8.6: $D(k)S(k)$ as function of wave vector k.

Note that $D(k)$ only starts to reach its plateau for wave numbers $k < 0.4$ nm^{-1} corresponding to wavelengths larger than approximately 16 nm. This value sets a lower limit to the length of the simulation box to be used in both equilibrium and nonequilibrium simulations. If the concentration gradient set up in nonequilibrium simulations is substantially larger than the inverse of this wavelength, the results will become unreliable. It is part of the elegance of the present method that the check whether the linear response regime has been reached or not comes straight out of the simulation.

Finally, we will spend some words on the contributions of self vs. collective motions in the transport process. From the same (equilibrium) simulation that we used to determine the transport diffusion coefficient, we also determined the self-diffusion coefficient. To this end we evaluated the velocity autocorrelation function (VACF) from Eq. (8.14) over the first 0.5 ns after equilibration. The result is shown in Fig. 8.8. Integration of this VACF yields a self-diffusion coefficient of $D_s = 0.784 \times 10^{-5}$ cm^2/s. When neglecting cross-correlations, the corresponding transport diffusion coefficient would be given by the Darken equation [Eq. (8.16)]. This leads to a value of $D_t = 1.12 \times 10^{-5}$ cm^2/s. Comparing this with the result we got from the complete calculation, we see that the transport diffusion coefficient in the Darken approximation differs by 20 % from the actual value. Thus, at a loading of 3 molecules per unit cell, collective motions account for about 20 % of the total transport of argon in the $AlPO_4$-5 channels at this loading, and are therefore not negligible. At present, experimental methods are not accurate enough to probe this deviation from the Darken approximation. For example in table 12.2 of the book by Kärger and Ruthven [106], the self-diffusion coefficient D_s from NMR and neutron scattering experiments and the corrected diffusion coefficient D_0 ($= D_t S(0)$ in our notation) from the other techniques, are given in one and the same column. The scattering in the data (due to differences in loading, temperature, samples, and experimental techniques) is too large to find the subtle difference we measure.

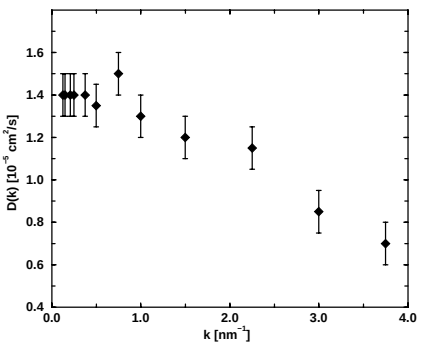

Figure 8.7: The k-dependent diffusion coefficient $D(k)$ as a function of wavenumber k.

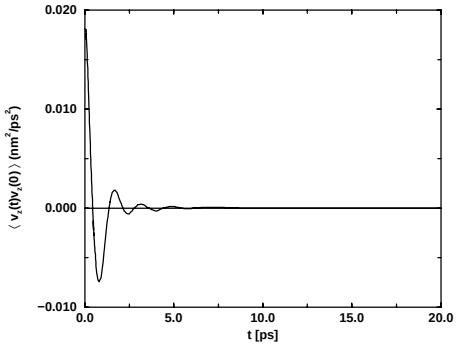

Figure 8.8: The velocity autocorrelation function for argon in $AlPO_4$-5 at a loading of 3 molecules per unit cell ($T = 87$ K).

8.5 Conclusions

In this chapter, we have introduced a method by which essentially nonequilibrium transport properties can be evaluated from equilibrium molecular dynamics simulations. Results were presented for the transport diffusion of argon in the unidirectional pores of $AlPO_4$-5. The simulations were done at a loading of 3 molecules per unit cell (approximately half the maximum loading) and a temperature of 87 K. For density fluctuations with wavelengths larger than 16 nm, the linear response regime was reached and the transport diffusion coefficient for this system was found to be $D_t = (1.4 \pm 0.1) \times 10^{-5}$ cm^2/s. It was shown that about 20 percent of this value can be attributed to correlated, collective motion. The increased contribution of group movement at higher loading is reflected in an underestimation of the transport diffusion coefficient when the Darken approximation would have been directly applied to the measured self-diffusion coefficient at the same loading.

9 The Einstein equation for transport diffusion

In this chapter, we investigate various methods to calculate corrected collective diffusion coefficients. We interpret the meaning of the center-of-mass coordinate that occurs in the usual Einstein expression for the corrected diffusivity and show that it should only apply to displacements of particles in the control volume. The use of unfolded particle trajectories in the expression is only valid for systems that are periodic and if the whole box is taken as the control volume. We derive a wavevector-dependent Einstein expression, equivalent to the Green-Kubo form we derived in Chapter 8*. We show that the box size dependence of the values derived from the usual Einstein equation is reproduced (at least for small k-values) by our expression applied to a large box. Finally, we discuss the order in which the limits of $k \to 0$ and $t \to \infty$ should be taken to arrive at the thermodynamic limit.*[*]

9.1 Introduction

Over the past 10-15 years, many simulation studies have appeared in the literature that calculate the transport of guest molecules through zeolites. Almost all of them, however, exclusively deal with the self or tracer diffusivity. Via the well-known Einstein equation, this quantity can be calculated from a single particle correlation function and is thus readily calculated in, e.g., molecular dynamics (MD) simulations, with excellent statistical accuracy. In many cases, calculations of the self-diffusion coefficient have proven able to reproduce measurements from microscopic experiments such as Pulsed Field Gradient Nuclear Magnetic Resonance (PFG-NMR) and Quasi-Elastic Neutron Scattering (QENS).

For most practical purposes, however, it is not the self-diffusivity that is of main interest but the transport diffusivity. The transport diffusion coefficient is the property that accounts for the collective motion of particles under the influence of a macroscopic gradient. Being a collective property, this is much more difficult to obtain reliably from atomistic simulations.

[*] The work described in this chapter has been submitted to J. Chem. Phys. [172]

The first attempts to calculate transport diffusion in zeolites (in this case methane in silicalite) were reported by Maginn *et al.* [123] in 1993. They used two different nonequilibrium techniques: Gradient Relaxation Molecular Dynamics (GRMD), where an initial nonequilibrium density profile is let to relax, and Colour Field Molecular Dynamics, where the particles are assigned a virtual colour charge and are then subjected to a colour field gradient. Both methods are computationally very demanding and in both cases it is difficult to apply gradients that are, on the one hand, small enough to ensure the system is in the linear response regime and, on the other hand, large enough to be able to distinguish them from spontaneous fluctuations in the density. The problems that arise in the construction of initial configurations for the GRMD simulations, where two boxes with different average densities are put together, are comparable to the problems we encountered in constructing initial configurations for our crystal-melt simulations (see, e.g., *Chapter 3*). In the light of that experience, the problems Maginn *et al.* experienced in getting reliable results out of the GRMD method might be largely due to their relatively small system sizes.

Maginn *et al.* also tried an equilibrium method, in which the transport coefficient was calculated from the flux-flux autocorrelation function:

$$D_t = \left(\frac{\partial \ln f}{\partial \ln c}\right)_T \frac{1}{3N} \int_0^\infty dt \langle \mathbf{j}(t) \cdot \mathbf{j}(0) \rangle, \tag{9.1}$$

with the microscopic flux $\mathbf{j}$ defined as

$$\mathbf{j} = \sum_{l=1}^{N} \mathbf{v}_l, \tag{9.2}$$

in which f is the fugacity of the guest molecules and c their concentration. This equation results from linear response theory and already appeared early in the literature (see, e.g., Ref. [53, 76]). It has been used for long in the theory of two-dimensional surface diffusion and it is equivalent to our Eq. 8.9 in the limit of $k \to 0$. Maginn *et al.* did not find the equation particularly useful since the flux-flux autocorrelation function has a long-time tail that oscillates around zero (in contrast to the single-particle velocity autocorrelation function, where this Green-Kubo formalism is routinely used to calculate self-diffusion coefficients). Today, with the availability of much more computing power, transport diffusion in zeolites is almost exclusively calculated by equilibrium simulations, since they lack the problems mentioned earlier.

As an alternative to the Green-Kubo expression, the transport diffusivity can be calculated via the equivalent Einstein expression:

$$D_t = \frac{1}{6N} \left(\frac{\partial \ln f}{\partial \ln c}\right)_T \frac{d}{dt} \left\langle \left(\sum_{l=1}^{N} (\mathrm{r}_l(t) - \mathrm{r}_l(0)) \right)^2 \right\rangle. \tag{9.3}$$

This equation has long been known in the field of surface diffusion [20, 67, 179] and was first suggested for use in zeolitic diffusion in a paper by Theodorou *et al.* [173].

Sanborn and Snurr [153] calculated the diffusion of binary mixtures of CF_4 and *n*-alkanes in faujasite. Besides a Green-Kubo equation similar to Eq. 9.1 but generalized to multi-component diffusion, they used the corresponding Einstein form. Good agreement was found between the Einstein and the Green-Kubo results.

In a succeeding study by Sanborn and Snurr [154], they again studied a CF_4-methane mixture in faujasite, but now at various loadings. They used the calculated transport coefficients in a phenomenological flux equation over a whole membrane and concluded that neglection of the cross-term Onsager coefficients L_{ij} (with $i \neq j$), which is sometimes done in Maxwell-Stefan models, can lead to quantitative (and sometimes even qualitative) errors. They reported difficulties in obtaining consistent values for the L coefficients in two cases: for the minor component as the composition of the other approaches 100 %, and for all components in the limit of very low loadings. Despite several attempts to adjust the simulation parameters, the problems remained unresolved.

Skoulidas and Sholl [161] studied the transport diffusion of CH_4 and CF_4 in silicalite at a range of temperatures and loadings using the Einstein form. In contrast to the early results of Maginn *et al.* they reported large deviations from the Darken equation.

In an earlier study, Sholl [160] investigated the macroscopic flux of Xe through $AlPO_4$-31 and CF_4 through $AlPO_4$-5 (both single-file systems). He used a coarse-grained model of hopping on a lattice, but including various kinds of concerted motion, of which the hopping parameters were taken from atomistic simulations. He calculated the corrected diffusivity from the decay of cosine transformations of the density:

$$\langle C_k(t)C_k(0)\rangle = \langle C_k(0)C_k(0)\rangle e^{-Dk^2t}, \tag{9.4}$$

with

$$C_k(t) = \sum_{i=1}^{N} \cos(kz_i(t)) - \left\langle \sum_{i=1}^{N} \cos(kz_i(t)) \right\rangle. \tag{9.5}$$

This is similar to the approach we took in *Chapter 8* and to the equation we will derive in the present study (Eq. 9.15), although we use in both cases the full Fourier transform of the density and not only the cosine part. Sholl remarked that "... it examines the decay of spontaneous density fluctuations in an equilibrium system, so no assumption about the applicability of linear response theory need to be made." We saw in Fig. 8.6 that this is not strictly true, since it depends on the *k*-values that are examined. Given the large system sizes that Sholl reached with his coarse-grained model, he found a perfectly constant diffusion coefficient with the 4 *k*-values that he examined.

Note that also Eqs. 9.1 and 9.3 are strictly only true for macroscopic density fluctuations. In an earlier study of ours (*Chapter 8*), we introduced the wavevector dependent form of the Green-Kubo equation and studied explicitly the *k*-dependence of the diffusion coefficient. This procedure had the obvious merit that it provided direct information on the regime of linear response (i.e., those wavelengths where D_t becomes independent of k). In Eqs. 9.1 and 9.3 the limit of $k \to 0$ has already been taken and as a consequence any such information is lost. The maximum wavelength (minimum *k*-value) of density fluctuations that can be probed in a periodic system is equal to the length of the simulation box. Therefore it might

be anticipated that when the above equations are applied in various simulation systems of decreasing size, a trend may be found similar to the k-dependence of D_t as shown in Fig. 8.7. In the present study we will investigate the system size dependence of the measured transport diffusivity by performing simulations with several box sizes and compare the results to an explicit wavevector-dependent equation applied to the largest box. In contrast to our earlier study, we will use the Einstein formalism. This has the advantage that the integration over the velocities is already carried out at each timestep by the integration scheme and does not need to be performed afterwards. This leads to less statistical errors and the interval between frames where data is stored to disk can be taken longer.

9.2 Theory

9.2.1 The Einstein form for D_c

In this chapter, we will focus on the calculation of the 'corrected diffusivity'

$$D_c = \frac{1}{N}\int_0^\infty d\tau \left\langle \sum_{l=1}^{N}\sum_{m=1}^{N} v_{lz}(\tau)v_{mz}(0) \right\rangle, \tag{9.6}$$

which is equal to the transport diffusivity divided by the thermodynamic correction factor $(\partial \ln f/\partial \ln c)_T$. The above expression can be brought into the equivalent Einstein-form by working out the mean square displacement of the center of mass Z of the total number of molecules in the system:

$$\begin{aligned}
\left\langle (Z(t)-Z(0))^2 \right\rangle &= \left\langle \left(\frac{1}{N}\sum_{l=1}^{N} z_l(t) - z_l(0)\right)\left(\frac{1}{N}\sum_{m=1}^{N} z_m(t) - z_m(0)\right) \right\rangle \\
&= \frac{1}{N^2}\int_0^t ds \int_0^t du \left\langle \sum_{l=1}^{N}\sum_{m=1}^{N} v_{lz}(s)v_{mz}(u) \right\rangle = \frac{2}{N^2}\int_0^t ds \int_0^s du \left\langle \sum_{l=1}^{N}\sum_{m=1}^{N} v_{lz}(s)v_{mz}(u) \right\rangle \\
&= \frac{2}{N^2}\int_0^t ds \int_0^s du \left\langle \sum_{l=1}^{N}\sum_{m=1}^{N} v_{lz}(s-u)v_{mz}(0) \right\rangle = \frac{2}{N^2}\int_0^t ds \int_0^s d\tau \left\langle \sum_{l=1}^{N}\sum_{m=1}^{N} v_{lz}(\tau)v_{mz}(0) \right\rangle \\
&= \frac{2}{N^2} s \int_0^s d\tau \left\langle \sum_{l=1}^{N}\sum_{m=1}^{N} v_{lz}(\tau)v_{mz}(0) \right\rangle \Bigg|_0^t - \frac{2}{N^2}\int_0^t ds\, s \left\langle \sum_{l=1}^{N}\sum_{m=1}^{N} v_{lz}(s)v_{mz}(0) \right\rangle \\
&= \frac{2}{N^2}\int_0^t d\tau (t-\tau) \left\langle \sum_{l=1}^{N}\sum_{m=1}^{N} v_{lz}(\tau)v_{mz}(0) \right\rangle.
\end{aligned} \tag{9.7}$$

The velocity autocorrelation function decays to zero over a time in which τ is very small which, together with Eq. 9.6, leads to

$$N\left\langle (Z(t)-Z(0))^2 \right\rangle = 2D_c t, \tag{9.8}$$

the Einstein form for the corrected diffusivity.

The velocities in Eq. 9.6 relate to the particle flux in a specific control volume. This gives a specific meaning to the integrals in line 2 of Eq. 9.7, namely that only particles in the control volume should be taken into account. As a consequence, the displacements in line 1 relate to (parts of) trajectories that take place in the simulation box, which is exemplified by the following expression:

$$Z(t) - Z(0) = \sum_{i=1}^{N} \int_0^t d\tau v_{zi}(\tau)\chi(z_i(\tau)) = \sum_{i=1}^{N} \sum_{n=1}^{n_t} \Delta z_i(n)\chi(z_i(\tau)) \tag{9.9}$$

with n the count of the integration timesteps, and $\chi(z)$ the characteristic function which equals 1 inside the control volume and 0 outside. In the case of a periodic system, however, the integrals can be calculated in an alternative way. Consider a particle that is leaving the simulation box at the left hand side. From that moment on, it does not contribute anymore to the particle flux in the control volume (i.e., the central simulation box). At the same time, however, its periodic image enters the box at the right hand side. *That* particle contributes, say, a distance $v\Delta t$ in the next timestep to the motion of the material in the system. Because of the exact correlation between the motions of a particle and its images the contribution of the image that enters the box could just as well be added to the motion of the particle that left the box. Therefore Eq. 9.8 can be conveniently evaluated as the total displacement of the *unfolded* trajectories of all the particles that were once located within the box. It is important to realize that this is only by virtue of the periodicity of the system and applies only when the whole simulation box is taken into account.

9.2.2 A wavevector-dependent Einstein form

We will now derive a wavevector-dependent expression for the corrected diffusivity, equivalent to Eq. 8.9. Starting from Eq. 8.3 we can write, for small values of k_z:

$$\frac{d}{dt}\left\langle \hat{\rho}(k_z,t)\hat{\rho}^*(k_z,0)\right\rangle = -D_t(k_z)k_z^2\left\langle \hat{\rho}(k_z,0)\hat{\rho}^*(k_z,0)\right\rangle, \tag{9.10}$$

where it should be noted that $\hat{\rho}(k,t)$ stands for the Fourier component of the deviation of the density from its equilibrium distribution. With

$$S(k_z) = \frac{1}{N}\left\langle \hat{\rho}(k_z,0)\hat{\rho}^*(k_z,0)\right\rangle = \frac{1}{N}\left(\frac{\partial \ln c}{\partial \ln f}\right)_T, \tag{9.11}$$

we arrive at

$$D_c(k_z) = -\frac{1}{Nk_z^2}\frac{d}{dt}\left\langle \hat{\rho}(k_z,t)\hat{\rho}^*(k_z,0)\right\rangle. \tag{9.12}$$

Making use of the fact that both the right-hand and left-hand side are real, and adding two time-independent averages, we can write

$$D_c(k_z) \quad = \quad \frac{1}{N}\frac{1}{2k_z^2}\frac{d}{dt}\left\{\left\langle \hat{\rho}(k_z,t)\hat{\rho}^*(k_z,t)\right\rangle - \left\langle \hat{\rho}(k_z,t)\hat{\rho}^*(k_z,0)\right\rangle\right.$$

$$
\begin{aligned}
& - \langle \hat{\rho}(k_z,0)\hat{\rho}^*(k_z,t)\rangle + \langle \hat{\rho}(k_z,0)\hat{\rho}^*(k_z,0)\rangle \} \\
= \;& \frac{1}{N}\frac{1}{2k_z^2}\frac{d}{dt}\left\langle \left(\hat{\rho}(k_z,t) - \hat{\rho}(k_z,0)\right)\left(\hat{\rho}^*(k_z,t) - \hat{\rho}^*(k_z,0)\right)\right\rangle \\
= \;& \frac{1}{N}\frac{1}{2k_z^2}\frac{d}{dt}\left\langle \left(\sum_{l=1}^{N} e^{ik_z z_l(t)} - \hat{\rho}_{\mathrm{eq}} - \sum_{m=1}^{N} e^{ik_z z_m(0)} + \hat{\rho}_{\mathrm{eq}}\right)\right. \\
& \qquad \left. \times \left(\sum_{n=1}^{N} e^{-ik_z z_n(t)} - \hat{\rho}_{\mathrm{eq}} - \sum_{p=1}^{N} e^{-ik_z z_p(0)} + \hat{\rho}_{\mathrm{eq}}\right)\right\rangle \\
= \;& \frac{1}{N}\frac{1}{2k_z^2}\frac{d}{dt}\left\langle \sum_{l=1}^{N}\left(e^{ik_z z_l(t)} - e^{ik_z z_l(0)}\right)\sum_{m=1}^{N}\left(e^{-ik_z z_m(t)} - e^{-ik_z z_m(0)}\right)\right\rangle, \qquad (9.13)
\end{aligned}
$$

with $\hat{\rho}_{\mathrm{eq}}$ the Fourier transform of the equilibrium density. Note that the last step is only valid if exactly the same number of particles is present in the system at any time. By definition, this holds true in a periodic system if the whole volume is taken into account.

In the final expression, the limit to small wavevectors could be taken again. By Taylor expansion up to first order, Eq. 9.8 is then recovered. Since in a finite periodic system of length L_z the smallest possible value of k_z equals $2\pi/L_z$, this Taylor expansion is only possible for finite and not too large values of t. If no Taylor expansion is performed, and t is extended to macroscopic timescales, the difference $e^{-ik_z z_l(t)} - e^{-ik_z z_l(0)}$ will eventually sample the interval $[0,1)$, and the average in Eq. 9.13 will level off to a constant value.

In both cases, first the limit $L_z \to \infty$ has to be taken, and only then t can be extended to macroscopic times. The same conclusion follows when Eq. 8.3 is Fourier transformed into the frequency domain:

$$
\frac{\omega^2}{k_z^2}\int_0^\infty dt \langle \hat{\rho}(k_z,t)\hat{\rho}^*(k_z,0)\rangle e^{-i\omega t} = \langle \hat{\rho}(k_z,0)\hat{\rho}^*(k_z,0)\rangle \frac{\omega^2}{k_z^2}\frac{D_t k_z^2}{D_t^2 k_z^4 + \omega^2}. \qquad (9.14)
$$

From this it is clear that first $k \to 0$ should be taken, and only then $\omega \to 0$. If the limits are taken in the reverse order, the right hand side tends to zero instead of to D_t.

In the perspective of the current derivation, the positions z relate to the positions of particles in the box. If Eq. 9.8 is calculated with the center-of-mass position from the (folded) positions of the particles in the box, this expression will level off as well. In that interpretation, if the limit to zero wavevector should be taken, the box size should be increased correspondingly. In the limit of infinite system size (the usual thermodynamic limit), neglecting edge effects of particles crossing the periodic boundary, the expression remains feasible. If the expression is transformed into the Green-Kubo form (Eq. 8.9) the limit can be taken of $k \to 0$, regardless of the choice for unfolding particle trajectories or not. This puts also Eqs. 9.1 and 9.3 into perspective; first the limit is taken to zero wavevector (which is equivalent to deriving the expression for infinite system sizes), and subsequently the result is applied to finite systems in the limit of $t \to \infty$.

9.3 Simulations

We performed canonical and microcanonical molecular dynamics simulations on a system of argon absorbed in $AlPO_4$-5, with the same interaction parameters as in *Chapter 8*. We used a timestep of 1 fs throughout and in the canonical simulations kept the average temperature at its desired value by using a Nosé-Hoover thermostat with a relaxation time of 1.0 ps. All simulations were done at a loading of 3 particles per unit cell and at a temperature of 87 K. They were performed with system sizes of 5, 10, 20, 30, and 60 unit cells in the *z*-direction (the direction of the pore). In all cases, the simulation box contained one single pore. Thermodynamic averages were taken by performing several simulations at the same state but with different initial configurations.

In order to speed up the simulations, we used pretabulated sorbate-zeolite interactions on a grid (in contrast to *Chapter 8*, where we did a full atomic simulation). Forces and energies were evaluated via tricubic Hermite interpolation over the energy field, with a grid spacing of 0.1 Å. The reader is referred to the Appendix for an extensive discussion of the choice of the interpolation scheme in these kinds of simulations.

The imaginary exponents in the one but last line of Eq. 9.13 were further worked out to give

$$\begin{aligned} D_c(k_z) &= \frac{1}{N}\frac{1}{2k_z^2}\frac{d}{dt}\left\langle \left(\sum_{l=1}^{N}\cos k_z(z_l(t)) - \sum_{l=1}^{N}\cos k_z(z_l(0))\right)^2 \right. \\ &\quad \left. + \left(\sum_{l=1}^{N}\sin k_z(z_l(t)) - \sum_{l=1}^{N}\sin k_z(z_l(0))\right)^2 \right\rangle. \end{aligned} \tag{9.15}$$

This form is very convenient in simulations, since only single sums over particles occur. Only two summations have to be evaluated per time frame (and per k-value), just like with the Green-Kubo form of *Chapter 8*.

9.4 Results

We carried out canonical and microcanonical simulations to calculate self and corrected diffusivities of argon in $AlPO_4$-5. All simulations started after 20 ps of equilibration and production runs ran 50 ns for the smallest box (5 unit cells), 40 ns for the 10 unit cell box, and 20 ns for all others.

First, single-particle mean square displacements were calculated up to correlation times of 1 ns and self-diffusion coefficients were calculated from a fit over 0.1 to 1 ns of correlation time. In all cases the mean square displacement curves were first averaged over 10 independent runs. Next, we calculated corrected diffusivities, both from Eq. 9.8 (i.e., from the mean square displacement of the center of mass), and from Eq. 9.15 (i.e., k-dependent diffusivities for different k-values). In Fig. 9.1 we have plotted the center-of-mass motion in a system of 60 unit cells z-length. Given the slow fluctuations on the timescale of the simulation, it is clearly necessary to run the simulations for several tens of nanoseconds in order to obtain

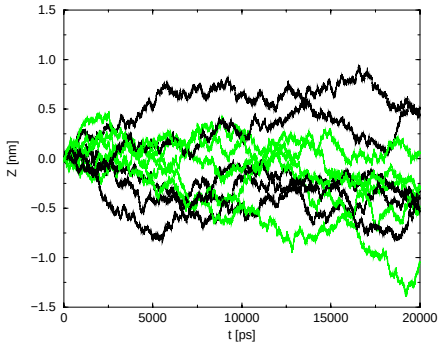

Figure 9.1: Center-of-mass motion in a system with a length of 60 unit cells, containing 180 argon atoms.

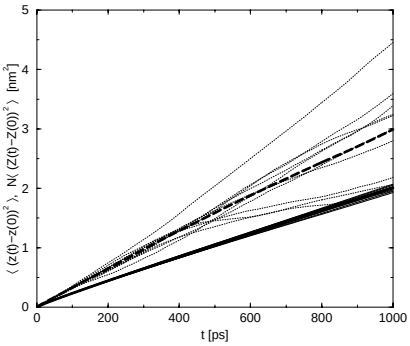

Figure 9.2: Mean square displacements of individual particles (solid lines) and of the center of mass (dashed lines) in a system of 60 unit cells. Shown are the lines of 10 independent runs and their averages (thick lines).

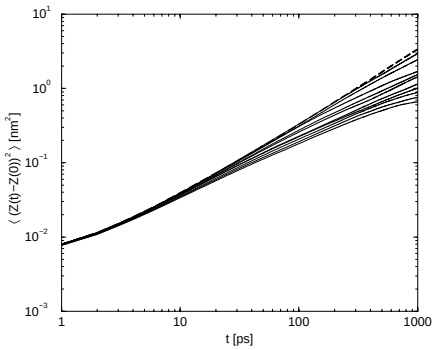

Figure 9.3: Mean square displacement of the center of mass, Eq. 9.8 (dashed line) and right-hand side of Eq. 9.15 (without d/dt), for the first 10 k-values (from top to bottom). All results for a box size of 60 unit cells in the pore direction.

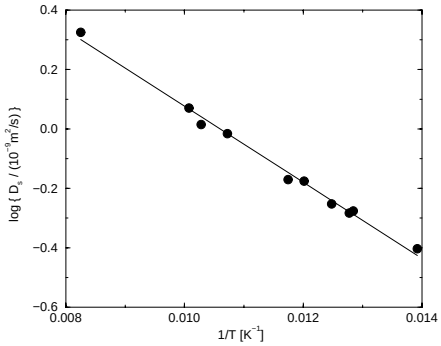

Figure 9.4: Dependence of measured self-diffusion coefficients on the average temperature in a system of 5 unit cells length. The drawn line represents an Arrhenius fit.

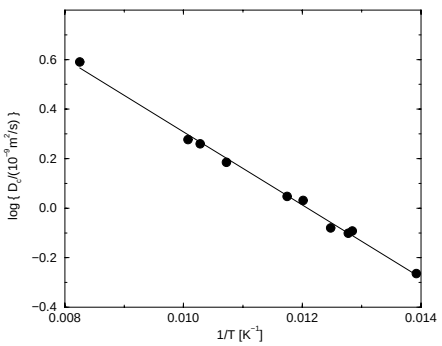

Figure 9.5: Dependence of measured corrected diffusion coefficients on the average temperature in a system of 5 unit cells length. The drawn line represents an Arrhenius fit.

reliable correlation functions. The mean square displacements of the individual particles (averaged) and of the center of mass are plotted in Fig. 9.2. Since the first is a single-particle property (which can be measured N times in each frame) this leads to statistically much more accurate results than the latter (which gives only one number per frame). Similar behaviour can be seen in the Figures of Sanborn and Snurr [153], although they calculated correlation functions only up to 10 ps. We plotted the mean square displacement of the center of mass together with the right hand side of Eq. 9.15 (except for the d/dt factor) in Fig. 9.3. It is clearly seen that for the larger k-values, the expression levels off at large correlation times, as was anticipated in the previous section. It is also seen that for all curves, there is a subdiffusive regime up to ca. 10 ps, due to the difficulty of particle passings. For the extraction of diffusivities, we looked for a region where the linear regime has started, but where most k-dependent curves did not level off yet. We chose to take correlation times from 20 to 40 ps to calculate all our corrected diffusivities (both k-dependent and in the $k \to 0$ form). Note that this correlation time interval is about the same order as was used in the work of Sanborn and Snurr [153] (they used correlation times between 0 and 10 ps).

In order to check the reliability of our results, we repeated all simulations in the microcanonical ensemble (except for the largest box size), which should give the same average results. The microcanonical runs were started with the end configurations of the canonical simulations. Since now the system was not thermostatted, every different run settled at a different temperature and the mean square displacements could not be averaged right away. Therefore we calculated the mean square displacements from the individual runs as well as the average temperatures. It is a well-known fact that diffusion in zeolites is an activated process (see *Chapter 6*), so the temperature dependent diffusion coefficients could be fitted to an Arrhenius law. Two examples are shown in Figs. 9.4 and 9.5.

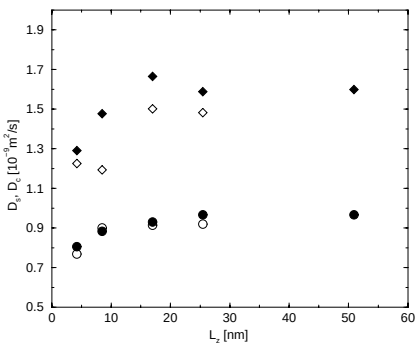

Figure 9.6: Self-diffusivities (circles) and corrected diffusivities (diamonds) as a function of system size in both canonical (closed symbols) and microcanonical simulations.

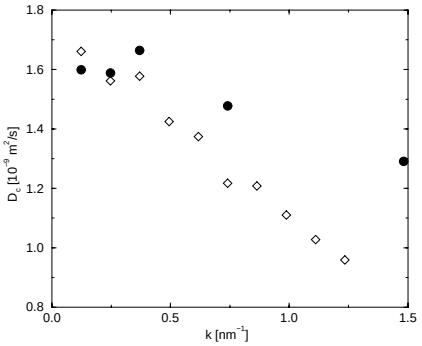

Figure 9.7: Corrected diffusivities vs. wavenumber (open symbols) from Eq. 9.15 for a system of 180 particles in 60 unit cells. For comparison, the results of Eq. 9.8 for different box sizes are also shown (closed symbols).

Final results for the self and corrected diffusivity for all box sizes are plotted in Fig. 9.6. As can be seen, the corrected diffusivities depend substantially on the box size, whereas the self-diffusion coefficients are nearly independent. For the self-diffusion, the NVT and NVE simulations give virtually the same results, and for the corrected diffusivities agree within the accuracy limits as well.

The results here are considerably larger for both diffusivities than the results in *Chapter 8* (Cf. Fig. 8.6). This is probably due to problems with the thermostat that we experienced in the previous study. There we used the Berendsen thermostat, which can give rise to an exponential increase of the center-of-mass motion in small systems [120]. That is why we removed the kinetic energy of the center of mass after every timestep. Although this is admissible in bulk systems, where the total momentum should be conserved, it is not strictly allowed when an external field (in this case provided by the zeolite lattice) is present. In fact, if the center-of-mass motion would be totally constrained (instead of stopping it *after* each step), Eq. 9.8 would give a corrected diffusivity of zero. We therefore believe that the present results are more reliable.

We now turn to our wavevector dependent formula for $D_c(k_z)$, Eq. 9.15. We calculated this quantity for 10 different k-vectors in our largest system. Again, averages were taken over 10 independent NVT simulations of 20 ns each. The results can be found in Fig. 9.7. The data show the same general trend as was seen in Fig. 8.6. For comparison, we have also plotted the results of Eq. 9.8 for all box sizes. With each box size we associated a wavevector of $2\pi/L_z$. It can be seen that for small values of k_z, both methods show the same limiting behaviour. Upon extrapolation to $k \to 0$, both methods would give approximately the same result. We

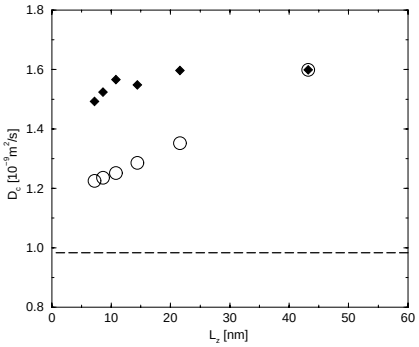

Figure 9.8: Diffusion coefficients for different control volumes in a system with a total length of 60 unit cells ($= 50.901$ nm). The circles denote the results from the center-of-mass displacement of molecules initially located in the control volume and the pyramids show the results from the displacement of only that material that is located in the box at any time (Eq. 9.9).

can conclude from this that although Eq. 9.8 is computationally simple and effective, it will only give the correct result for large enough box sizes, as was expected. Our wavevector dependent form, when applied to only one box size, has the advantage of giving results for a whole range of k-values which can be readily extrapolated to the macroscopic limit. This possibility is lost when Eq. 9.8 is used.

9.4.1 Center-of-mass motion

Despite the simplicity and efficiency of Eq. 9.8, one has to be careful not to misinterpret its meaning. Unlike the mean square displacement of tagged particles, which can be measured from the motion of a single particle, or as an average over several, the mean square displacement of the center of mass cannot be evaluated for an arbitrary part of the box. In fact, the expression is only valid when the whole box is taken into account and its correctness is entirely due to the periodicity of the system. It might be tempting to interpret this as the following Gedanken-experiment. Consider the infinite channel of all periodic images. Now at time zero, give all the particles in the central box a colour distinct from all their images. The (transport) diffusion coefficient could then be measured from the evolution of the distribution of coloured partcles, but again if and only if the motions of all the others are exactly correlated with the coloured ones.

To show this in the simulations, we calculated the mean square displacement of the center of mass of a subcollection of the molecules in the large box. We did this with half the number of particles (giving two experiments that can be averaged per simulation), the total number divided by three, $N/4$, $N/5$, and $N/6$. The resulting diffusion coefficients are plotted in Fig. 9.8. Although the considered particles may start out as a collective, they soon become (at least partially) uncorrelated. In the limit of a control volume of the size of one particle, it comes down to a calculation of the self-diffusion. As a reference, the self-diffusion coefficient is also represented in the plot. Indeed the results indicate that the results tend to the self-diffusion.

We also investigated the behaviour of Eq. 9.8, but now with $Z(t) - Z(0)$ calculated as in Eq. 9.9. The results of this are displayed as the filled symbols in the same figure. Clearly, these results are much more stable, although they also eventually decrease as the control

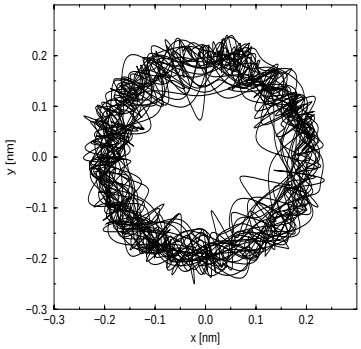

Figure 9.9: Trajectory of an individiual particle over 20 ps, projected on the x,y-plane.

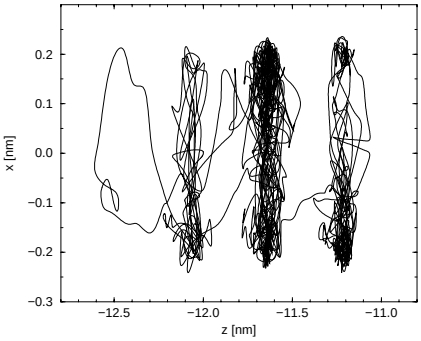

Figure 9.10: Trajectory of an individiual particle over 20 ps, projected on the z,x-plane.

volume becomes too small.

9.4.2 Jump-like diffusion

Although molecular dynamics simulations have proven very succesful in the study of transport in zeolites, much use is still been made of models of particles hopping on discrete lattices. In *Chapter 7* we used a lattice model to reach long time and length scales, and in one of the early simulations of transport diffusion [40], also lattice models were used. This is common practice for instance in the Maxwell-Stefan approach.

It is sometimes argued that the idea of particles hopping from one discrete site to the other, and staying at those sites for a while in between the hops, could not be a very accurate description for neutral molecules in fairly large pores. This objection might also apply to argon in $AlPO_4$-5, which is considered to be a large-pore zeolite. In Figs. 9.9 and 9.10 we plotted a short trajectory of a single particle in our system. Clearly the particle stays for a relatively long while in the vicinity of one oxygen ring, and then hops very fast to another. It is thus seen that the hopping picture applies perfectly well to this particular system, despite the fact that only van der Waals interactions play a role and the guest molecules are relatively small with respect to the pore size.

From the *xy*-plot it can be seen that the particle remains at the pore edge all of the time, i.e., including during the time of a hopping event. Since the hopping events seen in the *zx*-plot are all tilted in projection on the *xz*-plane, this must mean that the particle that travels from ring to ring follows a screw-like path. This is not surprising, since the six rings of oxygen that act as adsorption sites are rotated 30 degrees with respect to one another. The hopping event at the right of the figure thus probably reflects a hop to the nearest oxygen at the other rings. The crossing in the middle of the figure at the bottom half then represents a crossing

to the next nearest oxygen at the other ring.

9.5 Conclusions

In this chapter we have investigated various methods to calculate (corrected) collective diffusion coefficients. One way to arrive at an equation to calculate collective diffusion coefficients is to invoke Onsager's regression hypothesis [24, 36] and to model the decay of a long-wavelength microscopic density fluctuation by the corresponding phenomenological law, i.e., Fick's law of transport diffusion. This directly yieds Eq. 9.10 which we subsequently manipulated into Eq. 9.13. In the spirit of the derivation, the particles and their positions occurring in this equation must be restricted to those of the control volume. In case the control volume is all of the periodic simulation box, and k_z is one of the reciprocal lattice vectors of this box, one may just as well use the unfolded particle co-ordinates. In the thermodynamic limit of an infinite box, this distinction does not exist anymore.

The usual practice in the literature is to first take the thermodynamic limit, leading to Eq. 9.8, and next to sample this equation with a finite periodic box. The variable $Z(t)$ in this equation is then taken to be the center-of-mass position of the unfolded trajectories. We have shown in this chapter that this is only true in case the control volume is taken to be the whole periodic box. In all other cases $Z(t)$ should be interpreted as in Eq. 9.9. Secondly, we have shown that the final result depends on the size of the box; this holds for our Puritan method based on Eq. 9.13 as well as for the usual more Cavalier method based on Eq. 9.8. The advantage of our method is that by calculating the diffusion coefficients for several values of k_z, we can judge if our box size was large enough, and if necessary estimate the infinite-box-size value by extrapolation.

9.A Appendix. Grid-evaluation of sorbate-zeolite interactions

Over the course of the years, it has become generally established that, at least for sorbate molecules that are relatively small compared to the pore diameter, the diffusive motion of guest molecules inside zeolitic channels is hardly affected by lattice vibrations (see e.g., Fritzsche *et al.* [64] or Kopelevich and Chang [114]). If the zeolite framework is considered stiff, the lattice atoms can be excluded from the dynamics, thus saving much computational cost. Even more time is saved when the sorbate-zeolite interactions are pretabulated on a structured grid and subsequently interpolated during the actual simulations. This method was introduced in 1990 by June *et al.* [101, 102].

For an interpolation scheme to be applicable in such a simulation, the most important requirement is that no discontinuities in the forces occur upon crossing the boundaries of grid cells, and that the force field is rotation free. One method that always ensures smooth interpolating functions is spline interpolation [119]. A three-dimensional cubic spline, however, would require a full interpolation over the whole domain for every sorbate molecule at each timestep. For any reasonable grid size, this would make the calculation more expensive than

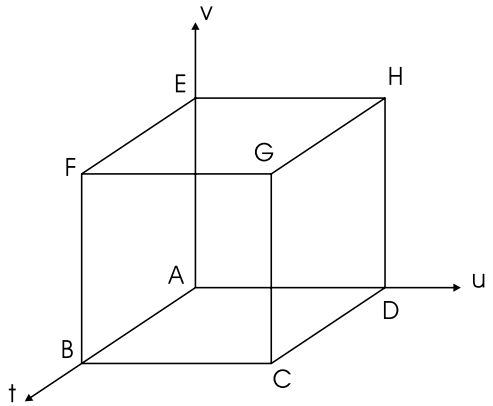

Figure 9.11: Definition of the grid cell as used in the interpolation schemes.

a direct evaluation of the atomic interactions. This problem could be partially overcome by performing a series of one-dimensional splines in the three directions, but the cost would still be comparatively high. Besides that, in the latter approach the continuity of derivatives across cell boundaries in the direction perpendicular to the spline would not be guaranteed.

The only way of arriving at a cost-effective interpolation is to use local methods, where the forces on (and/or the potential energy of) a sorbate molecule is derived from function values at neighbouring grid points. In *Chapter 7*, we applied such a method. After pretabulating the forces in *x*-, *y*-, and *z*-direction on each grid point, we calculated the actual force on a sorbate molecule by trilinear interpolation. (Trilinear interpolation over the energy was also used in order to calculate the sorbate's potential energy, but that does not play a role in the dynamics.) Trilinear interpolation is the three-dimensional variant of the so-called 'lever rule'. Using the eight nearest grid points of a particle (i.e., the corners of the grid cell in which it is located), one searches for a function

$$f(t,u) = \sum_{i=1}^{2}\sum_{j=1}^{2}\sum_{k=1}^{2} c_{ijk}\, t^{i-1} u^{j-1} v^{k-1}, \tag{9.A.1}$$

where t, u, and v are the fractional co-ordinates within the grid cell: $t = (x - x^A)/\Delta_x$, $u = (y - y^A)/\Delta_y$, and $v = (z - z^A)/\Delta_z$. For the rest of this appendix we will assume a cubic grid cell ($\Delta_x = \Delta_y = \Delta_z$), with the corners named as in Fig. 9.11.

In order to ensure continuity of the function (not its derivatives) across cell boundaries, eight conditions are specified:

$$\begin{aligned} &f(0,0,0) = f^A, \quad f(1,0,0) = f^B, \quad f(1,1,0) = f^C, \quad f(0,1,0) = f^D, \\ &f(0,0,1) = f^E, \quad f(1,0,1) = f^F, \quad f(1,1,1) = f^G, \quad f(0,1,1) = f^H, \end{aligned} \tag{9.A.2}$$

and by inversion one finds the coefficients c_{ijk}:

$$\begin{aligned} f(t,u,v) = {} & (1-t)(1-u)(1-v) f^A + t(1-u)(1-v) f^B \\ & + tu(1-v) f^C + (1-t)u(1-v) f^D \\ & + (1-t)(1-u)v f^E + t(1-u)v f^F \\ & + tuv f^G + (1-t)uv f^H. \end{aligned} \tag{9.A.3}$$

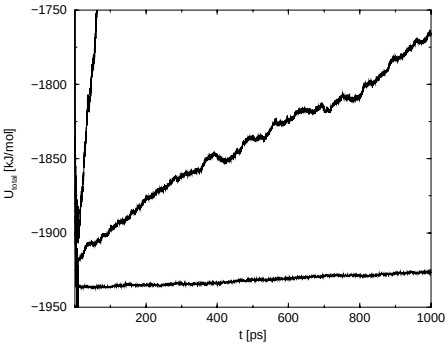

Figure 9.12: Total energy in an NVE simulation of 180 Ar molecules in a pore system of 60 unit cells by employing trilinear interpolation over pretabulated forces. Shown are grid spacings 0.4 Å (top line), 0.2 Å (middle line), and 0.1 Å (bottom line). The first 10 ps. represent equilibration at NVT with rigid temperature scaling at every step.

Thus a simulation with trilinear interpolation over the force field (such as we performed in *Chapter 7*) requires the storage of F_x, F_y, and F_z on each grid point (and U as well if one wishes to calculate energies).

The accuracy of the above method can be checked by performing a simulation at constant N, V, and E and monitoring how well total energy is conserved. The results of this for various grid spacings are displayed in Fig. 9.12. The figure clearly shows a nearly monotonous increase in the energy for all grid spacings. We suggest the following cause for this: differentiating F_x with respect to y yields a different answer from differentiating F_y with respect to x. This implies that no conservative field can be associated with the proposed force interpolations. In other words, at every force evaluation a small error is made compared to the force that would belong to the real underlying (conservative) potential energy field. This adds a small (quasi-random) error to the particle's velocity. Since the (kinetic) energy depends quadratically on the particle velocities, this leads to a 'diffusion' of the total energy (or, more precisely, of the mean square deviations of the velocities).

One way to reduce the errors in the force evaluations could be to incorporate more grid points in the interpolation scheme. This would result in better estimates of the higher order derivatives. (Cf. the three-, four- or five-point schemes for numerical approximation of one-dimensional derivatives). We extended our 8-point scheme to a 27-point and a 64-point scheme, respectively, but in both cases the results were hardly improved. This may not be surprising, since for any crossing of a cell boundary, the scheme switches to a new interpolating function (because a new set of grid points have become the nearest ones). Consequently, no matter how many extra grid points are taken into account, the derivative of the interpolating function will always be discontinuous. Only the continuity of the function itself is ensured, since the function values of the incorporated grid points are taken as constraints in the construction of the scheme. The only way to attain higher order smoothness is to stick to the eight nearest grid points but supply besides the function values, also first (and/or higher order) derivatives as constraints.

A systematic study of local interpolation schemes with the above strategy has been described by Russell [149]. He compared several schemes (all in two dimensions) of various

orders focussing on the continuity across cell boundaries. He reported that bicubic interpolation is the lowest order two-dimensional interpolation procedure which maintains the continuity of the function and its first derivatives both in the normal and tangential directions.

We will now derive the equations for tricubic interpolation over the potential energy field (thus ensuring continuity of the forces). Note that the one-dimensional analogue of tricubic interpolation is called 'Hermite interpolation'. Here the function and its derivatives are defined at two grid points, whereas standard cubic interpolation requires function values at four interpolation points (but does not, for the same arguments as above, lead to a continuous derivative distribution). Tricubic Hermite interpolation was also used in the second study of June *et al.* [102] (in their first study they used three-dimensional spline interpolation [101]).

We now search for a function:

$$U(t,u,v) = \sum_{i=1}^{4}\sum_{j=1}^{4}\sum_{k=1}^{4} c_{ijk} t^{i-1} u^{j-1} v^{k-1}, \tag{9.A.4}$$

with 64 unknown coefficients c_{ijk}. With 8 grid points, we are allowed to specify 8 constraints at each grid point. For this we chose U, $(\partial U/\partial t)$, $(\partial U/\partial u)$, $(\partial U/\partial v)$, $(\partial^2 U/\partial u \partial t)$, $(\partial^2 U/\partial v \partial t)$, $(\partial^2 U/\partial v \partial u)$, and $(\partial^3 U/\partial v \partial u \partial t)$. The resulting set of equations can in short be written as

$$\mathbf{Bc} = \mathbf{f}, \tag{9.A.5}$$

where the vector $\mathbf{f}$ contains all constraint values $(\partial U/\partial t)^A, (\partial U/\partial t)^B, \ldots (\partial U/\partial u)^A, \ldots$, etc. in one column and the vector $\mathbf{c}$ contains all coefficients c_{ijk}. The 64×64-matrix $\mathbf{B}$ can then be inverted to give the coefficients:

$$\mathbf{c} = \mathbf{B}^{-1}\mathbf{f}. \tag{9.A.6}$$

The resulting matrix $\mathbf{B}^{-1}$ is given on page 128.

We find the forces on the particles by differentiation of Eq. 9.A.4. As a result of this $(\partial^2 U/\partial\alpha\partial\beta)$ is always equal to $(\partial^2 U/\partial\beta\partial\alpha)$, which ensures that we have a consistent set of F_x, F_y and F_z associated with a conservative field. Note that continuity across cell boundaries of only the 8 imposed constraints is ensured. Derivatives of the forces parallel to their directions (e.g., $(\partial F_x/\partial x) = (\partial^2 U/\partial x^2)$) and higher order derivatives will be discontinuous. It is therefore not advantageous to go beyond the standard Verlet integration scheme with for example a high order Gear predictor-corrector (like is done for instance in the work of Sanborn and Snurr [153]), since the predictor relies upon the continuity of higher order derivatives.

Results for NVE simulations with the same grid spacings as in Fig. 9.12 but now with tricubic interpolation over the potential energy field are given in Fig. 9.13. Clearly, the energy is now perfectly conserved for all grid spacings. No discernible trend was found over 1 ns of simulation time and for all grid spacings the root mean square deviation of the energy amounted to 0.03 kJ/mol. The difference between the energy levels in Fig. 9.13 is almost entirely due to the NVT equilibration period, where energy is not conserved and thus develops differently in the three runs due to deviations of the particle trajectories. When the interpolation routine with the three different grid spacings were applied to a single configuration, the energies differed by 1 promille maximum.

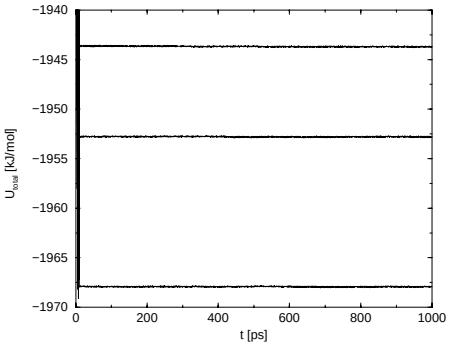

Figure 9.13: Total energy in an NVE simulation of 180 Ar molecules in a pore system of 60 unit cells by employing tricubic interpolation over pretabulated energies. Shown are grid spacings 0.4 Å (top line), 0.2 Å (middle line), and 0.1 Å (bottom line). The first 10 ps. represent equilibration at NVT with rigid temperature scaling at every step.

In most present-day mainframes, storage of large amounts of numbers in memory is not a problem. For our present application, the narrowest grid leads to a memory allocation for the pretabulated grid of ca. 350 Mb (compared to 45 Mb for a spacing of 0.2 Å and 6 Mb for a spacing of 0.4 Å). Given the fact that the simulation time is hardly affected by these memory sizes, we decided to use a grid spacing of 0.1 Å throughout our simulations, since those results would be closest to a direct evaluation of sorbate-zeolite interactions.

The matrix $\mathbf{B}^{-1}$:

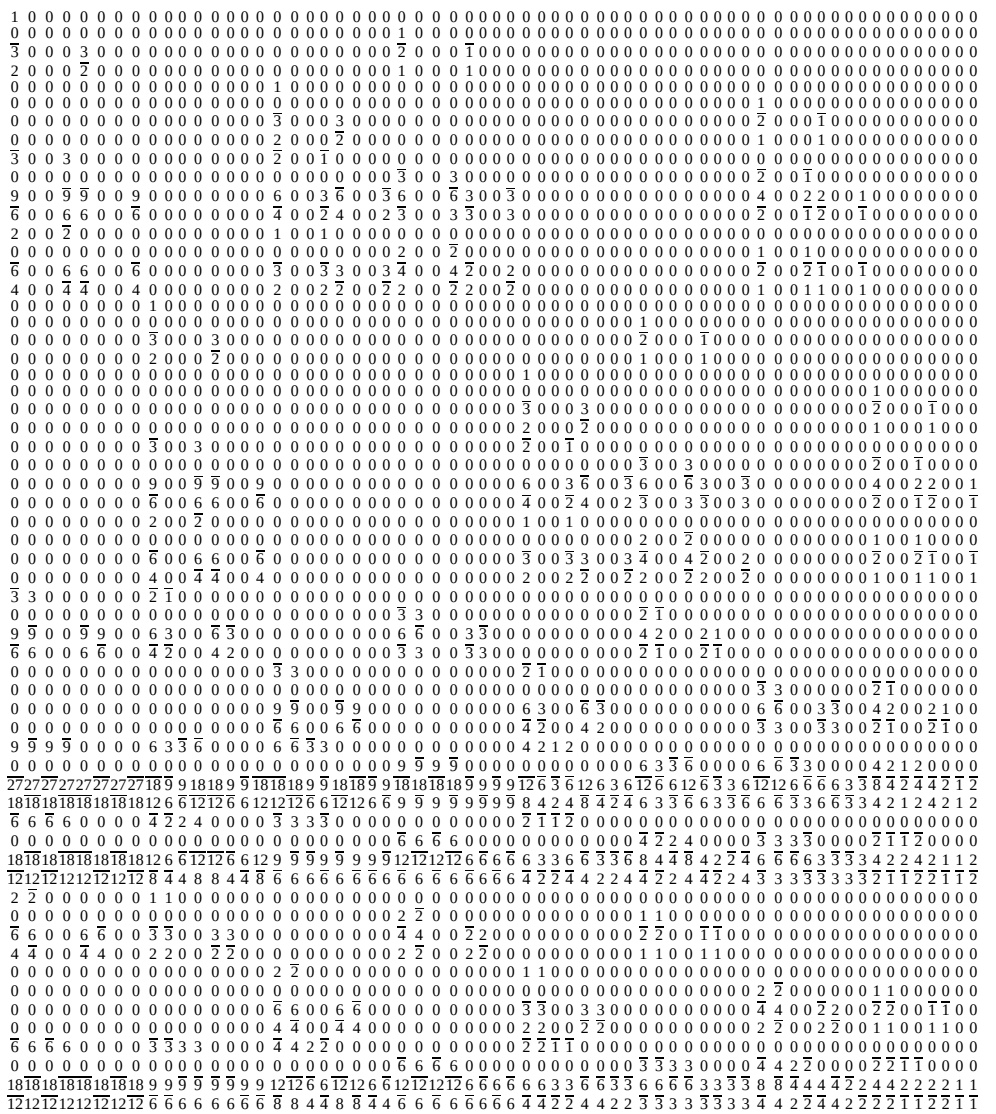

Part IV

Postludium

Summary

The research described in this thesis consists of two topics: simulation of the growth of atomic crystals on the one hand, of the motion of guest molecules through porous crystals (zeolites) on the other. Though seemingly unrelated, they share an important feature: in both cases, their macroscopic behaviour is primarily governed by processes on the molecular scale. In crystal growth, the macroscopic form of the crystal is determined by molecular motions at the interfaces and in zeolitic diffusion, the transport of gases through the material is governed by microscopic resistances felt by the molecules in the pores. A second common property of the two systems is their difficult experimental accessibility. This is both caused by the small scale (the zeolitic pores we describe have a diameter between 0.7 and 1 nm) and by the fact that the region of interest lies between two dense phases (liquid and crystal), which limits the use of light probes of any kind.

Because of the experimental difficulties, most measurements concern collective or average properties: the growth rate of a whole crystal surface or the collective diffusion coefficient in zeolites (measured by so-called 'uptake' experiments). Since the late 1970's, some microscopic experiments have been developed as well to measure diffusion coefficients in zeolites: Pulsed-Field Gradient Nuclear Magnetic Resonance (PFG-NMR), Quasi-elastic Neutron Scattering (QENS), and very recently, interference microscopy.

Molecular Dynamics (MD) simulations nowadays provide an important tool in testing theories that try to explain macroscopic behaviour from microscopic models. They can also help linking the results of the above-mentioned microscopic and macroscopic experiments. In MD, the equations of motion for a large collection of molecules are solved numerically. Because there is essentially no limit to the complexity of the used models, several assumptions that are necessary in analytical theories can be tested directly.

Throughout this thesis we have used MD simulations to study the microscopic processes that govern the macroscopic phenomena in both our systems. Our special focus is on the extrapolation of simulation results to the macroscopic scale of experiments. In the remaining two sections, we will describe the results of our research on both topics separately.

Growth of a Lennard-Jones crystal from the melt

The macroscopic form of a crystal represents its growth history: different forms evolve under different experimental conditions. The physico-chemical circumstances determine the growth rates of the individual crystal surfaces and the resulting form is bounded by the slowest growing faces. Understanding, predicting, or possibly even designing the forms of crystals is of tremendous importance in both science and technology. The production process of almost any solid material involves at least one crystallization step and the transport (pumping) properties of liquids containing small crystallites are mainly determined by the form of the crystallites.

As a first step in the prediction of growth morphologies, we study in this thesis the growth rates of 1 surface of a Lennard-Jones crystal. In particular, we focus on the temperature dependence of growth (and melting) rates close to the equilibrium temperature. All simulations initially consist of a separate simulation of a bulk liquid and a bulk crystal, which are subsequently combined to give a two-phase system. To monitor the amount of crystalline material throughout the two-phase simulations, we introduce a mathematical formula that allows us to classify particles as 'liquid-like' or 'solid-like'.

Growth and melting rates can be measured by (nonequilibrium) constant pressure simulations at different temperatures. The lengths of these simulations are, however, limited to the time over which the whole simulation box becomes crystalline (or liquid). Therefore we present an alternative method in *Chapter 2*: we measure the decay of spontaneous fluctuations of the amount of solid material in an equilibrium simulation (at constant volume) and therefrom extract the same kinetic coefficient as from the nonequilibrium simulations. We enhance the accuracy of both methods in subsequent chapters, to make a more quantitative comparison possible. In *Chapter 3* we show that in order to measure consistent growth and melting rates in nonequilibrium simulations, it is crucial to incorporate the correct number of 'lattice imperfections' (small but noticeable disorder) in the crystalline phase. This is ensured in *Chapter 4*, where we start all nonequilibrium simulations with extensive equilibration at the melting point. By performing the most accurate simulations to date of this system, we discover two linear regimes: a short-time regime which is associated with the relaxation of the interface from its equilibrium shape to its steady-state nonequilibrium shape, and a long-time regime which is associated with macroscopic growth (or melting). From the long-time rates we find a linear temperature dependence with no slope discontinuity at the melting point. This behaviour was already postulated in the 1920's, but has raised some debate in the literature due to contradicting results from simulations. We infer from our findings that such deviations must be due to improper equilibration of the system or to the use of too short observation times.

With a properly equilibrated system of a large enough size, we repeat our equilibrium method at the melting point found from the nonequilibrium simulations. From this we find two different regimes as well, the kinetic coefficients of which agree quantatively with the results from the preceding chapters.

Transport of methane and argon in the zeolite $AlPO_4$-5

Zeolites are crystals with a well-defined pore system of nanometer scale. Their pores can selectively adsorb or release molecules or ions, giving zeolites a tremendous industrial potential. They are widely used as catalysts, ion-exchangers, molecular sieves, drying agents, and many more. In almost all applications the transport of guest molecules through the pores plays a crucial role. In this thesis we focus on the diffusion of methane and argon through the zeolite $AlPO_4$-5, which has an internal structure of one-dimensional, non-interconnected pores.

In *Chapter 7* we study the self-diffusion of methane in $AlPO_4$-5. The size of methane molecules is such that they are just able to pass each other in the pores. We find that the

mean square displacement of the particles scales with the correlation time to the power of 0.6, just above the theoretical value of 0.5 for particles that cannot pass at all (single-file diffusion). On the long timescale, however, the infrequent passages of the particles dominate the dynamics. By switching over to a coarse-grained hopping model (with parameters taken from the atomistic simulations), we get access to this timescale as well. In that regime, we find normal diffusion and are able to calculate the self-diffusion coefficient.

Most practical applications of zeolites involve the transport of molecules under nonequilibrium conditions. This is not governed by self-diffusion but by transport diffusion. The purpose of *Chapters 8 and 9* is the calculation of the transport diffusion coefficient. To avoid the complications of anomalous diffusion, we study the transport of argon molecules, which are smaller than methane molecules. For the same reason as with the crystal growth simulations, we seek a method to calculate the nonequilibrium property from equilibrium simulations. In this case we measure the transport diffusion coefficient from the decay of spontaneous fluctuations of density waves in the system. In *Chapter 8* we present a Green-Kubo expression that depends explicitly on the wavelength of the density waves. From the dependence of the diffusion coefficient on the wavelength, we can pinpoint the onset of the linear response regime. These results set a lower limit to the length of the simulation system to be used in both equilibrium and nonequilibrium simulations.

We elaborate a little further on this in *Chapter 9*, where we compare our wavelength-dependent results with the results for different system sizes from an expression in which the limit to infinite wavelengths has already been taken. We find that the box size dependence of the latter expression is similar to the wavelength dependence of our results. This is not surprising because, although the limit is taken to infinite wavelengths analytically, the maximum wave that is probed by the system is the one that is commensurate to the boxlength. We also demonstrate that the usual Einstein expression for transport diffusion (in which the diffusion coefficient is calculated from the mean square displacement of the center of mass of the adsorbed species), is only valid in periodic systems and only if the whole box is taken as control volume.

Samenvatting in het Nederlands

Het onderzoek dat in dit proefschrift wordt beschreven is tweeledig: het betreft het modelleren van enerzijds de groei van atomaire kristallen en anderzijds de beweging van gastmoleculen door poreuze kristallen (zeolieten). Hoewel deze onderwerpen op het eerste gezicht weinig verwant lijken is er toch een sterke overeenkomst: in beide gevallen worden processen beschreven waarbij de macroscopische (met het blote oog waarneembare) verschijnselen in sterke mate beheerst worden door datgene wat zich op moleculaire schaal afspeelt; een kleine verandering of oneffenheid op het niveau van de moleculen kan een grote verandering in het macroscopische gedrag tot gevolg hebben. Een andere overeenkomst tussen beide systemen is dat zij experimenteel moeilijk toegankelijk zijn. De zeolietkanaaltjes uit dit proefschrift hebben een diameter die varieert tussen 0.7 en 1 nanometer (1 miljoenste deel van een millimeter). Op deze schaal is het onmogelijk bijvoorbeeld een ingenieuze camera door het kanaal te laten meebewegen om te kijken hoe het transport van moleculen in zijn werk gaat, zoals dat bijvoorbeeld wel kan in de medische wereld als de stroming in een bloedvat bestudeerd moet worden. De interessante processen in de kristalgroei vinden plaats aan het grensvlak van het kristal met de vloeistof en dit grensvlak is op zijn hoogst ook enkele nanometers dik. Er zijn tegenwoordig wel zeer geavanceerde microscopen beschikbaar waarmee bijvoorbeeld het oppervlak van een siliciumkristal tot op atomaire precisie kan worden bestudeerd, maar deze en andere technieken zijn alleen toepasbaar bij kristaloppervlakken in contact met een gasfase. Bij een kristal dat uit de smelt groeit bevindt het grensvlak zich tussen twee dichte fasen, wat een grote experimentele belemmering oplevert. In ons systeem is het dichtheidsverschil tussen het kristal en de vloeistof zelfs slechts 13.5 procent (hoewel de wijnkenner dit een stevig percentage zal vinden, betekent het voor ons een miniem verschil).

Dat de experimenten niet tot op moleculaire schaal kunnen doordringen, wil niet zeggen dat er aan deze systemen helemaal niet gemeten kan worden. Zo is het in bepaalde gevallen wel mogelijk om het voortschrijden van een heel kristalvlak door de smelt te volgen en daarmee de groeisnelheid van dat specifieke vlak te meten. Met moderne NMR-technieken kunnen diffusiecoëfficiënten in zeolieten worden gemeten. Deze geven de gemiddelde verplaatsing van moleculen per tijdseenheid weer. Ook kan met een zogenaamd ‘uptake’-experiment worden gekeken hoeveel materiaal er in een bepaald tijdsbestek door het zeoliet wordt opgenomen. Om een beter begrip te krijgen van de uitkomsten van dergelijke experimenten, zijn er in de loop der jaren tal van theorieën ontwikkeld die macroscopische verschijnselen verklaren op basis van een microscopisch beeld van de werkelijkheid. De voorspellingen die met die theorieën worden gedaan kunnen experimenteel getest worden, waarna het microscopische beeld kan worden bijgesteld of verfijnd. Om analytisch hanteerbaar te blijven, mogen de modellen niet te gecompliceerd worden, of moeten aannames worden gedaan waarvan de implicaties niet altijd te overzien zijn.

Sinds de jaren ’60 is er een nieuwe manier bijgekomen om inzicht in moleculaire processen te krijgen, namelijk computersimulaties. Hoewel er verschillende mogelijkheden zijn,

hebben we in het in dit proefschrift beschreven onderzoek uitsluitend gebruik gemaakt van Moleculaire Dynamica-simulaties (MD). Uitgaande van een bepaald interactiemodel tussen de moleculen worden de bewegingsvergelijkingen van Newton numeriek opgelost. Op elk moment worden de krachten tussen alle deeltjes bepaald en daarmee worden hun posities en snelheden op een iets later tijdstip berekend. Dan worden opnieuw de krachten bepaald en zo wordt geleidelijk de hele dynamica opgebouwd. Een van de voordelen van deze methode is dat de interactiemodellen zeer gedetailleerd gemaakt kunnen worden. Omdat het systeem numeriek (stapje voor stapje) wordt doorgerekend hoeven er niet allerlei aannames te worden gedaan die voor een analytische behandeling wel noodzakelijk zijn. Een ander groot voordeel is dat elk deeltje afzonderlijk in de tijd kan worden gevolgd en dat daarmee alle moleculaire informatie voorhanden is. Uit het tijdgemiddelde gedrag kunnen bovendien grootheden worden uitgerekend die wel experimenteel kunnen worden gemeten (zoals bijvoorbeeld kristalgroeisnelheden of diffusiecoëfficiënten). Door de resultaten van experimenten en simulaties te vergelijken kunnen de modellen worden verbeterd en de modelparameters worden geoptimaliseerd.

We zullen nu in het kort beschrijven wat de resultaten zijn geweest van ons onderzoek aan kristalgroei en in de daaropvolgende sectie zullen we de uitkomsten van het onderzoek aan diffusie in zeolieten behandelen.

Groei van een Lennard-Jones kristal vanuit de smelt

Iedereen die wel eens een mineraalkristal heeft gezien zal in de eerste plaats getroffen zijn door de perfect gladde oppervlakken en de symmetrische vormen. Deze vormen weerspiegelen de onderliggende microscopische structuur waarbij ieder atoom zijn thermodynamisch gunstigste plaats op een rooster heeft ingenomen. De uitwendige vorm van een kristal wordt echter ook in hoge mate bepaald door de omstandigheden waaronder het gegroeid is. Zo is het bevriezen van water in de lucht over het algemeen diffusie-gelimiteerd; de aanvoer van water kan het groeiproces niet bijhouden waardoor fractalachtige structuren (sneeuwkristallen) ontstaan. Wordt water echter langzaam vanuit de smelt bevroren dan kunnen gladde oppervlakken onstaan die een Elfstedentocht mogelijk maken. Behalve in de natuur, speelt kristalgroei ook in de industrie een belangrijke rol. In het productieproces van iedere vaste stof (variërend van computerchips tot medicijnen) komt wel ergens een kristallisatiestap voor. Het is dus van zowel wetenschappelijk als technologisch belang om fundamenteel inzicht te krijgen in de microscopische basis van kristalgroei.

De macroscopische vorm van een kristal wordt bepaald door de snelheid waarmee de verschillende kristalvlakken groeien; alleen de langzaamst groeiende vlakken zijn terug te vinden. Een voorspelling van de uitwendige vorm is dus mogelijk op basis van de groeisnelheden van de belangrijkste vlakken. Als een eerste stap op weg naar zo'n voorspelling beschouwen we in dit proefschrift de groeisnelheid van 1 vlak van een kristal bestaande uit zachte bollen. De interactiepotentiaal die we daarvoor gebruiken is goed in staat om de eigenschappen van edelgassen zoals argon te beschrijven. We bestuderen de temperatuurafhankelijkheid van de groeisnelheid zeer dicht bij het smeltpunt, wat bij argon gelijk staat aan 82 Kelvin (191 graden Celsius onder nul).

We beginnen steeds met het simuleren van een volume met vloeistof en een volume met kristal, in ons geval een vlakkengecentreerd kubisch (FCC) rooster. Na een tijdje worden beide systemen gecombineerd en rekenen we met het gehele systeem verder. Daarbij passen we voortdurend het volume zodanig aan dat de druk (gemiddeld) constant blijft. Bij een temperatuur onder het smeltpunt zal de vloeistof kristalliseren, erboven zal het kristal smelten. We hebben een wiskundige formule opgesteld waarmee we van elk deeltje kunnen zeggen of het tot de kristal- of tot de vloeistoffase behoort. Op deze manier kunnen we dus bij elke gewenste temperatuur de groei- of smeltsnelheid meten.

Er is echter een probleem: als het systeem een tijdje is aangegroeid (of gesmolten) raakt al snel een van beide fasen op, wat de maximale lengte van de simulaties drastisch beperkt. Dit effect is groter naarmate het systeem verder uit evenwicht is. Daarom introduceren we in *Hoofdstuk 2* een alternatieve methode: we simuleren het tweefasensysteem nu niet bij constante druk maar bij constant volume. Zo blijft het systeem van nature in evenwicht en is de lengte van de simulaties dus niet beperkt. Immers, als er spontaan wat materiaal kristalliseert zal de druk afnemen doordat het kristal een grotere dichtheid heeft. Door de lagere druk zal het smelten weer worden bevorderd, en vice versa. In *Hoofdstuk 2* leiden we een formule af waarmee we uit de fluctuaties van de hoeveelheid kristallijn materiaal dezelfde informatie kunnen halen als uit de simulaties bij constante druk.

In de volgende hoofdstukken verhogen we de nauwkeurigheid van beide metingen, te beginnen met de niet-evenwichtssimulaties. In *Hoofdstuk 3* onderzoeken we de invloed van de manier waarop het systeem wordt geprepareerd. Wanneer de vloeistof tegen het kristal wordt aangezet moet het systeem zich aan de nieuwe situatie aanpassen voordat het zich stabiel gedraagt. In dit hoofdstuk laten we zien dat de mate van wanorde in het kristal (de hoeveelheid deeltjes die een kleine afwijking ten opzichte van de ideale roosterpositie vertonen) cruciaal is om de goede snelheden te meten. Bevat het kristal minder wanorde dan er zou zijn in een reëel kristal bij die temperatuur, dan worden smeltsnelheden gemeten die te laag zijn ten opzichte van de gevonden groeisnelheden.

In *Hoofdstuk 4* doen we bij elke meting eerst een lange ‘equilibratie’ bij het smeltpunt voordat we de niet-evenwichtstemperatuur instellen. Tijdens de daaropvolgende metingen volgen we nauwkeurig de toename (of de afname) van de hoeveelheid kristallijn materiaal. Hierbij blijken twee regimes op te treden. Hoewel het systeem lang geëquilibreerd is bij het smeltpunt moet het grensvlak zich nog wat herstructureren als de temperatuur wordt veranderd: als de temperatuur wordt verlaagd is de stabiele vorm van het grensvlak smaller, bij een verhoging is deze breder. We vinden dus een initieel regime waarin het grensvlak zich aanpast aan de niet-evenwichtssituatie en een langetijds-regime van groeien of smelten. Door zeer nauwkeurig te middelen bij een voldoende groot systeem blijken we in staat de temperatuurafhankelijkheid van beide processen te bepalen. Het tweede regime blijkt daarbij een perfect rechte lijn op te leveren. Hoewel de wetenschapper Tammann dit al in de jaren ’20 voorspelde zijn in simulaties van verschillende groepen toch discontinuïteiten gevonden. Op grond van onze resultaten kunnen we het vermoeden uitspreken dat dergelijke afwijkingen van een rechte lijn toe te schrijven moeten zijn aan een onzorgvuldige preparatie van het systeem.

Nu we geleerd hebben hoe het systeem het best geprepareerd kan worden, welke grootte het ten minste moet hebben en we bovendien zeer nauwkeurig het smeltpunt bepaald hebben,

herhalen we in *Hoofdstuk 5* nogmaals de evenwichtsmethode. We brengen wat verfijningen aan in de formule en voorzien de afleiding van extra commentaar. De resultaten van een lange en zo nauwkeurig mogelijke evenwichtsmeting blijken ook twee regimes op te leveren die in overeenstemming zijn met de resultaten van de voorgaande hoofdstukken.

Transport van methaan en argon in het zeoliet $AlPO_4$-5

Zeolieten zijn kristallen die in hun structuur zeer goed gedefiniëerde kanaaltjes van moleculaire diameters bevatten. De ontdekking door de Zweed Cronstedt in 1756 dat zeolieten grote hoeveelheden water bevatten die ze bij verwarming weer vrijgeven, leidde (twee eeuwen later) tot talloze alledaagse en technologische toepassingen. Zo wordt van de wateruitwisseling gebruik gemaakt in vochtvangers (ter vervanging van silicagel), geurvreters, kattenbakkorrels en luchtdrogers. Door hun chemische structuur zijn zeolieten erg goede ionenuitwisselaars waardoor ze als waterontharders kunnen worden gebruikt (sinds het verbod op fosfaten bevat elk wasmiddel tegenwoordig zo'n 30 procent aan zeolieten). De grootte en de verschillende configuraties van de poriën maakt dat zeolieten uitgebreid ingezet worden als moleculaire zeven of specifieke katalysatoren, bijvoorbeeld in kraakreacties in de aardolieindustrie. Sinds in de loop van de vorige eeuw is aangetoond dat zeolietstructuren in allerlei gewenste samenstellingen vrij eenvoudig gesynthetiseerd kunnen worden, is het aantal toepassingsmogelijkheden exponentieel gegroeid.

Voor een goed gebruik van bestaande en een efficiënte synthese van nieuwe zeolieten is het van groot belang inzicht te hebben in de moleculaire transportmechanismen in de kanaaltjes. Ook hier kunnen simulaties veel inzicht verschaffen. Omdat de systemen in simulaties doorgaans veel kleiner zijn dan experimentele systemen, moet veel aandacht geschonken worden aan een juiste extrapolatie van de simulatieresultaten naar grote tijd- en lengteschalen, anders is een vergelijking met experimentele meetgegevens niet mogelijk.

In *Hoofdstuk 7* bestuderen we de zelfdiffusie van methaan in het zeoliet $AlPO_4$-5. Methaanmoleculen zijn zo groot dat ze elkaar zeer moeilijk kunnen passeren in de kanalen van het zeoliet. We meten dan ook een gemiddelde kwadratische verplaatsing die dicht in de buurt komt van het gedrag van deeltjes die elkaar helemaal niet kunnen passeren. Op zeer grote tijdschaal gaan echter de sporadische passages het diffusiegedrag overheersen. Om dit goed te bestuderen schakelen we over op een vereenvoudigd simulatiemodel waarvan we de parameters afstemmen op de gedetailleerde simulaties. Met het vereenvoudigde model komen we tot grote tijd- en lengteschalen en vinden we inderdaad normaal diffusief gedrag terug. Een discrepantie in de literatuur tussen verschillende experimenten kunnen we nu verklaren aan de hand van de verschillende tijdschalen waarop deze experimenten gebaseerd zijn.

De zelfdiffusiecoëfficiënt is een evenwichtsgrootheid. De meeste technologische processen vinden echter bij niet-evenwicht plaats. Het transport van moleculen onder invloed van een concentratiegradiënt wordt bepaald door de collectieve diffusiecoëfficiënt. Het berekenen van deze grootheid is de inzet van *Hoofdstuk 8*. Daar bestuderen we argon in $AlPO_4$-5. Omdat argonmoleculen iets kleiner zijn dan methaanmoleculen hebben we minder last van afwijkingen van normale diffusie. Om dezelfde reden als bij de kristalgroei proberen we ook

hier een niet-evenwichtsgrootheid uit te rekenen aan de hand van een simulatie bij evenwicht. Haalden we in *Hoofdstuk 5* de groeisnelheid uit fluctuaties van de hoeveelheid kristallijn materiaal, hier halen we de collectieve diffusiecoëfficiënt uit de fluctuaties van de dichtheid. Dat betekent dat we het, op atomaire schaal chaotisch bewegende, dichtheidsprofiel opgebouwd denken uit een heleboel golven. We bekijken het verval van dichtheidsgolven met verschillende golflengte en berekenen het verband tussen de gevonden coëfficiënt en de golflengte. Het gebied waar het resultaat niet meer van de golflengte afhangt kan geassocieerd worden met het zogenaamde regime van lineaire respons. Omdat de aanname van lineaire respons ten grondslag ligt aan alle niet-evenwichtsmethodes kan uit onze resultaten worden afgelezen hoe groot de systemen moeten zijn en hoe klein de gradiënten in het geval van niet-evenwichtsmetingen.

In *Hoofdstuk 9* beschouwen we een door anderen gebruikte formule waarin de extrapolatie naar oneindige golflengte (en dus impliciet oneindige systeemgrootte) vooraf is uitgevoerd. We tonen aan dat de resultaten met deze formule nog steeds van de systeemgrootte afhangen aangezien maximaal de langste golf die in het systeem past wordt bemonsterd. De resultaten voor grotere systemen zijn in overeenstemming met de resultaten van onze formule voor grote golflengtes.

Dankwoord

Dit proefschrift is het resultaat van ruim 4 jaar onderzoek. Vanzelfsprekend bestaat zo'n onderzoeksperiode uit de nodige toppen en dalen. Daarbij heb je zo nu en dan mensen nodig die je laten zien dat er ook in het dal genoeg moois te beleven is, of die je een mogelijke route naar de volgende top kunnen wijzen. Zonder daarbij iemand tekort te willen doen, wil ik op deze plaats enkele 'gidsen' bij naam noemen.

Allereerst mijn promotor, Wim Briels, die een enorm vermogen heeft het landschap te overzien en op cruciale momenten een verrassende doorsteek kan vinden. Wim, bedankt voor de mogelijkheden die je geboden hebt en voor het in mij gestelde vertrouwen. De vele discussies (soms tot in de kleine uurtjes) heb ik zeer gewaardeerd. Met name in het laatste jaar waarin onze creatieve ideetjes keer op keer werden ingehaald door nieuwe simulatieresultaten maar waaruit uiteindelijk toch een consistent beeld en veel inzicht naar voren is gekomen.

Vervolgens bedank ik de (oud-)leden van de leerstoel Computational Chemistry, die de afgelopen jaren de wetenschappelijke thuisbasis vormden: Marc Hulshof, mijn eerste kamergenoot, voor de gezelligheid, de vele computerhulp en de altijd aanwezige belangstelling; Reinier Akkermans, voor het altijd openstaan voor een vraag van welke aard dan ook en voor de vele gesprekken over onderwijs en webpagina's; Wouter den Otter, voor de talrijke discussies in de mensa en daarbuiten en voor de niet-aflatende inzet om dingen tot op de bodem uit te zoeken; en Johan Padding voor de hulpvaardigheid en het (soms ontembare) enthousiasme. Verder Martin, Dick, Frank, Nico, Bob, Roelof en Tanya voor de vele (koffietafel-)discussies, voor de (email-)ondersteuning en voor het lezen van (delen van) het manuscript.

Van de vele studenten die deel hebben uitgemaakt van de groep wil ik er twee met name noemen: Sonja Engels, die ik mocht begeleiden bij haar afstudeeropdracht en Jacob Hoogenboom, zonder wie Hoofdstuk 8 er nooit in deze vorm zou zijn geweest.

Om het op enig moment tot 'grootste rekenaar van Nederland' te kunnen schoppen is veel computerondersteuning nodig. Die kwam in de eerste plaats van de (vroegere) powergroupleden van Silicon Graphics / SGI (Ronald, Peter, Luc, Ruud en Bart), van wie ik veel leerde over supercomputing en parallellisatie. Daarnaast was ook de ondersteuning vanuit SARA (Henk en Mark) van grote klasse!

Hoewel het het laaste half jaar soms anders leek, is er meer in het leven dan wetenschap alleen. Voor mij vormt de muziek een belangrijke uitlaatklep. Daarbij heeft mijn begeleider en muzikale broer Onno Coster een grote rol gespeeld. Onno, ik hoop dat we de Leopatraspirit nog jaren kunnen volhouden, ook als daar straks een grote oceaan tussen zit. 'Leo bedankt!'

Een andere muzikale uitlaatklep werd gevormd door de 'dames uit Eibergen'; met name als de weekendberekeningen weer eens op niets waren uitgelopen en ik 's maandags nauwelijks was opgeschoten, zorgde hun grote inzet en motivatie er altijd voor dat ik weer vrolijk naar huis reed. Hun bijdrage aan dit proefschrift is dan ook groter dan ze zelf kunnen ver-

moeden.

Op deze plaats wil ik ook mijn ouders bedanken, die me tot op de dag van vandaag onvoorwaardelijk gesteund hebben en op wie ik altijd heb kunnen terugvallen. Daarin wil ik ook graag mijn zus Marion betrekken die, iets meer vanaf de zijlijn, ook altijd haar belangstelling heeft getoond.

En ten slotte, Irene. Bedankt voor alle steun de afgelopen jaren en voor je bijdrage aan dit proefschrift tussen de regels door. Het einde van de promotieperiode vormt voor ons in vele opzichten het begin van een nieuw groot avontuur. Ik hoop dat we daar nog lang samen van kunnen genieten.

Harald Tepper Enschede, september 2001

Bibliography

[1] D.J. Adams, *Grand canonical ensemble Monte Carlo for a Lennard-Jones fluid*, Mol. Phys. **29**, 307 (1975).

[2] B.J. Alder and T.E. Wainwright, *Phase transition for a hard sphere system*, J. Chem. Phys. **27**, 1208 (1957).

[3] B.J. Alder and T.E. Wainwright, *Studies in molecular dynamics. I. General method*, J. Chem. Phys. **31**, 459 (1959).

[4] M.P. Allen, *Back to basics*, in *Computer Simulation in Chemical Physics*, ed. by M.P. Allen and D.J. Tildesley (Kluwer Academic Publishers, the Netherlands, 1993). [pp. 49-92]

[5] M.P. Allen and D.J. Tildesley, *Computer simulation of liquids* (Oxford University Press, Oxford, 1987).

[6] R.J. Argauer and G.R. Landolt, U.S. Patent 3,702,886 (1972).

[7] L.A. Báez and P. Clancy, *The kinetics of crystal growth and dissolution from the melt in Lennard-Jones solutions*, J. Chem. Phys. **102**, 8138 (1995).

[8] V.G. Baidakov, G.G. Chernykh, and S.P. Protsenko, *Effect of the cut-off radius of the intermolecular potential on phase equilibrium and surface tension in Lennard-Jones systems*, Chem. Phys. Lett. **321**, 315 (2000).

[9] R.M. Barrer, *The sorption of polar and non-polar gases by zeolites*, Proc. Roy. Soc. London A **167**, 392 (1938).

[10] R.M. Barrer, Trans. Faraday Soc. **37**, 590 (1941).

[11] R.M. Barrer and W. Jost, *A note on interstitial diffusion*, Trans. Faraday Soc. **45**, 928 (1949).

[12] R.M. Barrer and P.J. Denny, *Hydrothermal chemistry of the silicates. Part IX. Nitrogenous aluminosilicates*, J. Chem. Soc. **99** 971 (1961).

[13] R.M. Barrer, *Chemical nomenclature and formulation of compositions of synthetic and natural zeolites*, Pure Appl. Chem. **51**, 1091 (1979).

[14] H. van Beijeren, K.W. Kehr, and R. Kutner, *Diffusion in concentrated lattice gases. III. Tracer diffusion on a one-dimensional lattice*, Phys. Rev. B **28**, 5711 (1983).

[15] H. van Bekkum, E.M. Flanigan, and J.C. Jansen, *Introduction to zeolite science and practice* (Elsevier, Amsterdam, 1991).

[16] P. Bennema and J.P. van der Eerden, *Crystal graphs, connected nets, roughening transition and the morphology of crystals*, in *Morphology of Crystals. Part A*, ed. by I. Sunagawa (Terrapub, Tokyo, 1987). [Chapter 1]

[17] J.M. Bennett, J.P. Cohen, E.M. Flanigan, J.J. Pluth, and J.V. Smith, *Crystal structure of tetrapropylammonium hydroxide — Aluminium Phosphate Number 5*, in *Intrazeolite chemistry*, ed. by G.D. Stucky and F.G. Dwyer, Am. Chem. Soc. Symp. Ser. **218**, 109 (1983).

[18] H.J.C. Berendsen, J.P.M. Postma, W.F. van Gunsteren, A. DiNola, and R.J. Haak, *Molecular dynamics with coupling to an external bath*, J. Chem. Phys. **81**, 3684 (1984).

[19] H.J.C. Berendsen and W.F. van Gunsteren, GROMOS *Reference Manual* (University of Groningen, Groningen, 1987).

[20] B.J. Berne and R. Pecora, *Dynamic light scattering* (Wiley, New York, 1976). [p. 86]

[21] A. Boutin, R.J.-M. Pellenq, D. Nicholson, *Molecular simulation of the stepped adsorption isotherm of methane in $AlPO_4$-5*, Chem. Phys. Lett. **219**, 484 (1994).

[22] D.W. Breck, U.S. Patent 3,130,007 (1964).

[23] W.J. Briels, *An expansion of the intermolecular energy in a complete set of symmetry-adapted functions; convergence of the series for methane-methane and adamantane-adamantane interactions*, J. Chem. Phys. **73**, 1850 (1980).

[24] W.J. Briels, *Theory of simple liquids* (Uppsala University, Uppsala, 1993) (lecture notes).

[25] W.J. Briels and H.L. Tepper, *Crystal growth of the Lennard-Jones (100) surface by means of equilibrium and nonequilibrium molecular dynamics*, Phys. Rev. Lett. **79**, 5074 (1997).
[*Chapter 2* of this thesis]

[26] J.Q. Broughton and L.V. Woodcock, *A molecular dynamics study of surface melting*, J. Phys. C: Solid State Phys. **11**, 2743 (1978).

[27] J.Q. Broughton, A. Bonissent, and F.F. Abraham, *The fcc (111) and (100) crystal-melt interfaces: A comparison by molecular dynamics simulation*, J. Chem. Phys. **74**, 4029 (1981).

[28] J.Q. Broughton, G.H. Gilmer, and K.A. Jackson, *Crystallization rates of a Lennard-Jones liquid*, Phys. Rev. Lett. **49**, 1496 (1982).

[29] J.Q. Broughton and G.H. Gilmer, *Molecular dynamics investigation of the crystal-fluid interface. I. Bulk properties*, J. Chem. Phys. **79**, 5095 (1983).

[30] J.Q. Broughton and G.H. Gilmer, *Molecular dynamics of the crystal-fluid interface. V. Structure and dynamics of crystal-melt systems*, J. Chem. Phys. **84**, 5749 (1986).

[31] J.Q. Broughton and G.H. Gilmer, *Molecular dynamics of the crystal-fluid interface. VI. Excess surface free energies of crystal-liquid systems*, J. Chem. Phys. **84**, 5759 (1986).

[32] E. Burke, J.Q. Broughton, and G.H. Gilmer, *Crystallization of fcc (111) and (100) crystal-melt interfaces: A comparison by molecular dynamics for the Lennard-Jones system*, J. Chem. Phys. **89**, 1030 (1988).

[33] W.K. Burton, N. Cabrera, and F.C. Frank, *The growth of crystals and the equilibrium structure of their surfaces*, Phil. Trans. R. Soc. **243**, 299 (1951).

[34] J. Caro, H. Jobic, M. Bülow, J. Kärger, and B. Zibrowius, *Molecular mobility measurement of hydrocarbons in zeolites by NMR techniques*, Adv. Catal. **39**, 351 (1993).

[35] B. Chalmers, *Principles of solidification* (John Wiley & Sons, New York, 1964). [p. 44]

[36] D. Chandler, *Introduction to modern statistical mechanics* (Oxford University Press, Oxford, 1987). [Chapter 8. *Statistical mechanics of non-equilibrium systems*]

[37] N.Y. Chen, T.F. Degnan Jr., and C. Morris Smith, *Molecular transport and reaction in zeolites* (VCH Publishers, New York, 1994).

[38] H. de St. Claire-Deville, Compt. Rend. **54**, 324 (1862).

[39] J.H.R. Clarke, W. Smith, and L.V. Woodcock, *Short range effective potentials for ionic fluids*, J. Chem. Phys. **84**, 2290 (1986).

[40] M.-O. Coppens, A.T. Bell, and A.K. Chakraborty, *Influence of occupancy and pore network topology on tracer and transport diffusion in zeolites*, in *Scientific computing in chemical engineering II*, ed. by F. Keil, W. Mackens, H. Voss, and J. Werther (Springer-Verlag, Berlin, 2000). [pp. 200-207]

[41] A.F. Cronstedt, *Rön och beskrivning om en obekant bärg art, som kallas zeolites*, Kungl. Vetenskaps Akad. Handl. Stockholm **18**, 120 (1756). [Translated by G. Sumelius in *Molecular sieves*, ed. by M.L. Occelli and H. Robson (Van Nostrand Reinhold, New York, 1992).]

[42] A.F. Cronstedt [originally anonymous], *Försök till Mineralogie eller Mineralrikets uppställning* (1758). [Translated as *An essay towards a system of mineralogy* (Charles Dilly, London, 2nd ed. 1788).]

[43] A. Damour, Ann. Mines **17**, 191 (1840).

[44] L.S. Darken, Trans. AIME. **175**, 184 (1948).

[45] R.L. Davidchack and B.B. Laird, *Simulation of the binary hard-sphere crystal/melt interface*, Phys. Rev. E **54**, R5905 (1996).

[46] R.L. Davidchack and B.B. Laird, *Simulation of the hard-sphere crystal-melt interface*, J. Chem. Phys. **108**, 9452 (1998).

[47] S.D. Druger, A. Nitzan, and M.A. Ratner, *Dynamic bond percolation theory: A microscopic model for diffusion in dynamically disordered systems. I. Definition and one-dimensional case*, J. Chem. Phys. **79**, 3133 (1983).

[48] A. Dyer, *Zeolite molecular sieves* (John Wiley, Chichester, 1988).

[49] H. Eichhorn, Poggendorf Ann. Phys. Chem. **105**, 126 (1858).

[50] A. Einstein, *On the movement of small particles suspended in stationary liquids demanded by the molecular kinetics theory of heat*, Ann. Phys. (Leipzig) **17**, 549 (1905). [Reproduced in *Investigations on the theory of the Brownian movement* (Dover Publications, New York, 1956).]

[51] A. Einstein, *On the theory of Brownian movement*, Ann. Phys. **19**, 371 (1906). [Reproduced in *Investigations on the theory of the Brownian movement* (Dover Publications, New York, 1956).]

[52] A. Einstein, quoted in M.J. Klein, *Thermodynamics in Einstein's Universe*, Science **157**, 509 (1967).

[53] D.J. Evans and G.P. Morriss, *Statistical mechanics of nonequilibrium liquids* (Academic Press, London, 1990). [p. 124]

[54] P.A. Fedders, and O.F. Sankey, *The generalized atomic hopping problem — occupancy correlation functions*, Phys. Rev. B **15**, 3580 (1977).

[55] P.A. Fedders, *Two-point correlation functions for a distinguishable particle hopping on a uniform one-dimensional chain*, Phys. Rev. B **17**, 40 (1978).

[56] A. Fick, Ann. Phys. (Leipzig) **94**, 59 (1855).

[57] A. Finkelstein and O.S. Andersen, *The gramicidin A channel: a review of its permeability characteristics with special reference to the single-file aspect of transport.*, J. Membr. Biol. **59**, 155 (1981).

[58] F.C. Frank, *The influence of dislocation on crystal growth*, Disc. Faraday Soc. **5**, 48 (1949).

[59] F.C. Frank, in *Morphology of crystals. Part A*, ed. by I. Sunagawa (Terrapub, Tokyo, 1987). [Foreword]

[60] D. Frenkel and B. Smit, *Understanding molecular simulation. From algorithms to applications* (Academic Press, San Diego, 1996).

[61] J. Frenkel, Phys. Z. Sowjetunion. **1**, 498 (1932).

[62] G. Friedel, Bull. Soc. Franc. Mineral. Cristallogr. **19**, 94 (1896).

[63] S. Fritzsche, R. Haberlandt, and J. Kärger, *An MD study on the correlation between trasport diffusion and self-diffusion in zeolites*, Z. Phys. Chem. **189** 211 (1995).

[64] S. Fritzsche, M. Wolfsberg, R. Haberlandt, P. Demontis, G.B. Suffritti, and A. Tilocca, *About the influence of lattice vibrations on the diffusion of methane in a cation-free LTA zeolite*, Chem. Phys. Lett. **296** 253 (1998).

[65] D. Gernez, Compt. rend. **95**, 1278 (1882).

[66] J.W. Gibbs (1877-1878). [Reprinted in J.W. Gibbs, *The scientific papers*, Vol. 1, p. 325 (Dover Publications, New York, 1961).]

[67] R. Gomer, *Diffusion of adsorbates on metal-surfaces*, Rep. Progr. Phys. **53**, 917 (1990).

[68] M.H. Grabow, G.H. Gilmer, and A.F. Bakker, *Molecular dynamics studies of silicon solidification and melting*, Mat. Res. Soc. Symp. Proc. **141**, 349 (1989).

[69] F. Grandjean, Compt. Rend. **149**, 866 (1909).

[70] W.F. van Gunsteren and H.J.C. Berendsen, *Algorithms for macromolecular dynamics and constraint dynamics*, Mol. Phys. **34**, 1311 (1977).

[71] V. Gupta, S.S. Nivarthi, A.V. McCormick, and H.T. Davis, *Evidence for single-file diffusion of ethane in the molecular sieve $AlPO_4$-5*, Chem. Phys. Lett. **247**, 596 (1995).

[72] A.A. Gusev, M.M. Zehnder, and U.W. Suter, *Fluctuation formula for elastic constants*, Phys. Rev. B **54**, 1 (1996).

[73] K. Hahn, and J. Kärger, *Propagator and mean-square displacement in single-file systems*, J. Phys. A: Math. Gen. **28**, 3061 (1995).

[74] K. Hahn, J. Kärger, and V. Kukla, *Single-file diffusion observation*, Phys. Rev. Lett. **76**, 2762 (1996).

[75] K. Hahn, and J. Kärger, *Molecular dynamics simulation of single-file systems*, J. Phys. Chem. **100**, 316 (1996).

[76] H.J.M. Hanley, *Transport phenomena in fluids* (Marcel Dekker, New York, 1969). [p. 248]

[77] J.-P. Hansen and L. Verlet, *Phase transitions of the Lennard-Jones system*, Phys. Rev. **184**, 151 (1969).

[78] J.-P. Hansen and I.R. McDonald, *Theory of simple liquids* (Academic Press, London, 1986).

[79] P.E. Hathaway and M.E. Davis, *High resolution, quasi-equilibrium sorption studies of molecular sieves*, Cat. Lett. **5**, 333 (1990).

[80] D.T. Hayhurst and A.R. Paravar, *Diffusion of C-1 to C-5 normal paraffins in silicalite*, Zeolites **8**, 27 (1988).

[81] A.D.J. Haymet, *Theory of the equilibrium liquid-solid transition*, Ann. Rev. Phys. Chem. **38**, 89 (1987).

[82] J.A. Hayward and A.D.J. Haymet, *The ice/water interface: Molecular dynamics simulations of the basal, prism,* $\{2021\}$*, and* $\{2110\}$ *interfaces of ice Ih*, J. Chem. Phys. **114**, 3713 (2001).

[83] H. Hertz, Ann. Phys. (Leipzig) **17**, 177 (1882).

[84] A.L. Hodgkin and R.D. Kenes, J. Physiol. (London) **128**, 61 (1955).

[85] M.A. van der Hoef, *Free energy of the Lennard-Jones solid*, J. Chem. Phys. **113**, 8142 (2000).

[86] J.P. Hoogenboom, H.L. Tepper, N.F.A. van der Vegt, and W.J. Briels, *Transport diffusion of argon in AlPO*$_4$*-5 from equilibrium molecular dynamics simulations*, J. Chem. Phys. **113**, 6875 (2000).
[*Chapter 8* of this thesis]

[87] W.G. Hoover, *Canonical dynamics: Equilibrium phase-space distributions*, Phys. Rev. A **31**, 1695 (1985).

[88] H.E.A. Huitema and J.P. van der Eerden, *Can Monte Carlo simulation describe dynamics? A test on Lennard-Jones systems*, J. Chem. Phys. **110**, 3267 (1999).

[89] H.E.A. Huitema, M.J. Vlot, and J.P. van der Eerden, *Simulations of crystal growth from Lennard-Jones melt: Detailed measurements of the interface structure*, J. Chem. Phys. **111**, 4714 (1999).

[90] H.E.A. Huitema, B. van Hengstum, and J.P. van der Eerden, *Simulation of crystal growth from Lennard-Jones solutions*, J. Chem. Phys. **111**, 10248 (1999).

[91] M. Iwamatsu and K. Horii, *Interface kinetics of freezing and melting of Si and Na*, Phys. Lett. A **214**, 71 (1996).

[92] K.A. Jackson and B. Chalmers, *Kinetics of solidification*, Can. J. Phys. **34**, 473 (1956).

[93] K.A. Jackson, *Mechanism of growth*, in *Liquid metals and solidification* (Am. Soc. Metals, Cleveland, Ohio, 1958). [pp. 174-186]

[94] K.A. Jackson, *Theory of melt growth*, in *Crystal growth and characterization*, ed. by R. Ueda and J.B. Mullin (North-Holland, Amsterdam, 1975).

[95] K.A. Jackson, *Computer modeling of atomic scale crystal growth processes*, J. Cryst. Growth **198/199**, 1 (1999).

[96] B.J. Jesson and P.A. Madden, *Ab initio determination of the melting point of aluminium by thermodynamic integration*, J. Chem. Phys. **113**, 5924 (2000).

[97] B.J. Jesson and P.A. Madden, *Structure and dynamics of the aluminium solid-liquid interface: An ab initio simulation*, J. Chem. Phys. **113**, 5935 (2000).

[98] H. Jobic, K. Hahn, J.Kärger, M.Bée, A. Tuel, M. Noack, I. Girnus, and G. Kearley, *Unidirectional and Single-File Diffusion of Molecules in One-Dimensional Channel Systems. A Quasi-Elastic Neutron Scattering Study*, J. Phys. Chem. B **101**, 5834 (1997).

[99] H. Jobic, J. Kärger, and M. Bée, *Simultaneous measurement of self- and transport diffusivities in zeolites*, Phys. Rev. Lett. **82**, 4260 (1999).

[100] J.K. Johnson, J.A. Zollweg, and K.E. Gubbins, *The Lennard-Jones equation of state revisited*, Mol. Phys. **78**, 591 (1993).

[101] R.L. June, A.T. Bell, and D.N. Theodorou, *Prediction of low occupancy sorption of alkanes in silicalite*, J. Phys. Chem. **94**, 1508 (1990).

[102] R.L. June, A.T. Bell, and D.N. Theodorou, *Molecular dynamics study of methane and xenon in silicalite*, J. Phys. Chem. **94**, 8232 (1990).

[103] J. Kärger and D.M. Ruthven, *On the comparison between macroscopic and NMR measurements of intracrystalline diffusion in zeolites*, Zeolites **9**, 267 (1989).

[104] J. Kärger, *Straightforward derivation of the long-time limit of the mean-square displacement in one-dimensional diffusion*, Phys. Rev. A **45**, 4173 (1992).

[105] J. Kärger, M. Petzold, H. Pfeiffer, S. Ernst, and J. Weitkamp, *Single-file diffusion and reaction in zeolites*, J. Cat. **136**, 283 (1992).

[106] J. Kärger and D. Ruthven, *Diffusion in Zeolites and Other Microporous Solids* (Wiley-Interscience, New York, 1992).

[107] D. Keffer, A.V. McCormick, and H.T. Davis, *Unidirectional and single-file diffusion in AlPQ-5: molecular dynamics simulations*, Mol. Phys. **87**, 367 (1996).

[108] F.J. Keil, R. Krishna, and M.-O. Coppens, *Modeling of diffusion in zeolites*, Rev. Chem. Eng. **16**, 71 (2000).

[109] G.T. Kerr, U.S. Patent 3,247,195 (1966).

[110] A.V. Kiselev, A.A. Lopatkin, and A.A. Shulga, *Molecular statistical calculation of gas-adsorption by silicalite*, Zeolites **5**, 216 (1985).

[111] M.D. Kluge and J.R. Ray, *Velocity versus temperature relation for solidification and melting of silicon: A molecular-dynamics study*, Phys. Rev. B **39**, 1738 (1989).

[112] M. Knudsen, Ann. Phys. (Leipzig) **29**, 179 (1909).

[113] G.T. Kokotailo, S.L. Lawton, D.H. Olson, and W.M. Meier, *Structure of synthetic zeolite ZSM-5*, Nature **272**, 437 (1978).

[114] D.I. Kopelevich and H.-C. Chang, *Does lattice vibration drive diffusion in zeolites?*, J. Chem. Phys. **114**, 3776 (2001).

[115] V. Kukla, J. Kornatowski, D. Demuth, I. Girnus, H. Pfeiffer, L.V.C. Rees, S. Schunk, K.K. Unger, and J. Kärger, *NMR studies of single-file diffusion in unidimensional channel zeolites*, Science **272**, 702 (1996).

[116] A.J.C. Ladd and L.V. Woodcock, *Triple-point coexistence properties of the Lennard-Jones system*, Chem. Phys. Lett. **51**, 155 (1977).

[117] A.J.C. Ladd and L.V. Woodcock, *Interfacial and coexistence properties of the Lennard-Jones system at triple point*, Mol. Phys. **36**, 611 (1978).

[118] B.B. Laird and A.D.J. Haymet, *The crystal/liquid interface: Structure and properties from computer simulation*, Chem. Rev. **92**, 1819 (1992).

[119] P. Lancaster and Kęstutis Šalkauskas, *Curve and surface fitting. An introduction* (Academic Press, London, 1986).

[120] A.S. Lemak and N.K. Balabaev, *On the Berendsen thermostat*, Mol. Sim. **13**, 177 (1994).

[121] A.C. Levi and M. Kotrla, *Theory and simulation of crystal growth*, J. Phys.: Cond. Mat. **9**, 299 (1997).

[122] C.S. Liu, J. Xia, Z.G. Zhu, and D.Y. Sun, *The cooling rate dependence of crystallization for liquid copper: A molecular dynamics study*, J. Chem. Phys. **114**, 7506 (2001).

[123] E.J. Maginn, A.T. Bell, and D.N. Theodorou, *Transport diffusivity of methane in silicalite from equilibrium and nonequilibrium simulations*, J. Phys. Chem. **97**, 4173 (1993).

[124] I.V. Markov, *Crystal growth for beginners* (World Scientific, New York, 1995).

[125] J.C. Maxwell, Phil. Mag. **19**, 19 (1860), and Phil. Mag. **20**, 21 (1860). [Reproduced in *Scientific papers of J.C. Maxwell*, ed. by W.D. Niven, p. 629 (Dover, New York, 1952).]

[126] J.W. McBain, *The sorption of gases and vapors by solids* (Rutledge and Sons, London, 1932). [Chapter 5]

[127] W.M. Meier and D.H. Olson, *Atlas of Zeolite Structure Types* (Butterworth-Heinemann, London, 1992).

[128] S.L. Meisel, J.P. McCullough, C.H. Lechthaler, and P.B. Weisz, *Gasoline from methanol in one step*, Chem. Tech. **6**, 86 (1976).

[129] R.M. Milton, U.S. Patent 2,882,243 (1959).

[130] R.M. Milton, U.S. Patent 2,882,244 (1959).

[131] B. Moore, Zeitschr. f. Phys. Chem. **12**, 545 (1893).

[132] A. Mori, *Effect of mass flow in melt on the motion of the crystal-melt interface of hard spheres: A molecular dynamics study*, J. Phys. Soc. Jap. **66**, 1579 (1997).

[133] R. Moss and P. Harrowell, *Dynamic Monte Carlo simulations of freezing and melting at the 100 and 111 surfaces of the simple cubic phase in the face-centered-cubic lattice gas*, J. Chem. Phys. **100**, 7630 (1994).

[134] T. Motooka, K. Nisihira, S. Munetoh, K. Moriguchi, and A. Shintani, *Molecular dynamics simulations of solid-phase epitaxy of Si: Growth mechanisms*, Phys. Rev. B **61**, 8537 (2000).

[135] F.Müller-Plathe, S.C. Rogers, and W.F. van Gunsteren, *Gas sorption and transport in polyisobutylene: Equilibrium and nonequilibrium molecular dynamics simulations*, J. Chem. Phys. **98**, 9895 (1993).

[136] J.J. Nicolas, K.E. Gubbins, W.B. Streett, and D.J. Tildesley, *Equation of state for the Lennard-Jones fluid*, Mol. Phys. **37**, 1429 (1979).

[137] W. Niessen and H.G. Karge, Stud. Surf. Sci. Catal. **60**, 213 (1991).

[138] S.S. Nivarthi, A.V. McCormick, and H.T. Davis, *Diffusion anisotropy in molecular sieves. A Fourier transform PFG NMR study of methane in $AlPO_4$-5*, Chem. Phys. Lett. **229**, 298 (1994).

[139] S. Nosé, *A unified formulation of the constant temperature molecular dynamics methods*, J. Chem. Phys. **81**, 511 (1984).

[140] D.W. Oxtoby and P.R. Harrowell, *The effect of density change on crystal growth rates from the melt*, J. Chem. Phys. **96**, 3834 (1992).

[141] D.W. Oxtoby and Y.C. Shen, *Density functional approaches to the dynamics of phase transitions*, J. Phys.: Cond. Matt. **8**, 9657 (1996).

[142] E. Passaglia and D. Pongiluppi, Mineral. Mag. **40**, 298 (1975).

[143] L. Pauling, Proc. Nat. Acad. Sci. **16**, 453 (1930).

[144] L. Pauling, Z. Kristallogr. **74**, 213 (1930).

[145] P.M. Richards, *Interface kinetics of freezing and melting with a density change*, Phys. Rev. B **38**, 2727 (1988).

[146] J.W. Richardson Jr., J.J. Pluth, and J.V. Smith, *Aluminophosphate number 5: time-of-flight neutron powder diffraction study of calcined powder at 295 K*, Acta Cryst. C**43**, 1469 (1987).

[147] L. Riekert, *Rates of sorption and diffusion of hydrocarbons in zeolites*, AIChE J. **17** 446 (1971).

[148] B. Roux and M. Karplus, *Ion-transport in a Gramicidin-like channel: Dynamics and mobility*, J. Phys. Chem., **95**, 4856 (1991).

[149] W.S. Russell, *Polynomial interpolation schemes for internal derivative distributions on structured grids*, Appl. Num. Math. **17**, 129 (1995).

[150] D.M. Ruthven, R.I. Derrah, and K.F. Loughlin, *Diffusion of light hydrocarbons in 5A zeolite*, Can. J. Chem. **51**, 3514 (1973).

[151] D.M. Ruthven, *Principles of adsorption and adsorption processes* (John Wiley, New York, 1984).

[152] Y. Saito, *Statistical physics of crystal growth* (World scientific, Singapore, 1996).

[153] M.J. Sanborn and R.Q. Snurr, *Diffusion of binary mixtures of CF_4 and n-alkanes in faujasite*, Sep. Purif. Techn. **20**, 1 (2000).

[154] M.J. Sanborn and R.Q. Snurr, *Predicting membrane fluc of CH_4 and CF_4 mixtures in faujasite from molecular simulations*, Submitted to AIChE J.

[155] O.F. Sankey and P.A. Fedders, *The generalized atomic hopping problem — particle correlation functions*, Phys. Rev. B **15**, 3586 (1977).

[156] U. Schemmert, J. Kärger, and J. Weitkamp, *Interference microscopy as a technique for directly measuring intracrystalline transport diffusion in zeolites*, Microp. Mesop. Mat. **32**, 101 (1999).

[157] Y.C. Shen and D.W. Oxtoby, *Density functional theory of crystal growth: Lennard-Jones fluids*, J. Chem. Phys. **104**, 4233 (1995).

[158] Y.C. Shen and D.W. Oxtoby, *Nucleation of Lennard-Jones fluids: A density functional approach*, J. Chem. Phys. **105**, 6517 (1996).

[159] Y.C. Shen and D.W. Oxtoby, *bcc Symmetry in the crystal-melt interface of Lennard-Jones fluids examined through density functional theory*, Phys. Rev. Lett. **77**, 3585 (1996).

[160] D.S. Sholl, *Predicting single-component permeance through macroscopic zeolite membranes from atomistic simulations*, Ind. Eng. Chem. Res. **39**, 3737 (2000).

[161] A.I. Skoulidas and D.S. Sholl, *Direct tests of the Darken approximation for molecular diffusion in zeolites using equilibrium molecular dynamics*, Phys. Chem. B **105**, 3151 (2001).

[162] W. Smith and T.R. Forester, *DL_POLY_2.0: A general-purpose parallel molecular dynamics simulation package*, J. Molec. Graphics **14**, 136 (1996).

[163] J. Stefan, Wien. Ber. **65**, 323 (1872).

[164] G. Tammann, *Kristallisieren und schmelzen. Ein Beitrag zur Lehre derÄnderungen des Aggregatzustandes* (Verlag J.A. Barth, Leipzig, 1903).

[165] G. Tammann, *Aggregatzustände. Die Zustandsänderungen der Materie in Abhängigkeit von Druck und Temperatur* (Leopold Voss, Leipzig, 1923). [Chapter 9. *Der Übergang eines instabileren in einen stabileren Aggregatszustand.*]

[166] W.H. Taylor, Z. Kristallogr. **74**, 1 (1930).

[167] D.E. Temkin, *Crystallization process* (Consultant Bureau, New York, 1966).

[168] H.L. Tepper, J.P. Hoogenboom, N.F.A. van der Vegt, and W.J. Briels, *Unidirectional diffusion of methane in $AlPO_4$-5*, J. Chem. Phys. **110**, 11511 (1999).
[*Chapter 7* of this thesis]

[169] H.L. Tepper and W.J. Briels, *Simulations of crystallization and melting of the FCC (100) interface: the crucial role of lattice imperfections*, J. Cryst. Growth **230**, 270 (2001).
[*Chapter 3* of this thesis]

[170] H.L. Tepper and W.J. Briels, *Crystallization and melting in the Lennard-Jones system. Equilibration, relaxation, and long-time dynamics of the moving interface*, Accepted for publication in J. Chem. Phys. (scheduled issue: November 22, 2001).
[*Chapter 4* of this thesis]

[171] H.L. Tepper and W.J. Briels, *Crystal growth and interface relaxation rates from fluctuations in an equilibrium simulation of the Lennard-Jones (100) crystal-melt system*, Submitted to J. Chem. Phys.
[*Chapter 5* of this thesis]

[172] H.L. Tepper and W.J. Briels, *Comments on the use of the Einstein equation for transport diffusion. Application to argon in $AlPO_4$-5*, Submitted to J. Chem. Phys.
[*Chapter 9* of this thesis]

[173] D.N. Theodorou, R.Q. Snurr, and A.T. Bell, *Molecular dynamics and diffusion in microporous materials*, in *Comprehensive supramolecular chemistry*, Vol. 7, ed. by G. Alberti and T. Bein (Pergamon, Oxford, 1996). [Chapter 18, pp. 507-548]

[174] S. Toxværd, *Algorithms for canonical molecular dynamics simulations*, Mol. Phys. **72**, 159 (1991).

[175] S. Toxværd, *Molecular dynamics at constant temperature and pressure*, Phys. Rev. E **47**, 343 (1993).

[176] J.Y. Tsao, M.J. Aziz, M.O. Thompson, and P.S. Peercy, *Asymmetric melting and freezing kinetics in silicon*, Phys. Rev. Lett. **56**, 2712 (1986).

[177] C.J. Tymczak and J.R. Ray, *Asymmetric crystallization and melting kinetics in sodium: A molecular-dynamics study*, Phys. Rev. Lett. **64**, 1278 (1990).

[178] C.J. Tymczak and J.R. Ray, *Interface response function for a model of sodium: A molecular dynamics study*, J. Chem. Phys. **92**, 7520 (1990).

[179] C. Uebing, V. Pereyra, and G. Zgrablich, *Diffusion of interacting lattice gases on heterogeneous surfaces with simple topographies*, Surf. Sci. **366**, 185 (1996).

[180] D.R. Uhlmann, J.F. Hays, and D. Turnbull, *The effect of high pressure on B_2O_3: crystallisation, densification, and the crystallization anomaly*, Phys. Chem. Glasses **8**, 1 (1967).

[181] N. Van-Den-Begin, L.V.C. Rees, J. Caro, and M. Bülow, *Fast adsorption-desorption kinetics of hydrocarbons in Silicalite-1 by the single-step frequency-response method*, Zeolites **9**, 287 (1989).

[182] T.J.H. Vlugt, W. Zhu, F. Kapteijn, J.A. Moulijn, B. Smit, and R. Krishna, *Adsorption of linear and branched alkanes in the zeolite silicalite-1*, J. Am. Chem. Soc. **120**, 5599 (1998).

[183] R.L. Wadlinger, G.T. Kerr, and E.J. Rosinski, U.S. Patent 3,308,069 (1967).

[184] Q.-H. Wei, C. Bechinger, and P. Leiderer, *Single-file diffusion of colloids in one-dimensional channels*, Science **287**, 625 (2000).

[185] O. Weigel and E. Steinhoff, Z. Kristallogr. **61**, 125 (1925).

[186] P.B. Weisz and H. Zollinger, *Sorption-diffusion in heterogeneous systems*, Trans. Faraday Soc. **63**, 1815 (1967).

[187] P.B. Weisz, *Zeolites — New horizons in catalysis*, Chem. Tech. **3**, 498 (1973).

[188] B. Widom, *Some topics in the theory of fluids*, J. Chem. Phys. **39**, 2808 (1963).

[189] A. Williams, R. Moss, and P. Harrowell, *Orientation dependent interface mobilities in a kinetic mean field theory of freezing and melting*, J. Chem. Phys. **99**, 3998 (1993).

[190] H.A. Wilson, *On the velocity of solidification and viscosity of supercooled liquids*, Philos. Mag. **50**, 238 (1900).

[191] S.T. Wilson, B.M. Lok, C.A. Messina, T.R. Cannan, and E.M. Flanigan, *Aluminophosphate molecular sieves: A new class of microporous crystalline inorganic solids*, J. Am. Chem. Soc. **104**, 1146 (1982).

[192] Y. Yasuda, *Frequency response method for study of the kinetic behavior of a gas-surface system. 1. Theoretical treatment*, J. Phys. Chem. **80**, 1867 (1976).

[193] Y. Yasuda, *Frequency response method for study of the kinetic behavior of a gas-surface system. 2. An ethylene-on-zinc oxide system*, J. Phys. Chem. **80**, 1870 (1976).

[194] Y. Yasuda, *Determination of vapor diffusion coefficients in zeolite by the frequency response method*, J. Phys. Chem. **86**, 1913 (1982).